Self-Reacting Point Absorber Wave Energy Converters

by

Scott James Beatty
B.A.Sc., University of British Columbia, 2003
M.A.Sc., University of Victoria, 2009

A Dissertation Submitted in Partial Fulfillment of the
Requirements for the Degree of

DOCTOR OF PHILOSOPHY

in the Department of Mechanical Engineering

Self-Reacting Point Absorber Wave Energy Converters

by

Scott James Beatty
B.A.Sc., University of British Columbia, 2003
M.A.Sc., University of Victoria, 2009

Supervisory Committee

Dr. B. Buckham, Supervisor
(Department of Mechanical Engineering)

Dr. P. Wild, Supervisor
(Department of Mechanical Engineering)

Dr. J. Klymak, Outside Member
(School of Earth and Ocean Sciences)

Supervisory Committee

Dr. B. Buckham, Supervisor
(Department of Mechanical Engineering)

Dr. P. Wild, Supervisor
(Department of Mechanical Engineering)

Dr. J. Klymak, Outside Member
(School of Earth and Ocean Sciences)

ABSTRACT

A comprehensive set of experimental and numerical comparisons of the performance of two self-reacting point absorber wave energy converter (WEC) designs is undertaken in typical operating conditions. The designs are either currently, or have recently been, under development for commercialization. The experiments consist of a series of 1:25 scale model tests to quantify hydrodynamic parameters, motion dynamics, and power conversion. Each WEC is given a uniquely optimized power take off damping level. For hydrodynamic parameter identification, an optimization based method to simultaneously extract Morison drag and Coulomb friction coefficients from decay tests of under-damped, floating bodies is developed. The physical model features a re-configurable reacting body shape, a feedback controlled power take-off, a heave motion constraint system, and a mooring apparatus. A theoretical upper bound on power conversion for single body WECs, called Budal's upper bound, is extended to two body WECs.

The numerical analyses are done in three phases. In the first phase, the WECs are constrained to heave motion and subjected to monochromatic waves. Quantitative comparisons are made of the WEC designs in terms of heave motion dynamics and power conversion with reference to theoretical upper bounds. Design implications of a reactive power take-off control scheme and relative motion constraints on the wave energy converters are investigated using an experimentally validated, frequency domain, numerical dynamics model. In the second phase, the WECs are constrained to heave motion and subjected to panchromatic waves. A time domain numerical model, validated by the experimental results, is used to compare the WECs in terms of power matrices, capture width matrices, and mean annual energy production. Results indicate that the second WEC design can convert 30% more energy, on average, than the first design given the conditions at a representative location near the West coast of Vancouver Island, British Columbia, Canada. In the last phase, the WECs are held with three legged, horizontal, moorings and subjected to monochromatic waves. Numerical simulations using panelized body geometries for calculations of Froude-Krylov, Morison drag, and hydrostatic loads are developed in ProteusDS. The simulation results—mechanical power, mooring forces, and dynamic motions—are compared to model test results. The moored WEC designs exhibit power conversion consistent with heave motion constrained results in some wave conditions. However, large pitch and roll motions severely degrade the power conversion of each WEC at wave frequencies equal to twice the pitch natural frequency. Using simulations, vertical stabilizing strakes, attached to the reacting bodies of the WECs are shown to increase the average power conversion up to 190% compared to the average power conversion of the WECs without strakes.

Contents

Supervisory Committee ii

Abstract iii

Table of Contents v

List of Tables viii

List of Figures ix

Acknowledgements xi

Dedication xii

1 Introduction 1

- 1.1 Background 1
  - 1.1.1 The significance of this research 3
- 1.2 Key Contributions 3
- 1.3 Outline 4

2 Experimental and numerical comparisons of self-reacting point absorber wave energy converters in regular waves 5

- 2.1 Introduction 6
- 2.2 Literature Review 7
- 2.3 Methods 9
  - 2.3.1 Numerical Methods 9
  - 2.3.2 Experimental Methods 14
- 2.4 Results 20
  - 2.4.1 Experimental Results 20
  - 2.4.2 Validation of Numerical Dynamics Model 23

2.4.3 Numerical WEC Investigation 30
2.5 Discussion 33
2.6 Conclusions 34

3 Experimental and numerical comparisons of self-reacting point absorber wave energy converters in irregular waves 42
3.1 Introduction 43
3.2 Literature Review 43
3.3 Methods 45
3.3.1 Numerical Methods 45
3.3.2 Experimental Methods 49
3.4 Results 52
3.4.1 Experimental Results 52
3.4.2 Validation of Time Domain Model 54
3.4.3 General Performance of WECs 61
3.4.4 Sensitivity of WEC Performance to Drag coefficients 63
3.4.5 Alternative Performance Measures 64
3.5 Conclusions 65

4 Experimental and numerical simulations of moored self-reacting point absorber wave energy converters 66
4.1 Introduction 67
4.2 Literature Review 67
4.3 Numerical Methods 68
4.3.1 Linear Hydrodynamics 68
4.3.2 Dynamics in the time domain 68
4.3.3 Selection of PTO damping 69
4.4 Experimental Methods 69
4.4.1 Experimental Setup 69
4.4.2 Decay Tests 71
4.4.3 Response Amplitude Operators 72
4.4.4 Power Conversion 72
4.5 Parameter Identification Results 72
4.5.1 Decay Tests 72
4.5.2 Response Amplitude Operators 75

4.6 Power Conversion Results 77
  4.6.1 Pitch and Roll Oscillations 77
  4.6.2 Mooring forces and PTO dynamics 80
  4.6.3 Power Conversion 81
4.7 Assessment of Strakes for Pitch Mitigation 84
  4.7.1 Strake Design 84
  4.7.2 Simulation Results 86
4.8 Conclusions 90

5 Conclusions 91

A Representative sea condition distributions 93

B WEC Model specifications 94

C Irregular Wave Conditions & Analysis 96

D Inviscid Hydrodynamic Coefficients 98

E The Effect of Radiation Coupling 103

F Tank Wall Effects 105

Bibliography 107

List of Tables

Table 2.1 Tank Specifications 14
Table 2.2 Summary specifications of heave constrained WEC models . . . 17

Table 3.1 Selected c_{pto} values and targeted wave conditions. 49
Table 3.2 Sensitivity of WEC performance to viscous drag coefficients. . . 63
Table 3.3 Alternative WEC performance measures off West Coast, BC, Canada. 64

Table 4.1 Selected c_{pto} values for each test wave frequency 70
Table 4.2 Summary specifications of moored WEC models 70
Table 4.3 Summary of results for WEC A with and without strakes. . . . 89
Table 4.4 Summary of results for WEC B with and without strakes. 89

Table B.1 Detailed specifications of experimental WEC models 94

List of Figures

Figure 2.1 Schematics of the two WEC model configurations. 6

Figure 2.2 Panel meshes used for BEM analysis. 10

Figure 2.3 Expt. setup of heave constrained WECs with wave probes. . 16

Figure 2.4 Expt. vs. BEM derived total damping coefficients. 21

Figure 2.5 Expt. vs. BEM derived heave added mass coefficients. 22

Figure 2.6 Expt. vs. BEM heave excitation force for reacting body A. . 23

Figure 2.7 Expt. vs. BEM derived excitation force for reacting body B 24

Figure 2.8 Float expt. vs. BEM derived excitation force 25

Figure 2.9 Expt. vs. frequency domain model reacting body heave RAOs. 26

Figure 2.10 Expt. vs. numerical PTO damping and power conversion . . 28

Figure 2.11 Displacements of power converting heave constrained WECs. 36

Figure 2.12 Sample PTO force time-series at two wave frequencies. . . . 37

Figure 2.13 PTO force noise variance. 37

Figure 2.14 Normalized power of heave constrained WECs with passive damping vs. reactive PTOs. 38

Figure 2.15 WEC motions with passive damping vs. reactive PTOs. . . . 39

Figure 2.16 Effect of stroke constraints on power conversion. 40

Figure 2.17 Full scale heave constrained WEC power vs. theoretical bounds. 41

Figure 3.1 Panel meshes used for BEM analysis of the WECs. 46

Figure 3.2 Power transport weighted occurrence contours for a West coast BC location. 51

Figure 3.3 Free decays of heave constrained WEC reacting bodies. . . . 53

Figure 3.4 Objective functions for reacting body drag and friction coefficient identification. 54

Figure 3.5 Expt. vs. time domain model heave RAO's for WEC reacting bodies. 55

Figure 3.6 Surface elevation, PTO stroke, and power capture. 58

Figure 3.7 Surface elevation, PTO stroke, and power capture (zoomed). 59
Figure 3.8 Expt. vs. numerical WEC power in irregular waves. 60
Figure 3.9 RMSE of expt. vs. time domain model stroke in irregular waves. 60
Figure 3.10 Contours of power output for WECs in panchromatic seas. . 61
Figure 3.11 Capture width contours for heave constrained WECs. 62
Figure 3.12 WEC power converted over 9 years off West Coast, BC. . . . 62

Figure 4.1 Images of WEC physical models. 67
Figure 4.2 Experiment setup of moored WECs. 71
Figure 4.3 Expt. vs. simulated heave decay results 73
Figure 4.4 Expt. and simulated sway decay results. 74
Figure 4.5 Expt. vs time simulation heave RAOs of WEC reacting bodies. 76
Figure 4.6 Combined pitch/roll motion of moored WECs in regular waves. 78
Figure 4.7 Pitch/roll motion for moored WECs in regular waves. 79
Figure 4.8 Mooring tensions for moored WECs in regular waves. 80
Figure 4.9 PTO force and stroke of moored WECs in regular waves. . . 81
Figure 4.10 Expt. and simulated power output of moored WECs in regular waves. 82
Figure 4.11 Normalized average power of moored WECs in regular waves. 83
Figure 4.12 Panel meshes of moored WECs fitted with pitch/roll damping strakes. 85
Figure 4.13 Simulation results of WEC A with and w/o strakes. 87
Figure 4.14 Simulation results for WEC B with and w/o strakes. 88

Figure B.1 External dimensions of experimental WEC models 95

Figure C.1 Variance density spectra from wave probe measurements. . . 97

Figure D.1 Added mass coefficients from BEM analysis 99
Figure D.2 Radiation damping coefficients from BEM analysis 100
Figure D.3 Excitation force coefficients from BEM analysis. 101
Figure D.4 Radiation and diffraction kernels in heave. 102

Figure E.1 Effect of radiation coupling impedance Z_c on power 103

Figure F.1 Regression results of two wave probe signals. 106

ACKNOWLEDGEMENTS

I would like to thank my father Brian, for teaching me the passion for the confluence of knowledge and craft, my mother Delores, for her unwaivering support while teaching me how to be a great parent and live a joyful life, and my brother Vance, for being himself. I'll always be greatful for the support from the brilliant, loving, talented, Shentae and the kind, beautiful, and adventurous Anna. The support from dear family and friends, Grandma Vance, Grandma Joan, Donna and Darreld, Joy, Nick and Otis, Aunt Michelle, Uncle John, Cousins Beatty, the Kouri family, Kama and Lucas, the McKenty clan, the Ditrich clan, and the McCleans have been a huge help on this journey.

I have a ton of thankfulness and respect for Dr. Buckham, for pushing me into new territory while always supporting my choices; For Dr. Wild, for his sage advice and understanding of engineering and non-engineering matters; For Jochem Weber for his mentorship; For Peter Ostafichuk—the first engineer to believe in my engineering; and the late Trevor Williams—whose passion and dedication to sustainable energy systems will always be an inspiration.

This work would not have been possible without Justin Blanchfield, Mike Optis, Mark Mosher, Stephen Lawton, Clayton Hiles, Jon Zand, Matt Hall, Mike Shives, Bryce Bocking, Kush Bubbar, Andrew Zurkinden, Francesco Ferri, Arthur Pecher, Izan le Crom, Thomas Roc, Yukio Kamizuru, and Sam Harding who all started as colleagues and have become life-long friends.

I gratefully acknowledge the support from the Pacific Institute for Climate Solutions, Natural Resources Canada, Natural Sciences and Engineering Research Council of Canada, British Columbia Innovation Council, Trevor Williams Memorial foundation, International Network for Offshore Renewable Energy, and Marine Renewables Canada.

DEDICATION

To my grandfather, Dr. James Beatty

Chapter 1

Introduction

The major aim of this thesis is to evaluate the dynamic motions and power conversion characteristics of self-reacting point absorber (SRPA) wave energy converters (WECs), in typical operating conditions, through both experimental and numerical approaches. Two WECs that characterize a particular design space of SRPAs are evaluated in three main sets of conditions. In the first set of conditions, the WECs are subjected to vertical motion constraints and monochromatic waves. In the second set of conditions, the WECs are subjected to vertical motion constraints and panchromatic waves. In the last set of conditions, the WECs are softly moored and subjected to monochromatic waves.

1.1 Background

Classified by external shape, three general categories have been identified for WECs [9, 19]: *Point absorbers* have a small horizontal dimension compared to the incident wavelengths, *attenuators* are of comparable dimension to the wavelengths in the direction of the waves, and *terminators* are of comparable dimension to the wavelength purpendicular to the direction of the waves. Classified by operating principle, three further categories have been identified for WECs: *Wave activated bodies*, *oscillating water columns*, and *overtopping devices*. This thesis focusses on WECs classified as point absorbing wave activated bodies.

Wave activated body WECs exploit the dynamic and hydrodynamic properties of moving bodies to absorb and convert ocean wave energy into useful forms. To perform this conversion, dynamic forces and body motions must be transferred to a power take-off[1](PTO). One design strategy is to locate the PTO between a single moving body and a ground fixed structure. Because their anchoring systems must withstand loads due to both power production and station-keeping, WECs with ground fixed reaction structures can require costly anchoring solutions, tend to be limited to locations with relatively shallow water depth, and typically require the power production equipment to be housed under water. An alternative design strategy, that may alleviate such challenges, is to locate the PTO between a moving body and second moving body. A WEC employing this alternative strategy is said to be *self-reacting*.

Among self-reacting WECs, some design concepts locate the PTO between a moving body and an oscillating body housed internally within the first body. For example, the PS-Frog device [37] features a floating hull that moves predominantly in the pitch and surge directions and the PTO reacts against an internally housed translating reaction mass. Further, the SEAREV [53] and Penguin [65] devices both feature floating hulls that move in combinations of pitch, roll, and surge directions with the PTOs reacting against internally housed rotating pendulums. Other self-reacting WEC concepts place the PTO between a moving body and a second external body. A benefit of this strategy is the potential for greater power absorption because the second body is exposed to hydrodynamic forces that can benefit power production [16].

This thesis focusses on SRPAs that operate primarily in the heave direction, locate the PTO between two axisymmetric moving bodies that are external and thus subjected to hydrodynamic forces.

---

[1] often a hydraulic system, an electrical generator system, or a hybrid hydraulic-electrical system.

1.1.1 The significance of this research

Two self-reacting point absorber WECs that have been in industrial development by different organizations over the past two decades are studied in this thesis. It has become apparent that, due to the financial, business, and marketing pressures on wave energy conversion technology start-up companies, a lack of engineering perspective has been applied so far. The results of this research provide a foundation for the wave energy community to determine:

- whether SRPA's are worthwhile compared to other WEC configurations
- which of the two archetypal self reacting point absorber design strategies is superior
- the key performance limitations of the self reacting point absorber configurations, and
- proposed solutions the mitigate the limitations.

1.2 Key Contributions

I make *four* contributions which my dissertation validates:

1. An extension of Budal's theoretical upper bound for single body WECs to two-body WECs.
2. A method to simultaneously extract Morison drag and Coulomb friction coefficients from decay tests of under-damped, floating bodies.
3. Comprehensive performance benchmarks for two, archetypal, SRPA WECs.
4. A method to mitigate power conversion degradation due to resonant pitch motions of SRPA WECs.

1.3 Outline

The remainder of this thesis is laid out as follows:

Chapter 2 describes and develops theoretical upper bounds on SRPA power conversion, and assesses the performance of the SRPA designs, constrained to heave motion, in regular waves.

Chapter 3 uses a combination of experiments and time domain simulations to assess the performance of SRPA designs, constrained to heave motion, in irregular waves. The mean annual energy production from each SRPA in the wave climate off the Pacific Coast of Canada is computed using the validated time domain simulation.

Chapter 4 extends both the experimental and numerical analyses to assess the motion dynamics and power conversion performance of the SRPA designs fitted with mooring systems in regular waves.

Chapter 5 then summarizes the key conclusions of the thesis.

Appendices provide details of the physical and numerical models used, and supplementary information referred to in the main text.

Chapter 2

Experimental and numerical comparisons of self-reacting point absorber wave energy converters in regular waves

This chapter is based on the contents of the paper:
Beatty, S., Hall, M., Buckham, B., Wild, P., Bocking, B., "Experimental and numerical comparisons of self-reacting point absorber wave energy converters in regular waves", *Ocean Engineering*, 104, pp. 370-386. (2015)

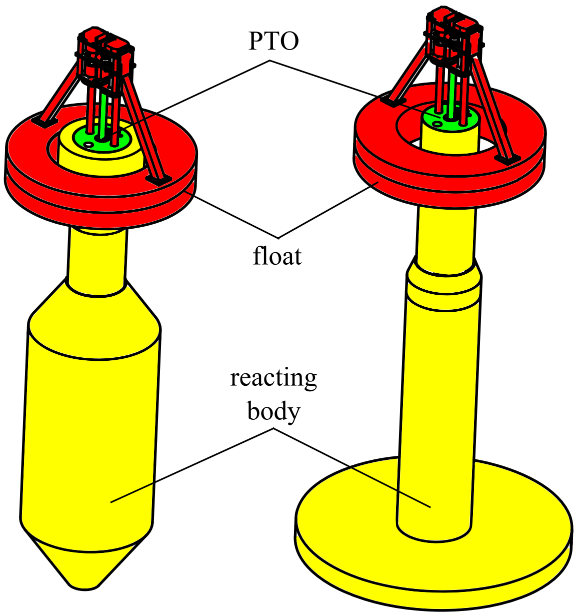

Figure 2.1: Schematics of the two WEC model configurations — WEC A (left) features a bulbous tank and WEC B (right) features a large heave plate. Both WECs have identical float shapes, drafts, PTOs, and instrumentation systems

2.1 Introduction

Self-reacting point absorbers (SRPAs) are wave energy converters (WECs) that extract energy from the relative motion between two or more bodies. SRPAs are axisymmetric and are intended to operate primarily in the heave (vertical) direction. SRPAs typically employ a buoyant, surface piercing body referred to as the *float* which reacts against a second surface piercing body referred to as the *reacting body*, to generate mechanical energy which is extracted by means of a *power take-off* (PTO). Two design strategies are evident in current SRPA devices. The key difference between these strategies is the shape of the reacting body, as shown in Figure 2.1. The external geometries of two SRPA designs that are the focus of this study are shown in Figure 2.1. The first, denoted WEC A, is modeled after a WaveBob$^{\text{TM}}$(WaveBob Ltd., Ireland) device, featuring a positively buoyant float and a streamlined reacting body with an integral water ballast tank. The second, denoted WEC B, is modeled after a PowerBuoy®(Ocean Power Technologies Inc, USA) device, featuring the same float as WEC A, but with a reacting body that has fitted with a large diameter heave plate.

The first objective of this work is to systematically compare the power production and heave motion amplitudes of WEC A and WEC B, given independently optimized PTOs. The second objective is to assess the effects of alternative relative motion constraints and PTO control strategies on power production and dynamic motions.

2.2 Literature Review

Previous experimental and numerical studies of SRPAs focus predominantly on single device designs [22, 31, 32, 64, 25, 5, 13, 6, 26, 11, 66]. From these studies, it is difficult to draw equitable comparisons among different SRPA designs due to differences in mooring and PTO control strategies and insufficient characterization of experimental and numerical uncertainties. Only three comparative studies of WEC devices have been identified. Fifteen WECs of various classes were compared experimentally in terms of capture width and cost by Meyer et al[38]. Eight WECs of different class and operating principle were compared by Previsic et al[50] at a high level based on performance data reported by device developers. Babarit et al[2] conducted numerical analyses to compare eight distinct WEC designs, including one SRPA based on mean power production and key cost indicators. No detailed studies that compare the performance of alternative SRPA designs have been identified.

Similarity of Froude number is widely relied upon as a scaling law for the estimation of full scale WEC behaviour from experimental model WEC behaviour. Because the dynamic behaviour is highly dependent on the PTO force, the choice of PTO at the experimental scale is critical to ensure dynamic similarity. Previous experimental studies of scale model WEC devices have used a variety of systems to apply reactions that represent the forces applied to a WEC by a PTO device. In this discussion, these systems are referred to PTO simulators. The PTO simulator must provide user-definable forces, dynamically similar to full scale WEC PTOs, that are adjustable to meet the desired PTO control scheme (*i.e.* passive damping, reactive, latching, etc.). Given a geometric scale ratio of α between experimental model and full scale WECs, under Froude scaling, the power absorption scales with $\alpha^{3.5}$. With such sensitivity in the scaling law, power losses from forces that are not dynamically similar, such as friction and mechanical backlash, must be minimized because they will obfuscate the power absorption results [47].

Some researchers have used PTO simulators based on passive elements, such as oilfilled dash-pots and pneumatic dampers [21, 4] even though the range and resolution of PTO force adjustability is limited. Flocard and Finnigan [21] reported using only three PTO damping settings from a PTO simulator based on a rotational viscous dashpot. Bailey and Bryden [4] reported using only five PTO damping settings from a PTO simulator based on translational pneumatic dampers. Pecher et al [48] reported testing six PTO settings on a PTO simulator based on adjustable sliding friction. Although the simplicity and low cost of passive element PTO simulators is attractive, these systems provide only low resolution adjustments of the PTO force and do not allow investigations of alternative PTO control schemes.

Actively controlled PTO simulators on the other hand, enable investigations of all conceivable PTO control schemes. Both Taylor and Mackay [60] and Lopes et al [35] designed and fabricated PTO simulators based on eddy current brakes that enable PTO control strategies beyond passive damping. Another actively controlled PTO simulator concept, requiring less complex electro-mechanical design than eddy current based systems, are feedback controlled electric motors. Feedback controlled motors, now common as off-the-shelf products for automation applications, can provide an arbitrarily defined PTO force with high resolution and repeatability when used in conjunction with a real-time controller and suitable instrumentation. Example implementations, reported by Villegas [62] and Zurkinden et al [69], used linear motors controlled in real-time by a feedback loop with the process variable being PTO force. Actively controlled PTO simulators can also function as an actuator for experimental identification of hydrodynamic coefficients. Because the functional benefits of actively controlled PTO simulators outweigh the detriments of increased complexity and cost over passive PTO simulators, a PTO simulator based on a feedback controlled linear motor was used in this work.

To facilitate the use of impedance matching strategies for determining the PTO behaviour that maximizes power absorption in regular waves, Falnes proposed the concept of mechanical impedance for dynamic analysis of single body point absorbers [17]. Falnes' later extension of the impedance matching methods for two-body SRPA concepts [16] are drawn upon in this work to select the optimum PTO impedance as a function of frequency.

2.3 Methods

Comparative analyses of WEC A and WEC B were performed using a combination of numerical and experimental methods. The numerical methods consisted of: a linear hydrodynamic analysis (Sec. 4.3.1); a heave-constrained dynamics model with implementation of impedance matching (Sec. 4.3.2); an application of a closed form relation for power capture with motion constraints (Sec. 2.3.1); and, finally, two theoretical upper bounds on power capture (Sec. 2.3.1). The experimental work was conducted using a reconfigurable, heave-constrained, 1:25 scale, WEC model in a wave flume of 2 m depth (Sec. 2.3.2). The experimental methods consisted of parameter identification and validation tests. The parameter identification consisted of radiation and diffraction tests. In the radiation tests, the PTO was utilized as an actuator to induce WEC body motions for identification of frequency dependent added mass and damping parameters in a quiescent tank (Sec. 2.3.2). In the diffraction tests, direct measurements were taken of the wave excitation loads on the WEC bodies while held fixed in regular waves (Sec. 2.3.2). The validation process consisted of application of identified hydrodynamic coefficients in the numerical dynamics model and subsequently testing the numerical dynamics model's validity against data from two experimental scenarios in regular waves. In first scenario, the numerical model output is compared to test data of each body's free response in the absence of a PTO in the form of response amplitude operators (Sec. 4.4.3). In the second scenario, the numerical model's output is compared with power capture test data where the PTO force was set to an optimized value that was specific to each of WECs A and B (Sec. 4.4.4).

2.3.1 Numerical Methods

Hydrodynamics

The Boundary Element Method (BEM) code WAMIT [63] was used to obtain the inviscid hydrodynamic coefficients for comparison to experimental results. The panel meshes used in the analyses of WEC A and B are shown in Figure 2.2. The water depth for the analysis is 2.0 m. The spatial domain is assumed to have infinite size (*i.e.* tank wall effects were neglected). A two-body analysis of each WEC configuration was performed so that hydrodynamic effects of the float and reacting body were assessed in the presence of the other body. For each body, the added mass, radiation damping, and excitation forces are generated as a function of frequency using the BEM analysis.

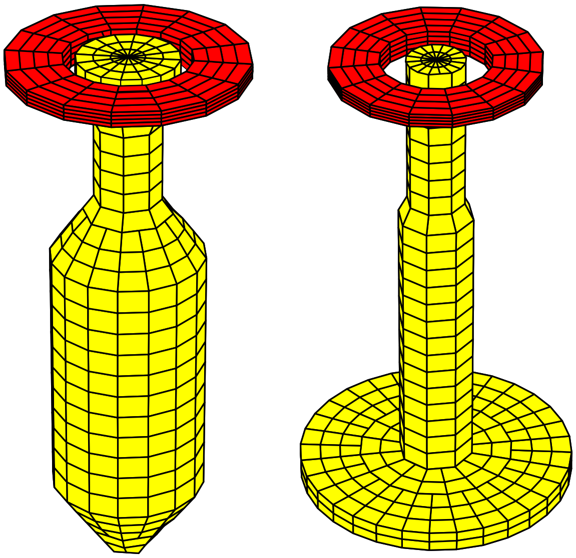

Figure 2.2: Panel meshes used for BEM analysis.

Dynamics

A linear, heave constrained, dynamics model in the frequency domain was used to identify the optimal PTO tuning for the power capture experiments of WECs A and B. Newton's second law for the two-body system, constrained to heave motion, can be written as:

$$\underline{Z}\vec{U} = \vec{f_e} \tag{2.1}$$

where $\underline{Z}$ is the complex impedance matrix given by Eq. (2.2). The wave excitation force complex amplitude for body j (float $j = 1$, reacting body $j = 2$) is $\hat{f}_{ej} = X_j e^{i\phi_j}$ where X_j and ϕ_j are the excitation force amplitude and phase with respect to the wave elevation. For each body, $\hat{f}_{ej}$, obtained from either BEM analyses or diffraction parameter identification tests, is inserted into the excitation force vector $\vec{f_e} = [\hat{f}_{e1}\ \hat{f}_{e2}]^T$. The complex amplitudes of the body velocities are given by $\vec{U} = [\hat{U}_1\ \hat{U}_2]^T$. Complex amplitude of body displacement can be expressed as $\hat{\xi}_j = \hat{U}_j/i\omega$. The intrinsic mechanical impedance is given in Eq. (2.3). The experimental results from the radiation experiments provide the added mass $A_{jj}(\omega)$ and the total damping, $(B_{jj}(\omega) + C_{vj}(\omega))$, which contains both radiation damping, $B_{jj}(\omega)$, and linearized viscous drag, $C_{vj}(\omega)$. The hydrodynamic coupling between the float and reacting body is represented by Z_c. The force applied by the PTO between the float and reacting body is written as $F_{pto} = -Z_{pto}\hat{U}_r$ where the complex amplitude of the relative float-reacting body velocity is $\hat{U}_r = \hat{U}_1 - \hat{U}_2$. The impedance of the PTO acting between the float and reacting body is Z_{pto} and is given in Eq. (2.4).

$$\underline{Z} = \begin{bmatrix} Z_{11} + Z_{pto} & Z_c - Z_{pto} \\ Z_c - Z_{pto} & Z_{22} + Z_{pto} \end{bmatrix} \tag{2.2}$$

$$Z_{jj} = (B_{jj}(\omega) + C_{vj}(\omega)) + i\omega\left(m_j + A_{jj}(\omega) - \frac{k_j}{\omega^2}\right) \tag{2.3}$$

$$Z_{pto} = c_{pto} + i\omega\left(m_{pto} - \frac{k_{pto}}{\omega^2}\right) \tag{2.4}$$

An analytical solution [16] to the optimal PTO impedance *in regular waves* is applied to WECs A and B in power capture tests assuming $Z_c = 0$[1]. If Z_{pto} is constrained to real values only, the PTO behaves as a passive dashpot with damping coefficient c_{pto}, and the optimal PTO impeance is given by Eq. (2.5).

$$Z_{pto}^{\text{Passive}} = c_{pto} = \left|\frac{Z_{11}Z_{22} - Z_c^2}{Z_{11} + Z_{22} + 2Z_c}\right| \tag{2.5}$$

If Z_{pto} is allowed both real and imaginary terms, then the PTO behaves as a passive dashpot with damping coefficient c_{pto} in addition to behaving as an actuator with inertia and stiffness coefficients m_{pto} and k_{pto}, respectively. In this case, the control regime is sometimes referred to as complex conjugate control [41] but herein will be termed *reactive control* as done in the works of Hals and Falnes [24, 18]. The optimum PTO impedance is given by Eq. (2.6), where $*$ denotes complex conjugate.

$$Z_{pto}^{\text{Reactive}} = c_{pto} + i\omega\left(m_{pto} - \frac{k_{pto}}{\omega^2}\right) = \left(\frac{Z_{11}Z_{22} - Z_c^2}{Z_{11} + Z_{22} + 2Z_c}\right)^* \tag{2.6}$$

When the PTO control is changed from a passive damping to reactive control there are known power capture improvements to be gained. In addition to the increased

---

[1] Results from the BEM analysis with WAMIT yield relatively small float-reacting body radiation coupling terms; As a result, they were disregarded in experiments. The frequency dependent coupling coeeficients are provided in Appendix D. Further details on the impact of including $Z_c \neq 0$ in the dynamics model defined by Eqs. (2.2),(2.5),(2.7) are provided in Appendix E. The impact is calculated using the numerical model only; No experiments on radiation coupling were conducted.

complexity of the PTO design for provision of reactive power, there are important consequences of such a scheme in terms of motion dynamics and structural loads. The power capture in the frequency domain is equal to the time average power dissipated across the resistive load of the power take-off, resulting in Eq. (2.7).

$$P = \frac{1}{2} c_{pto} |\hat{U}_r|^2 \tag{2.7}$$

Motion Constraints

Relative motion constraints are important for the practical design of SRPAs. There is a limit to the total stroke available for the hydraulic cylinders or other mechanisms that are commonly featured on PTOs for SRPAs. If the PTO is not adequately controlled, wave forces are unexpectedly high, or no braking system exists, excessive PTO stroke lengths may occur. One solution to this problem is to adjust the PTO force to constrain relative motion within the allowable range. However, such a strategy may reduce power capture. The trade-off between power capture and maximum allowable stroke for the SRPAs is investigated in this work.

First, using the methods of Falnes [16], the two-body dynamics model, given by Eq. (2.1), is translated into the equivalent one-body model where the independent variable becomes $\hat{U}_r$ instead of the vector $\vec{U}$. Second, given that both power capture (Eq. (2.7)) and the equivalent one-body model of an SRPA are functions of $\hat{U}_r$, the following relation given by Evans [15] for a one body WEC necessarily applies to the power capture of the SRPA.

$$P_{\text{constr}} = \{1 - (1 - \delta)^2 H(1 - \delta)\} P \tag{2.8}$$

where ϵ is the maximum allowable relative float-reacting body displacement, $\delta = \epsilon / |\hat{\xi}_2 - \hat{\xi}_1|$, $H(x)$ is the Heaviside step function ($= \{0, 1\}$ for $x = \{< 0, > 0\}$ respectively), and P is the optimal power capture without a displacement constraint.

Upper Bounds on Power Capture

There are two known theoretical upper bounds on power capture for point absorber WECs. The first upper bound is based on the optimum radiation pattern for single point absorbers operating in heave, Eq. (2.9) [14]. The bound applies to one-body point absorbers and two-body SRPAs. Here, J denotes the wave power transport per unit length of wave crest (W/m) and k is the wave number (rad/m).

$$P \leq \frac{J}{k} \tag{2.9}$$

The second upper bound, known as *Budal's upper bound*, is based on the maximum utilization of the wave excitation force assuming the WECs oscillations are optimal and the WEC's maximum allowable PTO stroke achieved. For single point absorbers, Budal's upper bound is shown to be more restrictive at low wave frequencies/long wave periods than Eq. (2.9), [19, 61]. An extension of Budal's upper bound for application to SRPAs devices shall be indentified. Falnes' [18] Eq. (6.5) states the time-averaged power available to a single body WEC from the waves is:

$$P_e = \overline{f_{e,j}(t)U_j(t)} = \frac{1}{2}|\hat{f}_{e,j}||\hat{U}_j|\cos(\gamma_j). \tag{2.10}$$

The first step in the derivation of Budal's upper bound is stating that the γ_j, the phase between the body's velocity and the excitation force is optimal (ie. $\gamma_j = 0$ naturally or by control), therefore the following inequality can be developed:

$$P \leq P_e \leq \frac{1}{2}|\hat{f}_{e,j}||\hat{U}_j|. \tag{2.11}$$

For a single body point absorbing WEC, it is suitable for the upper bound to substitute $|\hat{f}_{e,j}|$ with only the buoyancy force contributions from the excitation force because inertial terms are subtractive; however, for two-body SRPAs, the fluid inertial contributions from the excitation force must be accounted for because they can be used to the increase the total magnitude of force across the PTO—an effect known as force compensation [16]. In the extension of Eq. (2.11) to two-body SRPAs, an analogous excitation force magnitude must be identified. Assuming the PTO is locked ($Z_{pto} = \infty$), Falnes [16] provides the excitation force induced in the PTO from waves, $\hat{f}_0$ as follows:

$$\hat{f}_0 = \frac{1}{2}\left(\hat{f}_{e,1} - \hat{f}_{e,2} - \frac{(\hat{f}_{e,1} + \hat{f}_{e,2})(Z_{11} - Z_{22})}{Z_{11} + Z_{22} + 2Z_c}\right) \tag{2.12}$$

Using Eq. (2.12) along with the relative velocity $\hat{U}_r = \hat{U}_1 - \hat{U}_2$, the relative velocity magnitude, an inequality for SRPAs is given by Eq. (2.13).

$$P \leq P_e \leq \frac{1}{2}|\hat{f}_0||\hat{U}_r| \tag{2.13}$$

Now $|\hat{U}_r|$ can be replaced by the maximum float-reacting body relative displacement amplitude afforded by the SRPA design, $|\hat{U}_{r,max}| = \omega s_{\max}$ which is set to 0.08 m for the WECs in this work. The excitation forces $|\hat{f}_{e,j}|$ are obtained from BEM analysis here; however, these are sometimes estimated from the small-body approximation [16, 61]. The final expression for the revised version of Budal's upper bound is given by Eq. (2.14).

$$P \leq \frac{1}{2}|\hat{f}_0|\omega s_{\max} \tag{2.14}$$

2.3.2 Experimental Methods

The key mechanical design requirements of the tank model for this study are that it must: (1) allow for identification of frequency dependent hydrodynamic coefficients; (2) incorporate an adjustable PTO with suitable instrumentation for mechanical power absorption measurements; and (3) allow reconfiguration of the reacting body shape. Detailed descriptions of the experimental hardware including the wave tank, model design to meet the requirements are described in the following subsections. The targeted ocean conditions are the non-extreme seas off the Pacific Coast of British Columbia accounting for the bulk of the WECs' forecasted yearly energy production.

Experimental Setup

The facility used to undertake the experimental program was Memorial University's Ocean Engineering Research Center located in St. John's Newfoundland, Canada. Details on the tank are given in Table 2.1. The tank dimensions and performance envelope provided key constraints when determining the external dimensions of the experimental WEC models. Further constraints on the size of the experimental model

Table 2.1: Tank Specifications

Parameter	Value	Units
Length	58	m
Width	4.57	m
Maximum water depth	2.2	m
Maximum wave height (regular waves)	0.7	m
Maximum wave height (irregular waves)	0.2	m
Wavelengths	0.9 - 17	m
Wave period	0.76 - 4.16	sec

were: (1) it should as large as necessary to represent the targeted physical phenomena on the full scale devices with minimal scaling distortions from viscous drag; (2) it should be small enough to maintain reasonable costs of construction and to avoid problems with physical handling; (3) its diameter should not exceed 1/5 of the tank width (0.9 m) to avoid the hydrodynamic effects of tank walls [7, 47].

Since, full scale SRPAs have float diameters of $\approx$ 15 m, reacting body drafts of $\approx$ 35 m, and are deployed in depths of $\approx$ 50 m, the ratio of water depth from full scale to tank scale results in a geometric scale ratio of 1:25. Applying Froude similarity, at 1:25, to the wave maker capability shows that the tank's maximum wave height and period range cover the targeted ocean conditions. Further, the model scale float diameter becomes 0.59 m—less than 1/5 the tank width. If the geometric scale is increased from 1:25, the wave period range of the tank, experimental model size/cost, and proximity of model draft to the tank bottom all become critical constraints. Thus, a geometric scale of 1:25 was the largest physical scale found to meet all of the requirements. Summary specifications of the physical models are given in Table 4.2. Figure 2.3 shows the locations of the wave probes relative to the WECs and the heave motion constraint apparatus. Eqs. (2.5) and (2.6) show that the PTO impedance for optimum power absorption depends on each WECs own hydrodynamic impedance. Thus, to ensure an equitable study, each WEC must be tested with a PTO that is uniquely impedance matched. A research challenge results: to provide an impedance matched PTO that is unique to each WEC design but facilitates equitable comparisons between designs.

A feedback-controlled linear actuator was used for PTO simulation on this project as was done by Villegas [62] and Zurkinden et al [69]. The PTO simulator has two control modes. First, a position feedback mode enables the linear actuator to carry out preprogrammed motions in still water for hydrodynamic coefficient extraction. Second, a force feedback mode was used in tests with waves which enabled the linear actuator to exert the desired state dependent force for PTO simulation. The control systems were developed in NI Labview and implemented in real time on an NI PXI chassis running at 50 Hz for sampling and control. The linear motor (LinMot PS01-37x120, Elkhorn, Wisconson, USA), exerts 250 N maximum force, has a maximum travel of 0.28 m, and weighs under 3kg. Relative displacements are measured with a non-contacting laser displacement sensor (Micro-Epsilon optoNCDT-1402-600 with a range of 600 mm and resolution of 80 μm. The PTO force was measured by a 500 N capacity, S-type, tension/compression load cell. Accelerations of the float and

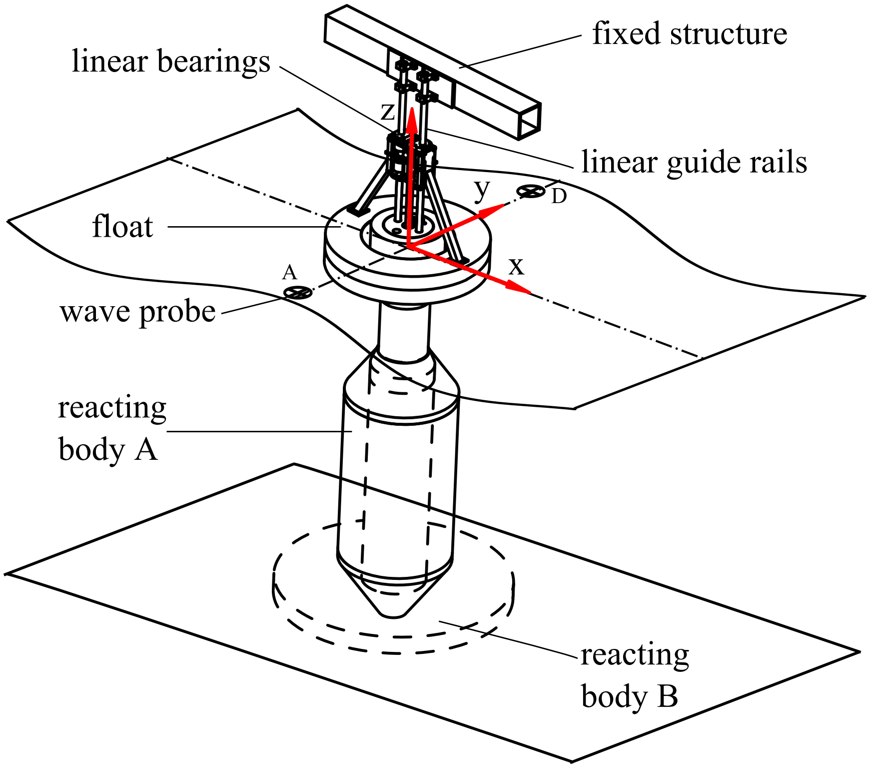

Figure 2.3: Experiment setup illustrating the method for constraining motions to heave direction. Tank width, depth, wave length, height are not to scale. There are two linear guide rails mounted to the tank structure from above. Both the float and the reacting body have linear bearings that run on the linear guide rails. Wave probes, labelled “A” and “D,” are located at y =-1 m and y =1 m.

Table 2.2: Summary specifications of heave constrained WEC models

	WEC A	WEC B
Draft	1.4m	1.4m
Displacement	127kg	87.5kg
Float outer diameter	0.60 m	0.60 m
Float hydrostatic stiffness	2000 N/m	2000 N/m
Reacting body hydrostatic stiffness	510 N/m	223 N/m

reacting bodies were measured via accelerometers (Analog Devices ADXL203) with +/-1.7 g range. A Kalman filter was used in the Labview code to synthesize a real-time velocity signal from the measured displacement and acceleration signals.

Radiation Tests

The objective of the radiation tests was to identify frequency dependent hydrodynamic coefficients. These tests comprised pre-programmed heave motions of 3-8cm in amplitude and 120 seconds in duration using the linear motor as a position-controlled actuator in a quiescent tank. The displacement, acceleration, and heave force exerted by the actuator were logged. Both the float and reacting bodies were tested while holding the other body fixed for each of WECs A and B.

For each oscillating body (j), four quantities were logged: displacement $x(t)$, velocity $\dot{x}(t)$, acceleration $\ddot{x}(t)$, and actuator force $F(t)$. Extraction of total damping and added mass from the logged time series data is based on the linear hydrodynamic model given by Eq. (2.15).

$$(m_j + A_{jj}(\omega))\ddot{\xi}(t) + (B_{jj}(\omega) + C_{vj}(\omega))\dot{\xi}(t) + k_j\xi(t) = F(t) \tag{2.15}$$

After removing starting and stopping transients from the logged data, the total damping coefficient, $(B_{jj}(\omega) + C_{vj}(\omega))$, and added mass, $A_{jj}(\omega)$, were extracted separately in a two-stage process.

In the first stage, the total damping coefficient was extracted from the time series data in three steps. (1) The time series were split into windows of data, of duration 1/2 oscillation period, each containing a *velocity* peak. (2), For each window, the added mass and total damping that satisfy Eq. (2.15) with minimum squared residuals were calculated. The added mass was rejected at this stage since its result is poorly resolved at velocity peaks. (3), the identified total damping coefficients were collected for all peaks of the $\dot{\xi}(t)$ time series, enabling a statistical analysis that yields the mean and standard deviation.

In the second stage, the added mass coefficient was extracted from the time series data similarly in three steps. (1) The time series were split into windows of data, of duration 1/2 oscillation period, each containing an *acceleration* peak. (2), For each window, the added mass and total damping that satisfy Eq. (2.15) with minimum squared residuals were calculated. The total damping was rejected at this stage since its result is poorly resolved at acceleration peaks. (3), the identified added mass coefficients were collected for all peaks of the $\ddot{\xi}(t)$ time series, enabling a statistical analysis that yields the mean and standard deviation.

A limitation of this experimental procedure arises when testing bodies with large hydrostatic stiffness. In this case, Eq. (2.15) is dominated by the buoyancy term, $k_j\xi(t)$, such that $F(t) - k_j\xi(t)$ is a small quantity, thus resulting in poorly resolved calculations for added mass and damping.

Diffraction Tests

The wave excitation forces in the heave direction on all bodies were measured in regular waves for frequencies of 1.5 to 4rad/s and for wave heights of 2cm, 4cm, 6cm, and 8cm. All diffraction tests were executed for each body with the other body held fixed at its equilibriumm position in the domain. Test durations were limited to 120sec to avoid longitudinal tank reflections. In these tests, the float and reacting body were held fixed while two load cells of 500N capacity measured the heave forces and two wave probes as shown in Figure 2.3 monitored the water surface elevation[2]. The excitation force magnitude and phase data were extracted from the force time series in three steps similar to the approach discussed in Section 2.3.2. First, the force time series was split into windows of data, of duration 1/2 wave period, each containing an excitation force peak. Second, for each window, the magnitude and phase of a sinusoid that has a minimum squared residual fit to the force data were identified. Third, a statistical analysis of the least squares optimal magnitudes and phases for all windows yields the mean and standard deviation.

---

[2] Although the wave probe signals likely include the diffraction effects due to the presence of the WEC, no attempt is made here to remove such effects.

Response Amplitude Operators

The free oscillation behavior of a floating body can be represented by its Response Amplitude Operator (RAO). A body's magnitude RAO is defined as the amplitude of the body's displacement, $|\hat{\xi}_j|$, normalized by the wave amplitude, η, as a function of frequency. A body's phase RAO is defined as the phase of the body's displacement with respect the wave, ϕ_j, as a function of frequency. Near their natural frequencies, the reacting bodies are expected to exhibit larger motion amplitudes in the absence of PTO forces than in the presence of PTO forces. As a result, RAO tests are useful for separately assessing the validity of numerical dynamics models for each floating body when undergoing large motion amplitudes.

Due to its buoyancy and high natural frequency, the float is a wave follower *i.e.* it moves in phase with the incident wave. However, the response of the reacting body is seen as a key differentiator between WECs A and B. Experimental identification of the heave RAOs of each WEC reacting body was done in two ways. The first method was done in regular waves. Separate regular wave tests were done at frequencies specifically chosen to identify the resonant responses of the bodies. The second method was done in low-pass filtered white noise waves. These waves contain broad band frequency content that allow the response as a function of frequency to be obtained from a single test using a DFT analysis. Similar to Roux et al [52], a modified periodogram technique (Welch's method) was applied to extract RAOs as smooth curves.

Power Capture

Tests of power capture for WECs A and B were done in regular waves of 4cm and 6cm heights, at 10 frequencies from 1.5 to 4.0rad/s. The optimum amplitude condition in regular waves, given by Eq. (2.5), was invoked to set the PTO damping level at each wave frequency for WECs A and B. The mean power capture for each test was calculated by Eq. (3.12), where $F_{pto}(t)$ is instantaneous PTO force signal and $U_r(t)$ is the instantaneous relative velocity signal.

$$P = \overline{P(t)} = \overline{F_{pto}(t)U_r(t)} \tag{2.16}$$

2.4 Results

2.4.1 Experimental Results

The results of testing to determine hydrodynamic parameters of each WEC are given in this section. These results are compared to hydrodynamic coefficients obtained from BEM analyses.

Radiation Tests

The total damping coefficients for reacting bodies A and B, derived from experiments and from the inviscid BEM analyses, are shown Figures 2.4a and 2.4b, for tests across the 3-8cm range of oscillation amplitudes. The plotted lines indicate the mean values and the error bounds indicate +/- one standard deviation, based on the analysis discussed in Section 2.3.2. There are three key observations to be made from Figures 2.4a and 2.4b. First, the experimentally derived total damping is one to two orders of magnitude greater than the BEM derived damping. Second, total damping of reacting body A is low compared to total damping of reacting body B. Third, an effect of oscillation amplitude on the experimentally derived total damping is evident for both reacting bodies. For reacting body A, an increase in oscillation amplitude tends to decrease the total damping coefficient. A converse trend is evident for reacting body B: an increase in oscillation amplitude tends to increase the total damping coefficient.

Interpreting the total damping results for the reacting bodies yields the following points. First, the experimentally derived total damping is much greater than the BEM derived damping for both reacting bodies because the BEM code accounts for the damping effect due to radiation of waves but does not account for viscous effects. Since radiation is a free surface phenomenon, and both reacting body geometries are small at the free surface, the radiation damping is negligible. It is clear that viscous effects are the dominant source of damping for both reacting bodies. Second, the experimental total damping for reacting body B is much greater than for reacting body A, as expected, due the viscous drag induced by the damper plate featured on reacting body B in comparison to the streamlined shape of reacting body A. Third, the observed variations of the experimental total damping with oscillation amplitude are explainable by considering the primary flow phenomena contributing to the drag force on each reacting body. For reacting body A's relatively streamlined shape, the

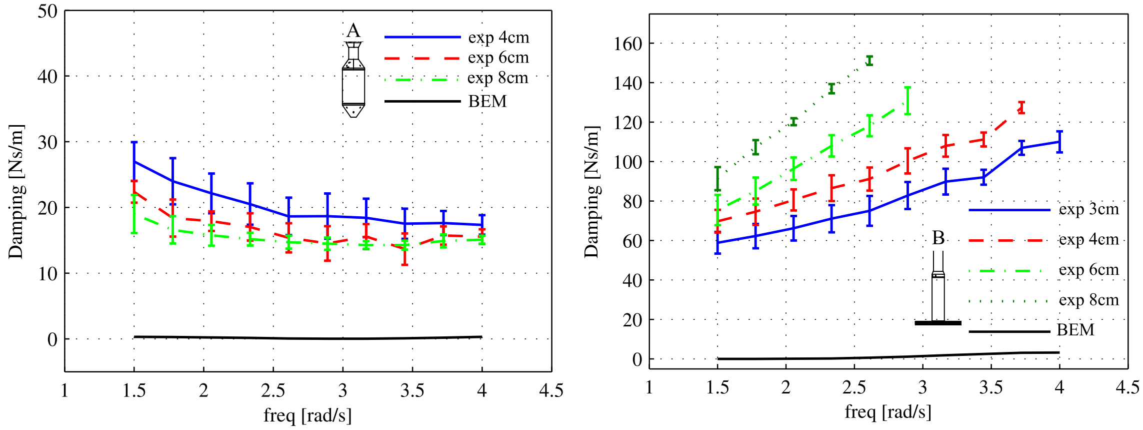

(a) Reacting body A. **(b)** Reacting body B.

Figure 2.4: Experimental and BEM derived total damping coefficients as a function of oscillation frequency, ω, and amplitude, ξ. Experimental results are shown with prefix 'exp.' for oscillation amplitude, ξ = 3cm, 4cm, 6cm, 8cm.

drag forces should be mainly friction drag (*i.e.* fluid shear stress on the hull walls). However, for reacting body B's damper plate shape, the drag forces should arise mainly from form drag (*i.e.* flow separation and vortex shedding).

Tao and Cai [58] showed for spars fitted with damper plates, and claim for truncated cylinders, that heave damping due to form drag increases dramatically with motion amplitude—via variation in the Keulegan-Carpenter number, $KC = 2\pi a/D$, where a and D are motion amplitude and characteristic body diameter respectively—and that friction drag remains relatively constant. Tao and Cai's results support the observed trends in Figure 2.4b but do not support the observed decrease of total heave damping with increasing motion amplitude for reacting body A in Figure 2.4a. This disagreement may have arisen from a combination of natural variation of the viscous drag of reacting body A's non-cylindrical shape with oscillation amplitude (*i.e.* $C_{v2} = f(Re)$) and the limitation of the numerical method discussed in Section 2.3.2.

The added mass coefficients for reacting bodies A and B derived from the experiments and from the inviscid BEM analyses are shown Figures 2.5a and 2.5b, for tests across a range of amplitudes and frequencies of oscillation. Key observations of the results are as follows. First, the added mass of reacting body A (10-20kg) is much lower than the added mass of reacting body B (210-230kg). Second, the magnitude of the added mass values derived from inviscid BEM analyses are in general agreement with the experimental results. Third, the experimental added mass results for react-

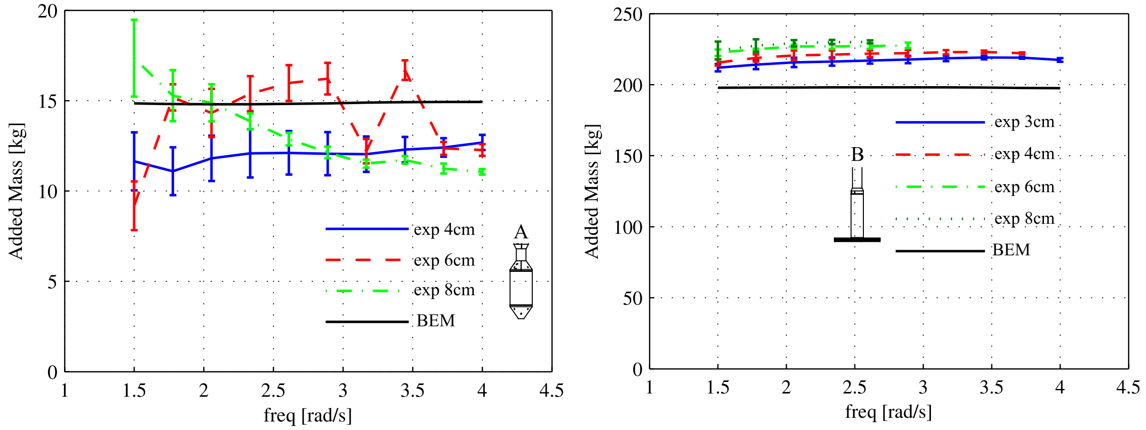

(a) Reacting body A.

(b) Reacting body B.

Figure 2.5: Experimental vs. BEM derived heave added mass coefficients as a function of oscillation frequency, ω and amplitude ξ. Experimental results are shown with prefix 'exp.' for oscillation amplitude, ξ = 3cm, 4cm, 6cm, 8cm.

ing body A exhibit variations with oscillation amplitude without any visible trends whereas, for reacting body B, they exhibit variations with oscillation amplitude that have a well defined trend: reacting body B's added mass increases slightly with oscillation amplitude. It is clear that, the damper plate feature on reacting body B provides a large added mass effect—an order of magnitude larger than reacting body A—as it pushes and pulls a very large fluid volume during motion. Second, the added mass results from experiments are reasonably well predicted by the BEM analysis because fluid inertial forces are generally well represented by fluid potential approach within the BEM code. Lastly, the variations in added mass with oscillation amplitude for reacting body B are primarily due to the natural variation of added mass with oscillation amplitude (*i.e.* $A_{22} = f(KC)$); whereas the variations in added mass with oscillation amplitude for reacting body A are primarily due to the limitation of the numerical method discussed in Section 2.3.2.

Diffraction Tests

The experimental and BEM derived excitation forces, also known as diffraction forces, for reacting bodies A and B, and the float, are summarized by the frequency dependent magnitude and phase plots shown in Figures 2.6 through 2.8. The results are shown for tests across a range of wave heights (*i.e.* 2cm, 4cm, 6cm, 8cm). The plotted lines indicate the mean values and the error bounds indicate +/- one standard deviation from the analysis discussed in Section 2.3.2. Key observations to be made from Figures 2.6 through 2.8 are as follows. First, the experimental excitation force data agree well with the BEM calculated values. The experimental excitation force magnitude curves seen in Figures 2.6a and Figures 2.7a, as normalized by wave amplitude, are observed to collapse together and the error bounds are narrow throughout most of the frequency range. It is apparent therefore, that diffraction forces are well predicted by BEM analysis in most of the wave frequencies tested. However, the BEM and experimental results shown in Figures 2.7a and 2.8a between 3 and 4rad/s, differ by approximately 25%. This difference is likely due to transverse reflections[3]. This issue is dealt with by assessing results from the numerical dynamics model using both the experimental and BEM-derived excitation force coefficients (see Section 4.6).

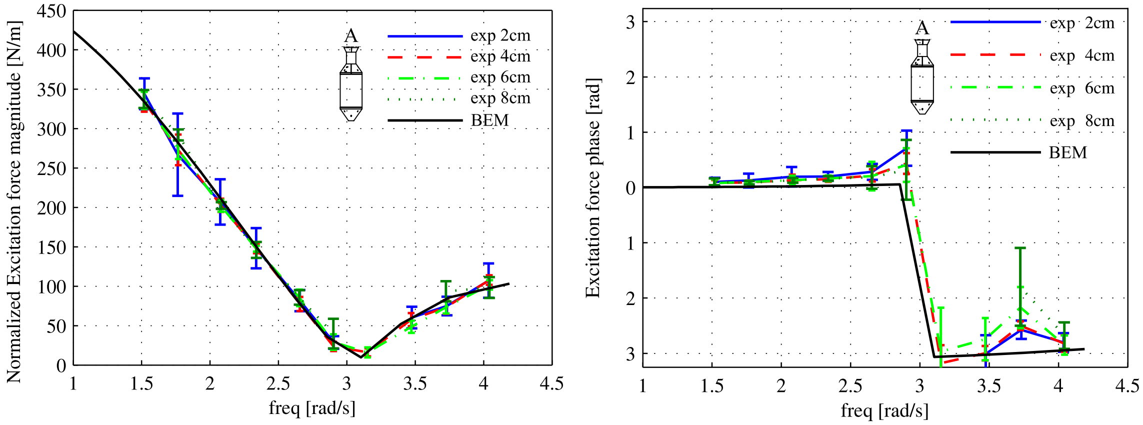

(a) Magnitude X_2/η.

(b) Phase ϕ_2.

Figure 2.6: Reacting body A experimental vs. BEM derived excitation force magnitude and phase.

2.4.2 Validation of Numerical Dynamics Model

The following sub-sections present, first, the rationale for input coefficient selection to the numerical dynamics model, and, second, an assessment of the validity of the numerical dynamics model for predicting power capture and dynamic motions of the WECs.

---

[3] An assessment of the tank standing wave resonant frequencies and evidence of transverse waves being present are given in Appendix F

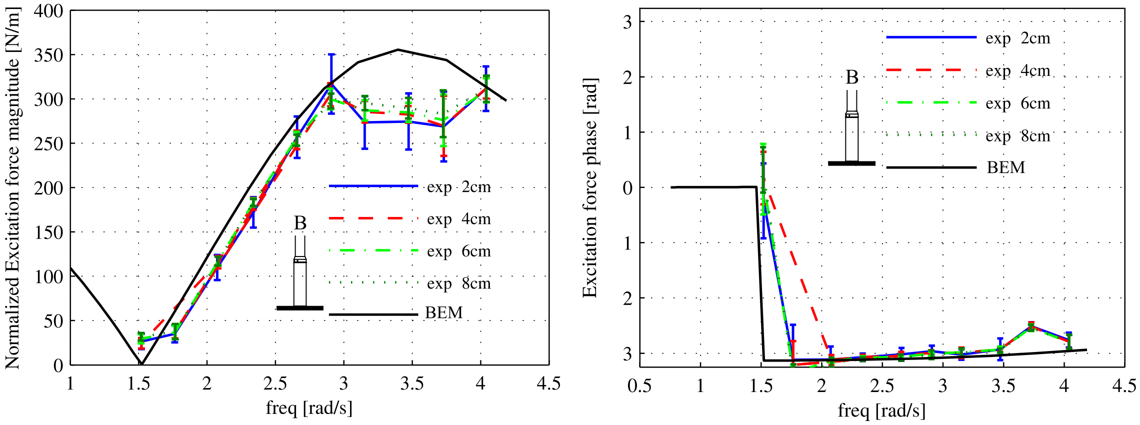

(a) Magnitude X_2/η.

(b) Phase ϕ_2.

Figure 2.7: Reacting body B experimental vs. BEM derived excitation force magnitude and phase.

Numerical Dynamics Model Inputs

Experimentally-derived heave damping and added mass values for the reacting bodies are used in the numerical dynamics model. The high damping levels attributed to viscous effects seen in Figures 2.4a and 2.4b, illustrate that the inclusion of viscous effects within the damping coefficients is critical to the validity of a numerical model.

BEM derived added mass and damping coefficients were used for the float. This choice was made for two reasons. First, radiation damping is expected to comprise a high proportion of the total float heave damping because it has a high water-plane area, thus a high displaced water volume for a given heave displacement. Second, experimentally derived added mass and damping coefficients are unavailable because the radiation tests were not capable of providing data for the float as discussed in Section 2.3.2.

BEM derived excitation force coefficients are used for the reacting bodies and the float because these coefficients are validated against experimental measurements, as shown in Figures 2.6a through 2.8b. A sensitivity study is conducted to assess the significance of disagreements in the 3-4rad/s range (see Section 4.6).

Because the numerical dynamics model is a linear model, it does not account for the amplitude dependence of the damping coefficients seen in Figures 2.4a to 2.4b. Therefore, the frequency dependent mean curve of the total damping coefficients over all oscillation amplitudes was taken. Where there are missing damping and added mass coefficient data, as shown in Figures 2.4b and 2.5b, a linear interpolation was

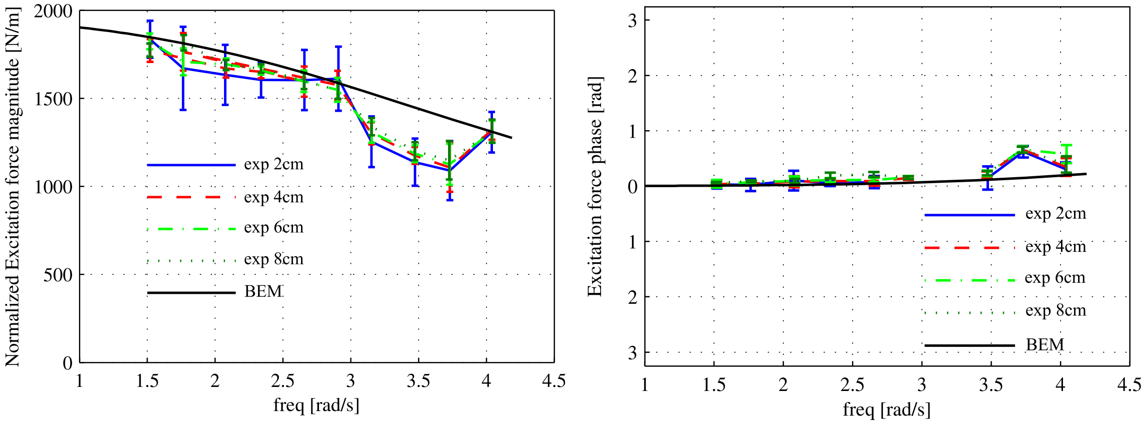

(a) Magnitude X_1/η.

(b) Phase ϕ_1.

Figure 2.8: Float experimental vs. BEM derived excitation force magnitude and phase.

used to estimate the missing data.

Response Amplitude Operators

Experimental and numerical magnitude and phase RAOs of reacting bodies A and B with zero PTO force are plotted in Figures 2.9a through 2.9d. As a strategy to avoid end-stop collisions during regular wave RAO tests, the wave amplitude was varied between tests. For RAO tests of reacting body A, 0.7cm $\leq \eta \leq$ 3.9cm and for reacting body B, 1.5cm $\leq \eta \leq$ 6cm.

Two numerically generated curves are shown on each of the RAO plots. The first is the numerical dynamics model result based on experimentally-derived reacting body added mass and total damping coefficients. The second is the numerical dynamics model result based on BEM-derived reacting body added mass and damping coefficients. As shown in Figures 2.9a through 2.9d, the natural frequency of reacting body A is approximately 2.0rad/s whereas the natural frequency of reacting body B is approximately 0.75rad/s. Reacting body A behaves as a 'wave follower' at frequencies below 1.5rad/s. At 1.5rad/s, the resonance condition is approached and large motion amplitudes are observed. Reacting body B exhibits much lower motion amplitudes below 1.5rad/s and approximately zero amplitude response above 1.5rad/s. The phase plots, shown in Figures 2.9c and 2.9d, show two distinct phase jumps. Observing each of the phase plots from low to high ω, the first phase jump is due to resonance of each of the reacting bodies—a natural behavior of damped single DOF oscillators. Inspection of Figures 2.6b and 2.7b indicates that the second phase jump is due to the discontinuity in the excitation force phase for each reacting body.

The numerical dynamics model with BEM added mass and damping coefficients heavily over-predicts the heave response at resonance for both reacting bodies. Excellent agreement is seen between the heave responses from the experimental results and the numerical model with experimental reacting body added mass and total damping coefficients. The numerical model in this case slightly over-predicts the resonant peaks, as expected, due to the assumption of linearized viscous drag. In Summary,

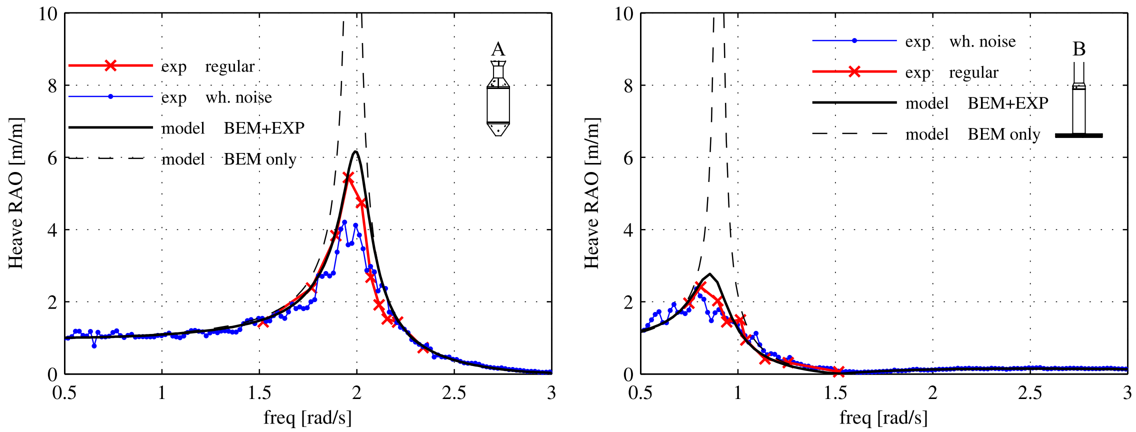

(a) Reacting body A magnitude.

(b) Reacting body B magnitude.

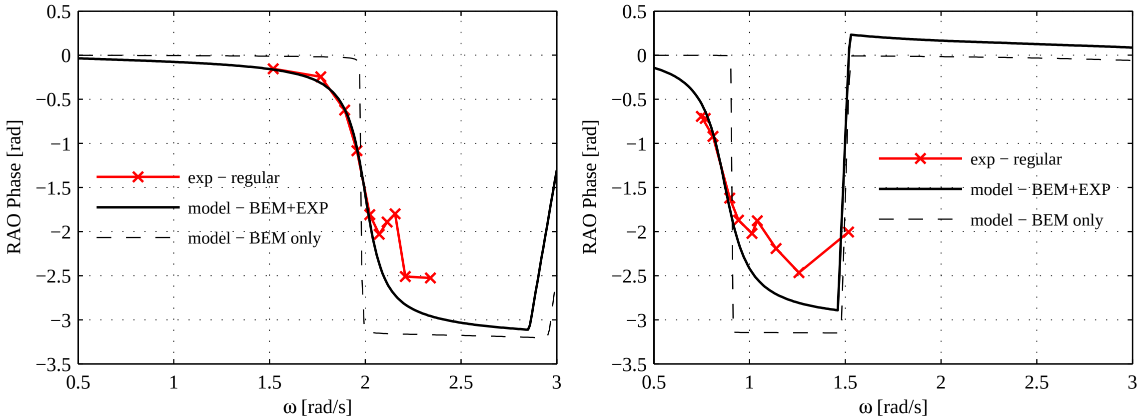

(c) Reacting body A phase.

(d) Reacting body B phase.

Figure 2.9: Heave RAO's for reacting bodies A and B. (a), (b) Response amplitudes from two experimental methods compared to two different numerical model results for reacting body A, B respectively. (c), (d) Response phases from one experimental method compared to two different numerical model results for reacting body A, B respectively. Two curves are shown for the numerical model when supplied with reacting body added mass and damping coefficients first from experiments (solid lines) and from BEM analyses (dashed lines).

the RAO results show that the numerical dynamics model, when supplied with experimentally derived added mass and total damping coefficients, is valid under free oscillation conditions. In the following sections, the numerical dynamics model data is compared with data from power producing WECs.

Power Capture

During power capture experiments in regular waves, the PTO damping was adjusted to separately optimized values across the frequency range for both WECs. Using hydrodynamic coefficients purely from *a priori* BEM analyses, the impedance matched passive PTO damping from Eq. (2.5) was applied. Figure 2.10a shows the *a priori* estimated optimal PTO damping coefficient, as applied in the experiments, along with optimal damping coefficient calculations from the numerical dynamics model with updated hydrodynamic parameters, herein referred to as *a posteriori* results.

Three observations can be made from Figure 2.10a. First, the optimal PTO damping for WECs A and B are, as expected, significantly different due to the different hydrodynamic properties of the reacting bodies. Second, comparing the peaks of the optimal PTO damping for WECs A and B, the PTO for WEC B provides 75% greater damping to maintain optimal passive damping control compared to the PTO for WEC A. Lastly, small differences are observed between the *a priori* PTO damping values and the *a posteriori* PTO damping curves shown in Figure 2.10a. These differences are due to the discrepancy in the output of Eq. (2.5) when supplied with *a priori* estimates to the WEC hydrodynamics from BEM analyses and the *a posteriori* knowledge of the WEC hydrodynamics from the experiments discussed in Section 3.4.1.

Frequency domain comparisons of wave power absorption are shown in Figure 2.10b for regular waves of heights, $2\eta = 4$cm, 6cm. Experimental mean power is based on Eq. (3.12) normalized by η^2. The curves labeled ‘model’ show the output of the numerical dynamics model supplied with the experimental PTO damping and mean frequency dependent curves of hydrodynamic parameters.

The sensitivity of the numerical dynamics model to the hydrodynamic parameters was assessed graphically by overlaying a shaded region that illustrates the upper and lower bounds of predictions based on upper and lower bounds of physical parameters to the numerical model. The upper and lower bounds of the shaded regions in Figure 2.10b are the envelope of the results from supplying the numerical dynamics model with all possible combinations of experimentally derived hydrodynamic coefficients.

For example, the lower bound of the shaded region in Power capture for WEC B in Figure 2.10b results from the numerical dynamics model when supplied with experimentally derived excitation forces (seen in Figures 2.7a and 2.8a featuring lower excitation force than predicted by BEM) and the highest valued experimentally derived total damping curve (seen in Figure 2.4b for $2|\hat{\xi}_2| = 8\text{cm}$).

The numerical results fit the experimental data quite well except for outliers in the experimental data at $\omega = 3.7\text{rad/s}$ in Figure 2.10b.

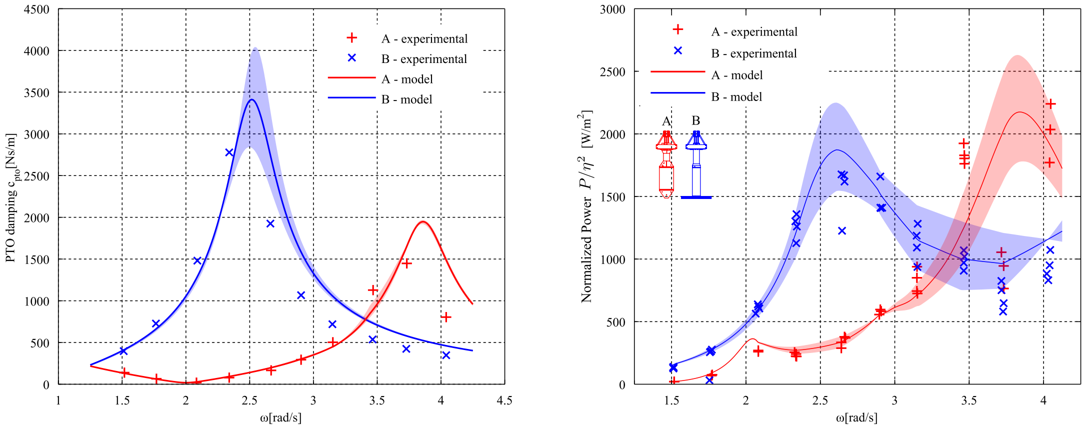

(a) PTO damping, c_{pto} **(b)** Normalized power, P/η^2.

Figure 2.10: (a) Experimental and numerical PTO damping. Data labeled experimental are the *a priori* estimated optimal PTO damping applied in experiments. Curves labeled model are the *a posteriori* calculated optimum damping. (b) Experimental and numerical mechanical power normalized by wave amplitude squared. The upper and lower bounds of the shaded regions are the envelope of the results from supplying the numerical dynamics model with all possible combinations of experimental and BEM-derived hydrodynamic coefficients.

The amplitudes of relative displacement between the float and reacting body during power capture tests in regular waves are plotted in Figure 2.11a. Three key observations of Figure 2.11a are made. First, the numerical dynamics model predicts the motion amplitude reasonably well for both WECs, with two exceptions: For WEC B, between 2.3 and 2.9rad/s, the amplitude is under-predicted and, for both WECS, the identified outlier at 3.7rad/s is evident though more pronounced for WEC A. Second, because the transparent regions are narrow, it is evident that relative displacement is less sensitive to perturbations in float excitation force, reacting body damping and added mass coefficients than power capture. Third, WEC A exhibits large relative oscillations at 2.1rad/s that provide little power capture, a result that will be discussed in Section 2.4.3. The amplitude and phase of absolute heave displacements for WECs A and B during power capture tests in regular waves of 4cm height are plotted in Figures 2.11c through 2.11f. The shaded regions representing the numerical dynamics model sensitivity to input parameters do not encapsulate all of the experimental data points. This indicates that sources of experimental variability other than the variability present among the hydrodynamic coefficients are present.

Observing the displacement and power absorption results for WEC A: Figures 2.10b, 2.11a, 2.11c, and 2.11e at frequency ω =3.7rad/s feature a distinctive and repeatable deviation from the model's predicted power capture and displacement amplitudes.

The outliers coincide an instability that arose in the PTO force feedback controller where high frequency oscillations in the float-reacting body relative displacement were physically observed during tests primarily at $\omega = 3.7$rad/s. Time series of the PTO force are shown in Figures 2.12a and 2.12b. The instability is clearly evident when comparing Figure 2.12b to Figure 2.12a which is typical of tests at all other wave frequencies.

To assess the overall contribution of the instability to the power absorption data, the high frequency noise caused by the instability was isolated by subtracting a filtered force time series from the raw force time series using a 124th order, finite impulse response, low-pass filter with 8rad/s cut-off frequency. For each wave frequency, the variance of the PTO force noise was taken as the indicator of the degree of noise due to the instability.

The variance of the PTO force noise signal as a function of frequency, shown in Figure 2.13, indicates clearly that the power capture tests for WEC A at $\omega = 3.7$rad/s are dominated by the unstable controller behaviour; thus, these points can be rejected as outliers whereas test data at $\omega \neq 3.7$ are essentially unaffected by the problem. The model vs. experiment discrepancy seen in Figures 2.10b to 2.11 at $\omega = 3.7$rad/s is due to the control instability observed in Figure 2.12b. The PTO control instability at $\omega = 3.7$rad/s approximately coincides with the expected and measured transverse standing waves discussed in Appendix F. It is likely that transverse standing waves induced unexpected force perturbations, thus causing difficulty for the PTO controller to maintain the desired force.

Based on Figures 2.10 and 2.11, the numerical model agrees well with experimental results in terms of absolute displacements, relative displacements, and power capture. The numerical dynamics model is, therefore, considered to be valid for the purposes of this study. In the following sections, the numerical dynamics model is used to investigate and compare practical design considerations for WECs A and B.

2.4.3 Numerical WEC Investigation

In this section, the validated numerical dynamics model is used (1) to analyze the behaviour of each WEC; (2) to investigate the engineering trade-offs associated with different PTO control schemes, and; (3) to shed light on the effect of motion constraints on each WEC. These analyses are constrained to the heave direction and regular waves.

Effect of reactive control

Figure 2.14 shows the modelled power absorption results for passive and reactive PTO's on both WECs A and B. The PTO mechanical impedances for passive and reactive control are set using Eqs. (2.5) and (2.6) respectively. Three key observations can be made from Figure 2.14. First, as expected, the reactive control PTO curves show greater power capture than passive damping PTO curves. Second, the peaks of each passive PTO curve intercept the reactive PTO curves at certain frequencies. For WEC A, the reactive and passive PTO curves meet at both 2.0rad/s and 3.8rad/s and for WEC B, the curves meet at approximately 2.6rad/s. Third, with a reactive PTO, WEC B's power curve nearly gains back all power capture advantage that WEC A's power curve shows at high wave frequencies.

The frequencies for which the peaks of each passive PTO curve intercept the reactive PTO curves occur where Eq. (2.6) collapses to the result of Eq. (2.5); *i.e.* when the optimal PTO impedance is a real number and passive damping PTO control is identical to reactive PTO control. Reactive control is shown to widen the power capture bandwidth of both WECs though WEC B seems to benefit more than WEC A. The effect of reactive control PTOs on the PTO force magnitude, relative displacement, and absolute displacement are shown in Figures 2.15a to 2.15d.

Observing Figure 2.15a, reactive control demands approximately 20-25% greater peak PTO force magnitudes than for passive PTOs on both WECs. Figure 2.15b shows that reactive control causes much higher float-reacting body relative motion amplitudes, especially for WEC A, in comparison to the passive damping control cases. Although, in wave frequencies above 3.5rad/s, where the peak performance of WEC A is observed for both passive and reactive PTO control, the relative motion of WEC A is low—less than that of WEC B. Figures 2.15c and 2.15d show that reactive control causes higher float and reacting body motion amplitudes. Exceptionally high reacting body displacement amplitudes shown in Figure 2.15d for WEC A are notable.

Along with the power capture improvements afforded by reactive control, exceptionally high displacements are induced compared to passive damping PTOs. From a structural design perspective, WEC A with a reactive control PTO exhibits critically high motion amplitudes whereas WEC B exhibits high, but manageable, motion amplitudes. It is likely for WEC A, that motions exhibited when operating with a reactive control PTO are mechanically feasible only for sea-states with small significant wave heights.

Effect of relative motion constraints

The effects of relative float-reacting body motion constraints on power capture are shown in Figure 2.16. Figures 2.16a and 2.16b show the numerical dynamics model's predicted power capture and relative displacement of the WECs with passive PTO control with the introduction of the relative displacement constraint from Eq. (2.8). Figures 2.16c and 2.16d show the effect of the displacement constraint on power capture and relative displacements with reactive PTO control.

The following conclusions can be drawn from the motion constraint analysis. Both WECs with passive PTO control are largely unaffected by the gradually increasing relative motion constraint. At first observation, WEC A's large relative motion amplitude at 2.0rad/s appears to contradict this claim. However, WEC A's large relative motion amplitude at 2.0rad/s enables only a small power capture improvement as shown by the shaving down of the small peak at 2.0rad/s in WEC A's power curve with the gradually increasing relative motion constraint. Thus, it would be advantageous to the mechanical design of WEC A to sacrifice the small power peak at 2.0rad/s in order to maintain low relative motion amplitudes. The effect of the motion constraint is negligible on WEC B's power capture under passive PTO control. The observations here illustrate that, within the limitations of heave constrained motions in regular waves, both WEC's relative displacements with passive damping PTO control are mechanically feasible.

In contrast to the motion constrained results with passive damping PTO control, Figures 2.16c and 2.16d show that power capture under reactive control is highly sensitive to relative displacement constraints. For WEC A, at frequencies below 3.7rad/s, where reactive PTO control enables power capture advantages over passive damping PTO control, the motion constraint strongly negates these advantages. For WEC B, at frequencies above 2.75rad/s, where reactive PTO control enables power capture advantages over passive damping PTO control, the motion constraints are not as restrictive as for WEC A because WEC B, when unconstrained, exhibits less relative motion than WEC A. That said, the two most restrictive motion constraint values investigated (*i.e.* $\epsilon = 1, 0.5$) are shown to strongly negate power capture. For both WECs. The curves of Figure 2.16c with the most restrictive motion constraint (*i.e.* $\epsilon = 0.5$) are nearly identical to the passive PTO control power curves in Figure 2.16a.

In summary, assuming passive damping PTO control both WECs are largely unaffected by motion constraints. However, when reactive control is assumed, WEC A is more sensitive to motion constraints than WEC B.

Performance Comparisons

Froude scaling was applied to the experimental and numerical power capture data, based on a geometric scale factor of α =25, to facilitate comparisons of the power capture results to theoretical upper bounds and representative sea conditions at full scale. WEC power capture with passive damping PTO and the two theoretical upper bounds are plotted in Figure 2.17a. The horizontal axis is wave period for ease of comparison the with results of Muliawan et al. [39] and Yu and Li [67] for WECs A and B respectively.

In Figure 2.17a, for regular waves with $T > 5$ sec, the WEC A power capture function follows closer to the theoretical upper bound, based on the radiation pattern for a point absorber (Eq. (2.9)), than the WEC B power capture function. However, a reactive control PTO would increase WEC B's power capture at low wave periods/high frequencies, as shown in Figure 2.14, to approach much closer to upper bound based on the radiation pattern of a point absorber. The theoretical upper bounds based on maximum utilization of the excitation force, given by Eq. (2.14), are also shown in Figure 2.17a for each WEC. The maximum full scale relative float-reacting body stroke assumed here for both WECs is $2|\hat{\xi}_r| = 2\epsilon$ =4 m. These bounds are different for each WEC due to the differences in the WECs' excitation forces and mechanical impedances.

The suitability of each WEC design for the North American West Coast wave climate can be assessed with reference to Figure 2.17b. Three distributions that characterize the Canadian Pacific wave energy resource are shown in Figure 2.17b for reference comparison to the power capture functions seen in Figure 2.17a. The resource distributions are (1) occurrence distribution of energy period; (2) the mean spectrum shape of the most frequently occurring sea-state; and (3) mean spectrum shape weighted by wave power transport. Details for calculation of the wave resource distributions are outlined in Appendix A. Observing the WEC power capture functions in relation to the resource distributions, WEC A features high power capture from short period seas and WEC B features higher performance in longer wave period seas; Thus, WEC A's power capture has most complementarity with the most frequently occurring seas, whereas WEC B's power capture has most complementarity with the power weighted most frequent seas.

Three caveats to these comparisons are: (1) The power capture functions are from regular waves analyses and the resource distributions are from irregular waves analyses. The performance of the WECs in irregular waves will need to be assessed to draw any definitive conclusions with respect to the resource; (2) An implementation of reactive PTO control could improve WEC B's performance in shorter period seas with non-extreme wave heights; And (3) since the WECs in this study were constrained to vertical motions, the effects of other modes of motion should be assessed to draw final conclusions on the comparison of WEC A to WEC B and the comparisons of both WECs performance to the wave resource.

2.5 Discussion

The most influential hydrodynamic parameter on the numerical dynamics model's validity is reacting body heave damping. The experimentally derived heave damping coefficients, containing both viscous and inviscid effects, are orders of magnitude larger than the BEM derived values which contain only inviscid (radiation) effects. Indeed, the heave RAO's for both reacting bodies were heavily over-predicted by the numerical dynamics model when inviscid (radiation) damping coefficients were used. Thus, it is critical to the numerical dynamics model validity that heave damping coefficients account for viscous effects.

Comparing both SRPAs performance and motion behaviors with optimum passive damping PTOs leads to a key point. WEC B maintains a fairly constant relative motion amplitude to wave amplitude ratio of $\sim$0.5 across the frequency range, whereas WEC A exhibits much higher relative displacement at lower frequencies. However, WEC A's high relative motion amplitude is associated with very little power production at the low frequencies—as proven by the displacement constrained results shown in Figure 2.16a. As a result, an implementation of motion constraints or a motion-limiting control system will be necessary for WEC A to avoid end-stop collisions but will not significantly impede WEC A's power capture function. In general, for similarly dimensioned SRPAs under passive damping PTO control: devices with streamlined reacting bodies produce more power at high frequencies and exhibit narrow-banded power functions. However, devices with heave damper plates on the reacting body produce more power at low frequencies and exhibit wide-banded power functions, mostly due to the vastly increased added mass afforded by the damper plate.

Reactive control vastly increases the power function bandwidth of both WECs A and B. To gain the bandwidth benefits associated with reactive control: WEC A's relative motion amplitudes become prohibitively large whereas WEC B's relative motion amplitudes are considered manageable from a design perspective. It follows that for similarly dimensioned SRPAs, the power production of devices with streamlined reacting bodies is more sensitive to any implementation of relative motion constraints compared to devices with heave damper plates on the reacting body.

2.6 Conclusions

A 1:25 scale, reconfigurable self-reacting WEC fitted with an adjustable PTO system has been developed and a comprehensive series of measurements has been conducted. A theoretical upper bound was identified for power conversion of two body WECs. The bound, established from the maximum utilization of the wave excitation force on a two body WEC, is an extension of Budal's upper bound for single body WECs.

Near-optimal PTO damping coefficients obtained from a heave motion constrained, linear, numerical dynamics model have been applied to the experimental WECs A and B. From the analyses of experimental data from WECs A and B constrained to vertical motions in non-extreme operating conditions, a numerical dynamics model that uses a combination of experimentally and numerically derived coefficients was validated for WECs A and B. The validated numerical model was used to investigate various considerations related to control and hydrodynamics of each WEC in regular waves. The following conclusions are made:

1. WEC A's reacting body has a much higher natural frequency than WEC B's reacting body, due to the combination of low buoyancy stiffness and high added mass of the damper plate of WEC B.
2. In terms of power capture with optimal-passive-damping PTOs, WEC A exhibits peak power capture at much higher frequency than WEC B's peak power capture mainly due to the very high added mass contribution of the damper plate on WEC B's reacting body.
3. Reactive control shows promise to significantly increase power capture for both WECs though the promise is greater for WEC B than for WEC A because its relative motion appears more manageable than WEC A's.

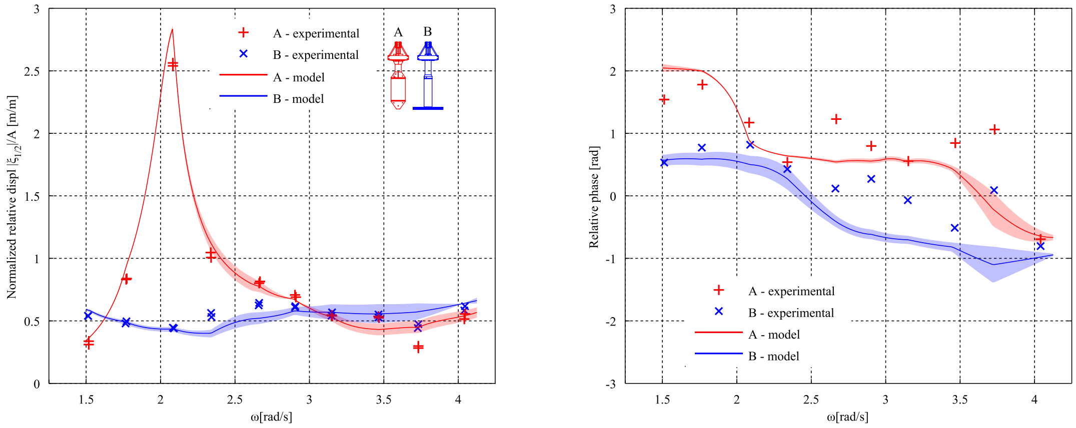

(a) Normalized relative displ.. **(b)** Relative phase.

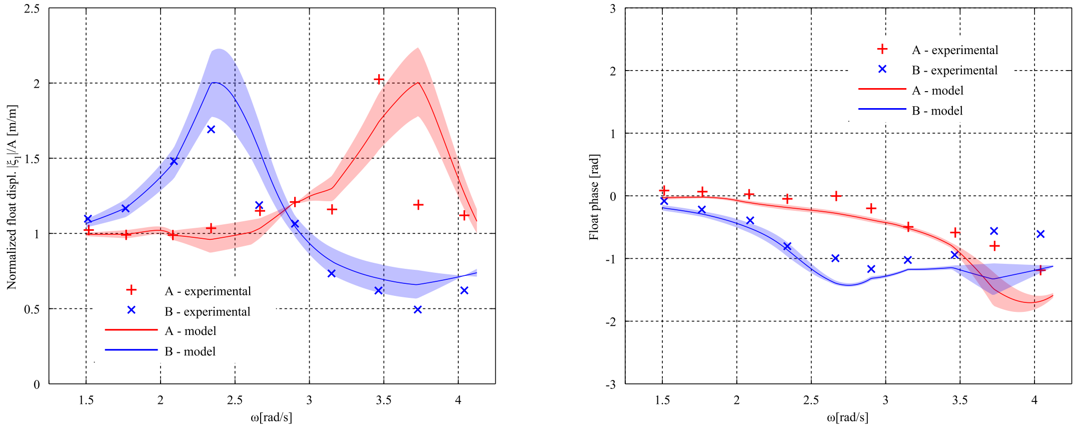

(c) Normalized float displ. **(d)** Float phase.

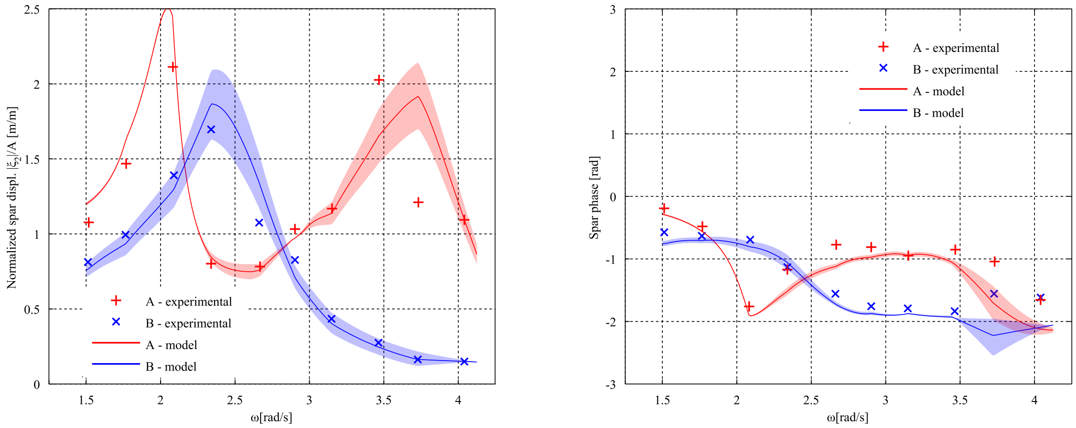

(e) Normalized reacting body displ. **(f)** Reacting body phase.

Figure 2.11: Normalized heave displacement amplitudes and phase for WECs A and B during power conversion tests with optimum passive damping PTO. Experimental results in $2\eta = 4$cm regular waves are shown with model results.

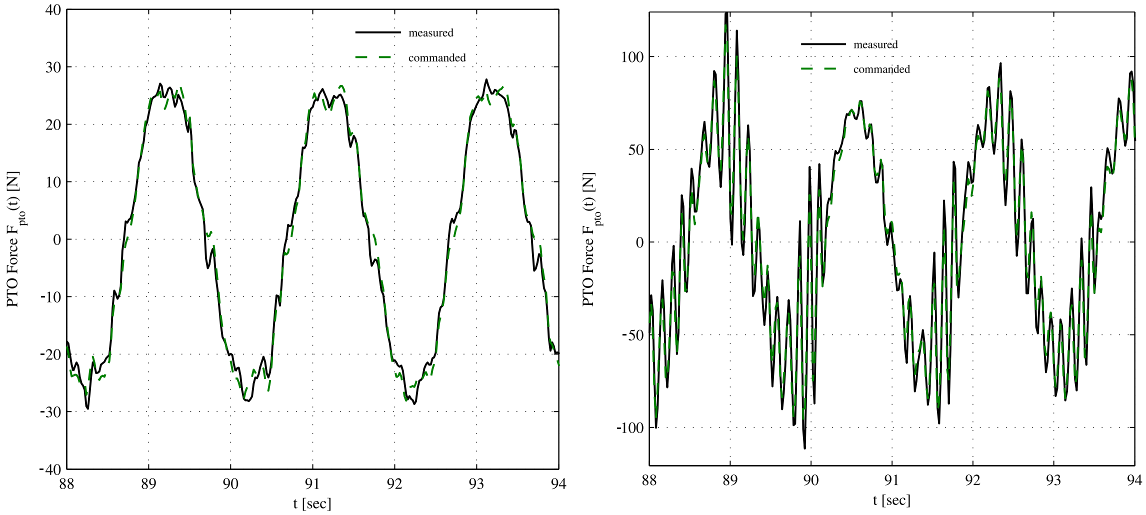

(a) $\omega = 3.2\text{rad/s}$ **(b)** $\omega = 3.7\text{rad/s}$

Figure 2.12: PTO force time series for WEC A in regular waves of (a) $\omega = 3.2\text{rad/s}$ (b) $\omega = 3.7\text{rad/s}$. The 'commanded' and 'measured' signals are the set-point force and the measured force output of the PTO respectively.

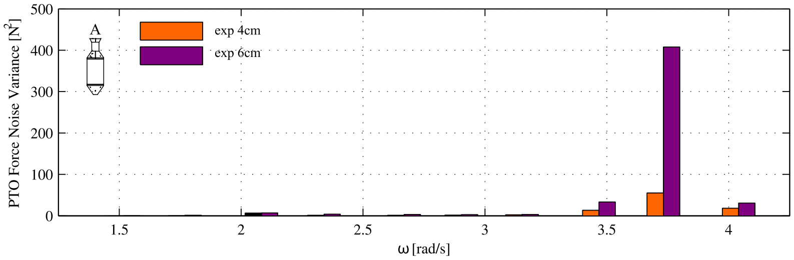

Figure 2.13: Variance of the PTO force noise, $Var(F_{raw} - F_{filt})$, as a function of frequency for 4cm and 6cm wave heights. F_{filt} corresponds to F_{raw} post-processed through a 124th order, low pass filter with 8rad/s cuttoff.

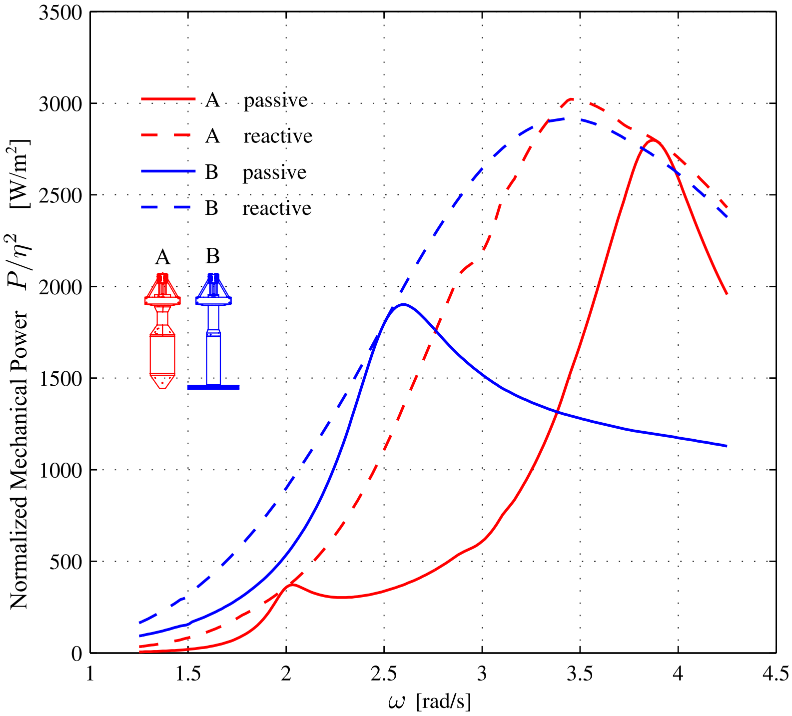

Figure 2.14: Normalized mechanical power output calculated by the numerical dynamics model for WECs A,B with both passive damping PTOs and reactive control PTOs.

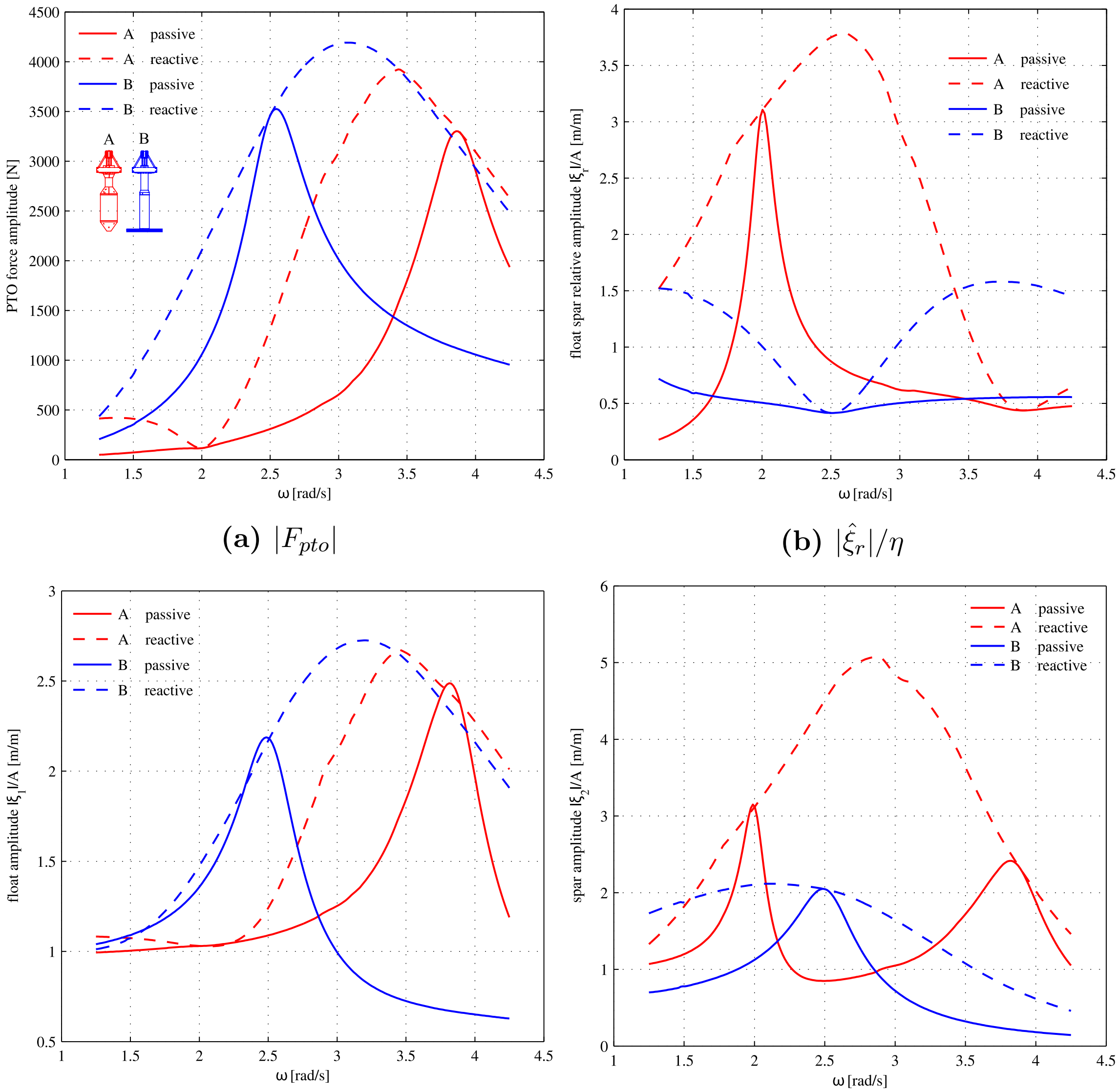

(a) $|F_{pto}|$

(b) $|\hat{\xi}_r|/\eta$

(c) $|\hat{\xi}_1|/\eta$

(d) $|\hat{\xi}_2|/\eta$

Figure 2.15: Frequency domain heave motion dynamics for WECs A and B with passive damping PTO and reactive controlled PTO (a) PTO Force magnitude, (b) Normalized relative displacement amplitude (c)Normalized float displacement amplitude (d) Normalized reacting body displacement amplitude.

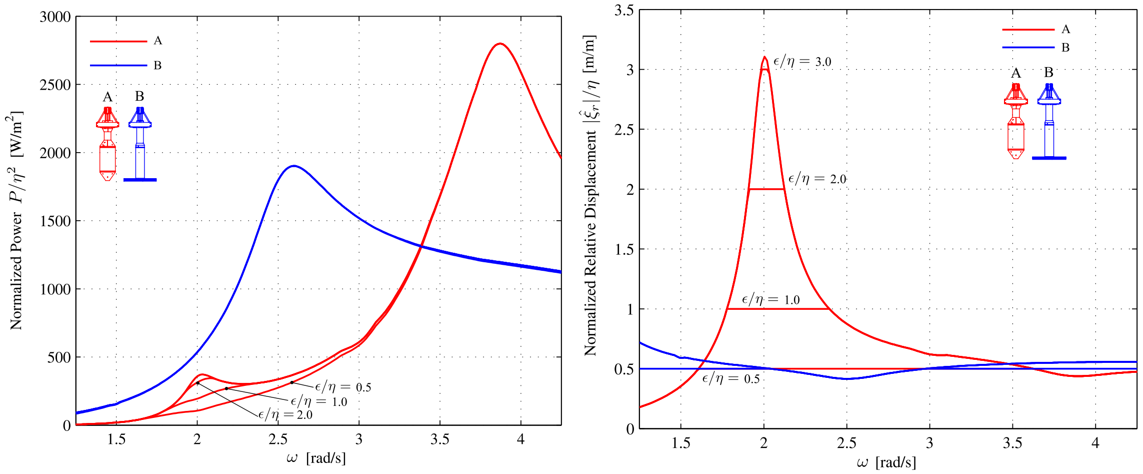

(a) P/η^2 (Passive PTO)

(b) $|\hat{\xi}_r|/\eta$, (Passive PTO)

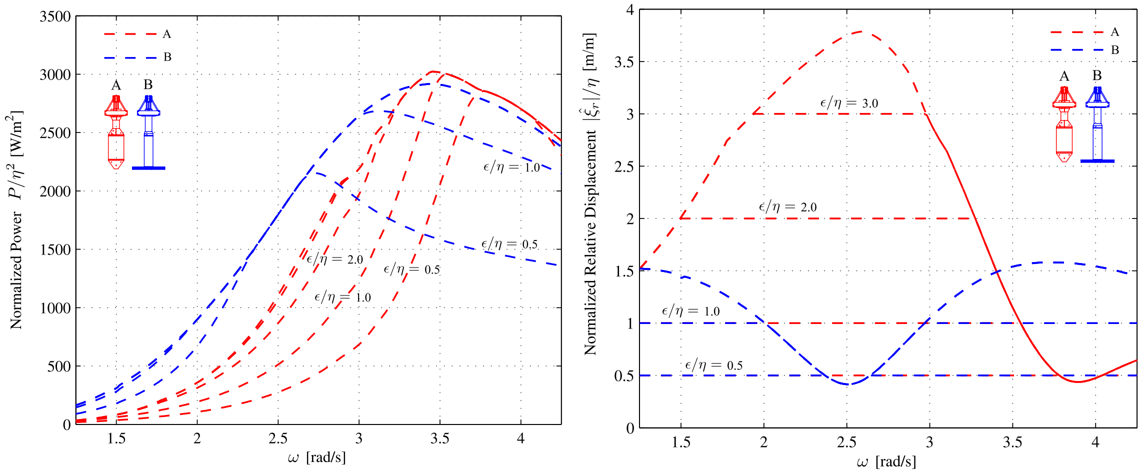

(c) P/η^2 (Reactive PTO)

(d) $|\hat{\xi}_r|/\eta$ (Reactive PTO)

Figure 2.16: The effect of relative displacement constraints on normalized power capture and relative displacement. The constraint is shown with various lines. The first lines are inactive constraint, then normalized constraint values $\epsilon/\eta = 3, 2, 1, 0.5$ are shown. The maximum allowable displacement amplitude, ϵ, is normalized by wave amplitude, η. (a) and (b) are results with passively damped PTO whereas (c) and (d) are results with reactive control PTOs.

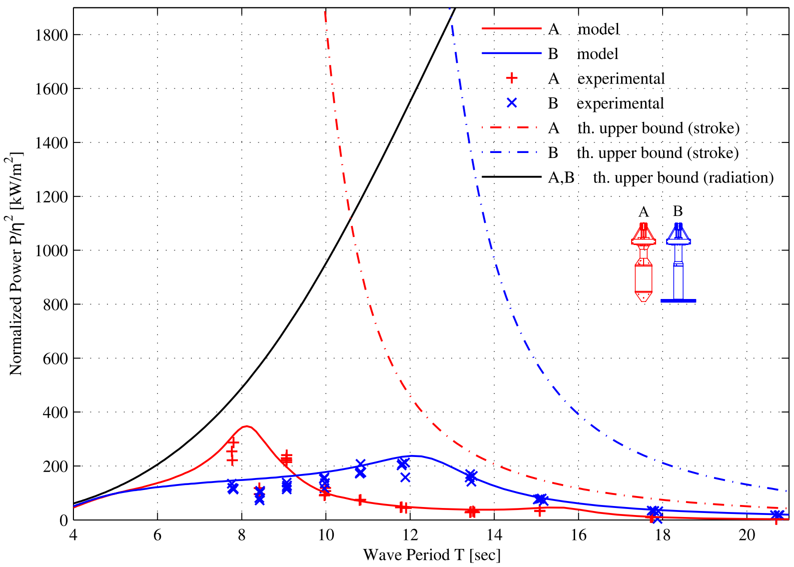

(a) Full scale power capture normalized by wave amplitude squared (model and experimental).

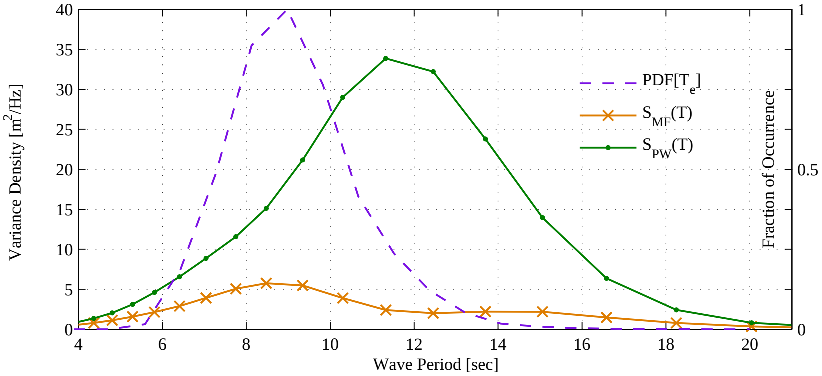

(b) Three resource distributions.

Figure 2.17: (a) Full scale power capture normalized by wave amplitude squared (model and experimental) as a function of wave period with upper bounds for power capture. (b) Distribution of energy period occurrence,PDF$[T_e]$, Mean spectrum shape of the most frequently occurring sea-states, $S_{MF}(T)$, Mean spectrum shape weighted by wave power transport J, $S_{PW}(T)$, from a 10 year data set at a grid point located near Hesquiaht Sound, on the Pacific coast of Canada.

Chapter 3

Experimental and numerical comparisons of self-reacting point absorber wave energy converters in irregular waves

3.1 Introduction

Self-reacting point absorbers (SRPAs) are wave energy converters (WECs) that convert energy from wave driven relative motion between two or more bodies into useful energy forms. SRPAs are axi-symmetric and are intended to operate primarily in the heave (vertical) direction. SRPAs typically employ a buoyant, surface piercing body referred to as the *float* which, driven by waves, reacts against a second surface piercing body referred to as the *reacting body*, to convert wave energy into mechanical energy which is extracted by means of a *power take-off* (PTO). Two design strategies are evident in current SRPA devices. The key difference between these strategies is the shape of the reacting body.

The two SRPA designs that are the focus of this study are shown in Figure 2.1. The first, denoted WEC A, is modeled after a WaveBob^{TM}(WaveBob Ltd., Ireland) device, featuring a positively buoyant float and a streamlined reacting body. The second, denoted WEC B, is modeled after a PowerBuoy®(Ocean Power Technologies Inc, USA). WEC B uses the same float as WEC A, but its reacting body has a smaller water-plane cross sectional area and features a large diameter heave plate.

The objective of this work is to systematically compare the power production of WEC A and WEC B, in irregular waves, given independently optimized PTOs . In this study, all motions are constrained to the heave direction in order to highlight the primary hydrodynamic effects that contribute to the WECs power performance.

3.2 Literature Review

Previous experimental and numerical studies of SRPAs focus predominantly on single device designs [22, 31, 32, 64, 25, 5, 13, 6, 26, 11, 66]. From these studies, it is difficult to draw equitable comparisons among different SRPA designs due to differences in mooring and PTO control strategies and insufficient characterization of experimental and numerical uncertainties. Only three comparative studies of WEC devices have been identified. Fifteen WECs of various classes were compared experimentally in terms of capture width and cost by Meyer et al. [38]. Eight WECs of different class and operating principle were compared by Previsic [50] at a high level based on performance data reported by device developers. Babarit et al. [2, 3] conducted numerical analyses comparing eight distinct WEC designs, including one Wavebob style SRPA—similar to WEC A in this study—based on mean energy production and key cost indicators. No detailed studies that compare the performance of alternative SRPA designs have been identified.

In an equitable (model scale) experimental and numerical power production comparison study of two SRPAs such as WEC A to WEC B, it is paramount that each WEC be assessed with individually optimized PTOs. Three key requirements follow: (1) the PTO simulator on the physical model must have sufficient resolution and repeatability for setting its impedance; (2) numerical models must sufficiently capture each WEC's heave motion dynamics; and (3) each WEC's hydrodynamics must be well characterized because the optimal PTO settings and numerical models for each WEC are highly dependent on knowledge of the complete suite of hydrodynamic parameters.

A handful of recent works are relevant to requirement (1): PTO simulation on the physical model. Two versions of an OPT Powerbuoy style SRPA—similar to WEC B of the current work—were previously developed and tested at 1:33 scale [34, 49, 40]. However, due to the inherent limitations of the passive mechanical PTO simulators on those models, the results were coarse and this ultimately limited the numerical model validation efforts [67]. Conversely, Villegas et al. [62] and Mackay et al. [36] describe large scale (1:20) experimental model SRPAs with advanced approaches to PTO simulation. The SRPA physical models in those studies use feedback controlled linear motors which, in concert with suitable instrumentation and control systems, provide for highly resolved and repeatable control over the PTO force behavior. Although the advanced PTO simulation strategies proved successful, neither of the studies state power conversion performance of the SRPA device in a comprehensive manner that facilitates comparison to other SRPA designs.

On WEC dynamics modelling, requirement (2): There exists well known dynamics modelling approaches, both in the frequency domain and time domain. However, frequency domain techniques should be avoided for modelling WECs in irregular waves [51]. The time domain approach by Cummins [10] is predominant for WEC dynamics modelling in irregular waves, although Taghipour et al [57] have investigated and presented viable alternatives. Recent literature presenting time domain models of SRPAs include studies by Babarit et al [2] and de Andres [11]. Babarit et al applied the Cummins approach to model heave, pitch, surge and relative motions of the float-reacting body in the absence of moorings. de Andres presents results from a heave motion constrained time domain model. Olaya et al [46] developed a heave constrained time domain model of an SRPA. Through a sensitivity study of viscous drag on the simulation results, Olaya states that viscous drag cannot be neglected; However no procedure is presented for specifying the viscous drag coefficient. For all three of these studies, experimental data validating the component hydrodynamic models is not available.

Finally, on literature relevant to requirement (3): hydrodynamic characterization, relevant studies have been published for both generic floating bodies and for specific SRPA designs. Inviscid analyses are routinely done with BEM software packages, but Olaya [45] presents a semi-analytical approach to obtain inviscid radiation/diffraction loads on an SRPA. Viscid loads, such as Morison drag, are often estimated from literature with high uncertainty; whereas, experimental characterization by means of free decay tests [8, 30] or forced oscillation tests [29, 1, 54] can improve the certainty of the estimation.

To facilitate a systematic comparison of WECs A and B with independently optimized PTOs in irregular waves, experimental tests of the physical model WECs with advanced PTO simulation will be undertaken. A time domain numerical model that contains coefficients extracted from experimental hydrodynamic characterization of the WECs will be developed. Experimental data gathered during a series of tests in operating conditions will be used to validate the time domain WEC model, and finally the time domain model will be used to assess each WECs production over a wider range of operational sea conditions.

3.3 Methods

3.3.1 Numerical Methods

Linear Hydrodynamics

The Boundary Element Method (BEM) code WAMIT [63] was used to obtain the inviscid hydrodynamic coefficients of WEC A and B—namely added mass, radiation damping, and excitation force. The panel meshes used in the analyses of WEC A and B are shown in Figure 3.1. The spatial domain is infinite in the horizontal dimensions and the water depth is 2.0m. A three-body analysis of each WEC configuration was performed of the float (body 1) and the reacting body (body 2) and body 3 was a numerical *moon-pool lid* introduced at the water surface in the annular gap between the float and reacting body. The moon pool lid mitigates erroneous BEM numerical solutions such as such as negative added mass and unrealistically high radiation damping in the fluid domain arising from resonant oscillations[1]. The moon pool lid is not considered in any further dynamic analyses of the current chapter. For each body j, the added mass, $A_j(\omega)$, radiation damping, $B_j(\omega)$ and complex excitation forces coefficient, $X_j(\omega)$, as a function of frequency are computed using the BEM analysis. Subsequently, the BEM derived added mass and excitation force coefficients in the frequency domain are converted to the time domain by establishing the kernel functions in Eqs. (3.1) and (3.2).

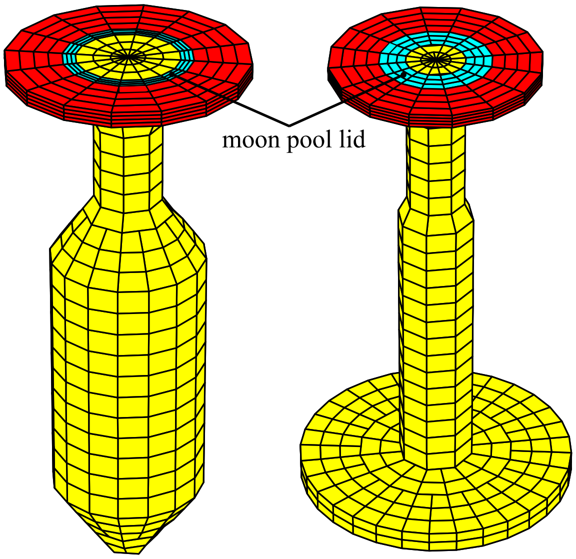

Figure 3.1: Panel meshes used for BEM analysis of the WECs. The float, reacting bodies, and moon-pool lids, are shown in red, yellow and light blue respectively. The moon pool lid is an infinitesimally thin mesh at the water-line.

$$k_{r,j}(t) = \frac{2}{\pi}\int_0^{\infty} B_j(\omega)cos(\omega t)d\omega \tag{3.1}$$

$$k_{e,j}(t) = \frac{1}{\pi}\int_{-\infty}^{\infty} X_j(\omega)e^{i\omega t}d\omega \tag{3.2}$$

Dynamics in the time domain

The equations governing the heave dynamics of the two-body WECs are given by Eq. (3.3). The inviscid effects described in Section 4.3.1 are complemented with addi-

---

[1] The moon pool lid is required here but not in Chapter 2 because an expanded frequency range is required here to accurately compute the kernel functions for the time domain model compared to the frequency domain model of Chapter 2.

tional forces of viscous drag, sliding friction, and the PTO force. Heave displacement, velocity, and acceleration of the float and reacting body are represented respectively by 2x1 vectors: $\vec{\xi}(t)$, $\dot{\vec{\xi}}(t)$, and $\ddot{\vec{\xi}}(t)$. $\boldsymbol{M} + \boldsymbol{A}(\infty)$ is a 2x2 mass matrix combined with the infinite frequency added mass. The remaining terms are 2x1 vectors, where $\boldsymbol{F}_e(t)$ are excitation forces, $\boldsymbol{F}_r(t)$ are radiation forces, $\boldsymbol{F}_c(t)$ are Coulomb friction forces, $\boldsymbol{F}_v(t)$ are viscous drag forces, $\boldsymbol{F}_k(t)$ are hydrostatic forces, and finally $\boldsymbol{F}_{pto}(t)$ are PTO forces.

$$(\boldsymbol{M} + \boldsymbol{A}(\infty))\ddot{\vec{\xi}}(t) = \Re(\boldsymbol{F}_e(t)) + \boldsymbol{F}_r(t) + \boldsymbol{F}_c(t) + \boldsymbol{F}_v(t) + \boldsymbol{F}_k(t) + \boldsymbol{F}_{pto}(t) \tag{3.3}$$

As per the Cummins approach [10], excitation forces are modelled by the convolution integrals seen in Eq. (3.4), where $\boldsymbol{k}_e = \begin{bmatrix} k_{e,1} & k_{e,2} \end{bmatrix}^T$. The radiation forces are modelled by the convolution integrals seen in Eq.(3.4). In the implementation, the input signals are discrete in time and the continuous integrals become sums with finite bounds. The radiation convolutions are evaluated from 0 to 10 seconds and the excitation convolutions are evaluated from -10 to 10 seconds. The convolution integral bounds are chosen to be wide enough so that kernel functions $k_{e,j}$ and $k_{r,j}$ have approached zero in the time ranges. Plots of the kernel functions in addition to the frequency dependent hydrodynamic coefficients are given in Appendix D.

$$\boldsymbol{F}_e(t) = \int_{-\infty}^{\infty} \boldsymbol{k}_e(\tau)\eta(t-\tau)d\tau \tag{3.4}$$

$$\boldsymbol{F}_r(t) = -\int_{-\infty}^{t} \begin{bmatrix} k_{r,1}(\tau)\dot{\xi}_1(t-\tau) \\ k_{r,2}(\tau)\dot{\xi}_2(t-\tau) \end{bmatrix} d\tau \tag{3.5}$$

A sliding friction force is included to account for the friction in the linear guide bearings on which the float and reacting bodies translate. The sliding friction force on body j is modelled using the Coulomb model with constant force $C_{c,j}$ as seen in Eq. (3.6).

$$\boldsymbol{F}_c(t) = -\begin{bmatrix} C_{c,1}\mathrm{sgn}(\dot{\xi}_1(t)) \\ C_{c,2}\mathrm{sgn}(\dot{\xi}_2(t)) \end{bmatrix} \tag{3.6}$$

The viscous drag force on body j is modelled by Eq. (3.7)— the relative velocity formulation of the Morison drag force [12]—where D_j is the characteristic diameter, $C_{D,j}$ is the drag coefficient, and $V_{f,j}(t)$ is taken as the fluid velocity at the depth location of the characteristic diameter. D_1 is taken as the float outer diameter, D_2 for WEC A is taken as the largest diameter of reacting body A, and D_2 for WEC B is taken as the diameter of the damper plate.

$$\boldsymbol{F}_v(t) = -\rho\frac{\pi}{8}\begin{bmatrix} D_1^2 C_{D,1}\left|\dot{\xi}_1(t) - V_{f,1}(t)\right|\left(\dot{\xi}_1(t) - V_{f,1}(t)\right) \\ D_2^2 C_{D,2}\left|\dot{\xi}_2(t) - V_{f,2}(t)\right|\left(\dot{\xi}_2(t) - V_{f,2}(t)\right) \end{bmatrix} \tag{3.7}$$

The hydrostatic forces are modelled by Eq. (3.8) where d_j is the diameter of body j at the waterline. The hydrostatic force is evaluated at the intersection of the mean-water-line and vertical centreline of the bodies.

$$\boldsymbol{F}_k(t) = -\rho g\frac{\pi}{4}\begin{bmatrix} d_{1\text{outer}}^2 - d_{1\text{inner}}^2 & 0 \\ 0 & d_2^2 \end{bmatrix}\vec{\xi}(t) \tag{3.8}$$

The PTO force is modelled by a passive PTO damping coefficient, c_{pto}, between the float ($j = 1$) and the reacting body ($j = 2$) as seen in Eq. (3.9).

$$\boldsymbol{F}_{pto}(t) = -\begin{bmatrix} c_{pto} & -c_{pto} \\ -c_{pto} & c_{pto} \end{bmatrix}\dot{\vec{\xi}}(t) \tag{3.9}$$

The selection of c_{pto} to maximize wave energy conversion in a given wave condition is discussed in the next section. A 4th order Runge-Kutta, fixed time-step, integrator with a time step of 0.065 seconds is used for the time simulations. The time domain model runs at approximately 10:1 real-time. No attempt is made to approximate the convolution integrals in the dynamics equations with a CPU time saving technique such as the State-space method [28, 68, 57].

Selection of PTO damping in Irregular Waves

The selection of the PTO damping coefficient, c_{pto}, that maximizes power capture in regular (monochromatic) waves can be obtained by mechanical impedance matching strategies for a two-body WEC as shown in Chapter 2. However, the analytical formula derived from impedance matching principles does not apply in irregular (panchromatic) waves. To overcome this, a numerical optimization of the c_{pto} value was completed for each wave spectrum considered. The optimization problem is as follows: Choose c_{pto} that maximize power capture, $\bar{P}$, given the variance density spectrum $S(\omega) = f(H_s, T_p)$ subject to $0 \leq c_{pto} \leq 3500$ Ns/m. The objective function is given by Eq. (3.10),

$$\bar{P}(c_{pto}) = c_{pto} \sum_{i=1}^{N} \omega_i^2 \left(\frac{\hat{\xi}(\omega_i, c_{pto})_{1/2}}{\eta} \right)^2 S(\omega_i) \Delta\omega \tag{3.10}$$

where the magnitude of the relative float-reacting body displacements, $\hat{\xi}(\omega_i)_{1/2}$, is computed by a frequency domain model with experimentally determined, linearized, viscous drag terms, as outlined in Chapter 2. Table 3.1 gives the selected c_{pto} values for each WEC with the targeted wave conditions. The Pierson-Moscowitz -spectrum is used for all wave conditions.

Table 3.1: Selected c_{pto} values and targeted wave conditions.

Name	H_s [m] [m]	T_p [sec] [sec]	c_{pto} A [Ns/m]	c_{pto} B [Ns/m]
IRR1	0.10	2.25	742	524
IRR3	0.10	1.80	959	772
IRR5	0.10	2.70	584	362
IRR8	0.06	2.25	742	524
IRR11	0.06	1.80	959	772
IRR14	0.06	2.70	584	362
IRR17	0.06	3.15	468	242
IRR20	0.10	2.90	305	305
IRR23	0.10	3.15	242	242
IRR25	0.06	2.35	483	483

3.3.2 Experimental Methods

Experimental Setup

The test facility (dimensions 58m x 4.57m x 2m depth) was Memorial University's Ocean Engineering Research Center located in St. John's Newfoundland, Canada. Chapter 2, Figure 2.3 shows the locations of the wave probes relative to the WECs and the heave motion constraint apparatus. Tests were conducted at geometric scaling factor 1:25. Detail on the rationale for tank choice, model specifications, and PTO simulator design are discussed in Chapter 2.

Decay Tests

Records of the displacement signals from the free oscillations of initially displaced bodies were used to extract Morison drag, C_{Dj}, and Coulomb friction, C_{Cj}, coefficients the reacting bodies of WEC A and WEC B. In data analysis, the coefficient extraction was done by solving an unconstrained optimization problem. The goal is to minimize the mean squared error between experimental and time domain model derived displacements given by Eq.(3.11) for time series displacement vectors of length N. The design variables are C_{Dj} and C_{Cj}. The optimization was carried out with the Nelder-Mead Simplex method [33] via Matlab's "fminsearch.m" function.

$$\epsilon_j(C_{Dj}, C_{Cj}) = \frac{1}{N}\sum_{i=1}^{N}\Big(\xi_{j,\mathrm{exp}}(t_i) - \xi_{j,\mathrm{mod}}(t_i, (C_{Dj}, C_{Cj}))\Big)^2 \tag{3.11}$$

Response Amplitude Operators

Response amplitude operator (RAO) tests without influence of the PTO were undertaken to separately assess the validity of the time domain model for each floating body in waves. The RAO is defined as the amplitude of the body's displacement, $|\hat{\xi}_j|$, normalized by the wave amplitude, η, as a function of frequency.

To validate the time domain model, the time domain model RAOs are compared to experimental RAO's. The experimental RAOs were obtained from from two methods. (1) Regular wave tests over a range of frequencies where $|\hat{\xi}_j(\omega)|/\eta$ was obtained from amplitudes of the monochromatic signals. (2) Irregular waves tests with white noise waves. (low pass filtered before input to wave maker). In this method, the RAO is derived from the ratio of Discrete Fourier Transforms of the heave response and wave probe signal.

Irregular wave selection

Analysis of a ten year set of hourly hind cast wave data, validated by wave measurements, from the West coast of BC, Canada [27] was used to select the sea-states applied in the physical model tests. A contour plot of the sea-state frequency of occurrence weighted by wave power transport for each record is shown in Figure 3.2.

The targeted region of conditions for the experimental tests are also shown in Figure 3.2. The conditions were chosen to cover as much of the power weighted

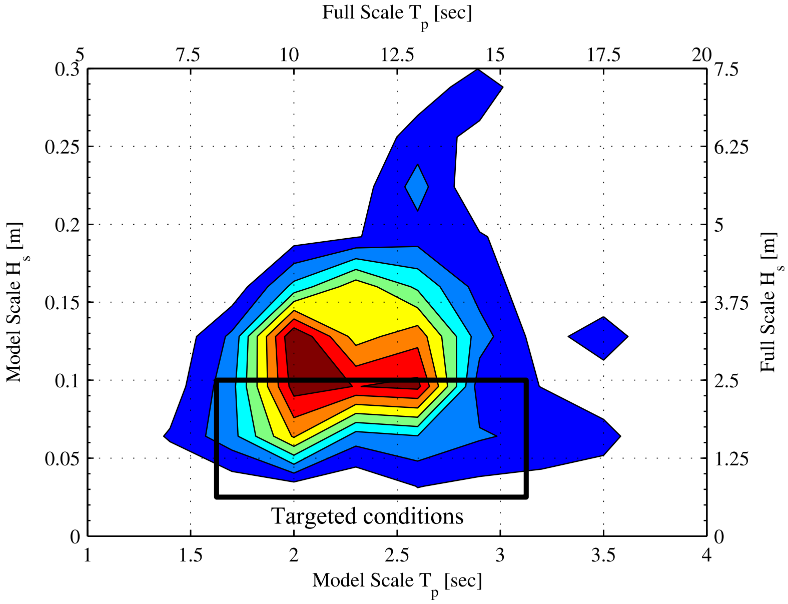

Figure 3.2: Frequency of occurrence contours weighted by wave power transport for a representative West coast BC location. Targeted conditions for experimental testing are within the rectangle shown. Model and full scale axes are given.

contours as possible while aiming to avoid end-stop collisions and wave over-topping during the model testing.

Power Capture

Tests of power capture for WECs A and B were done in 26 synthesized Pierson-Moscowitz spectra within the region indicated in Figure 3.2. The mean power capture for each test was calculated by Eq. (3.12), where $F_{pto}(t)$ is instantaneous PTO force signal and $U_r(t)$ is the instantaneous relative velocity signal.

$$P = \overline{P(t)} = \overline{F_{pto}(t)U_r(t)} \tag{3.12}$$

Capture width, a measure that quantifies the production capability of the WEC with respect to the available power in the wave conditions, is defined by Eq. (3.13),

$$\text{CW} = \frac{P}{J} \tag{3.13}$$

where J [W/m] is the wave power transport per unit crest width. Further, the capture width can be normalized by a characteristic dimension to form a metric given by

Eq. (3.14) known as capture width ratio,

$$\mathrm{CWR} = \frac{\mathrm{CW}}{L} \tag{3.14}$$

where the characteristic dimension, L in units of meters, can be developed in a number of ways for various WECs.

3.4 Results

3.4.1 Experimental Results

Decay Tests

The experimental and time domain model results for the freely decaying oscillations of the initially displaced reacting bodies are shown in Figure 3.3. Decaying oscillation test results were not available for the float. For each decay test, convergence of the optimization algorithm was achieved in approximately 60 iterations with objective function and design variable tolerances set to 10^{-6}. The model results shown in Figure 3.3 are from the time domain model with converged optimal Morison drag, C_D, and Coulomb friction, C_c coefficient pairings.

For reacting body A, three decay tests were analyzed with the resulting optimum coefficient pairs, $(C_{D2}, C_{c2}) = (2.3,\ 0.0081), (1.5,\ 0.011), (1.75,\ 0.010)$. Figure 3.3a shows the first of the three tests. For reacting body B, one decay test, as seen in Figure 3.3b, was analyzed with the resulting optimum pairing: $(C_{D2}, C_{c2}) = (2.8, 0.0051)$.

The fits between the experimental and numerical results with converged optimal C_{D2} and C_{c2}, as shown in Figure 3.3, are quite close. However, the spread of the results for reacting body B (C_{D2} = 1.5-2.3) showed further analysis was needed to select a single set of coefficients. To assess whether the converged values are meaningful, grids of the objective function (Eq. (3.11)) were directly computed in the solution regions defined in the parameter space $0 \leq C_{D2} \leq 6$, $0 \leq C_{c2} \leq 0.02\mathrm{N}$. Surfaces of the objective functions are shown in Figure 3.4.

In Figures 3.4a and 3.4b, the objective function surfaces are shown. The surfaces are flipped so that optima are viewed as maxima rather than minima to aid visual interpretation. Five contours around the solution surface optima (maxima) and the converged optima are shown.

Figures 3.4a and 3.4b show that the optimizations converged to the global opti-

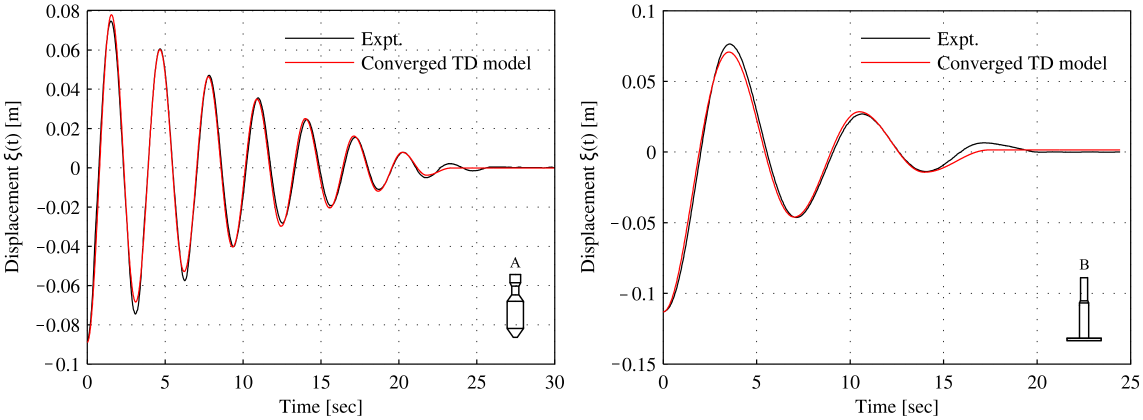

(a) Reacting body A free oscillation. **(b)** Reacting body B free oscillation.

Figure 3.3: Decaying free oscillations of the reacting bodies. Experimental displacement and the displacement from the numerical model output with converged optimal drag and Coulomb friction coefficients are shown.

mum of the objective function for both reacting body A and reacting body B. The results for reacting body A, seen in Figure 3.4a, show the gradient of the objective function is low in the solution region in comparison to the gradient in the outer regions of the (C_{D2}, C_{c2}) parameter space. However, the contours indicate the region is convex and smooth in the local area. The results for reacting body B, seen in Figure 3.4b, show the gradient of the objective function is also relatively low in the solution region in comparison to the outer regions; The contours indicate the region is convex; However, the jagged contours indicate the objective function is less smooth in the local area than the decay objective function for reacting body A.

The fits between the experimental and numerical decays shown in Figure 3.3 are extremely close. The optimization method for extracting Morison drag and Coulomb friction coefficients from decaying oscillation tests is shown to converge at the global optimal solution. However, due to the relatively low gradients of the objective functions in the solution region, the resolution and robustness of the method for extracting drag and friction could be improved with repetition of decay tests and subsequent application of the optimization method. Based on these analyses, the drag coefficients for reacting bodies A and B are taken as 1.9 and 2.8 respectively. The Coulomb friction coefficients for reacting bodies A and B are taken as 0.0051 N and 0.0097 N respectively. The float heave drag coefficient is taken as 1.0, consistent with Babarit et al. [3, 2]. Because the physical model of the float uses the same linear guides as the reacting bodies, the Coulomb friction of the float is taken as 0.0097 N.

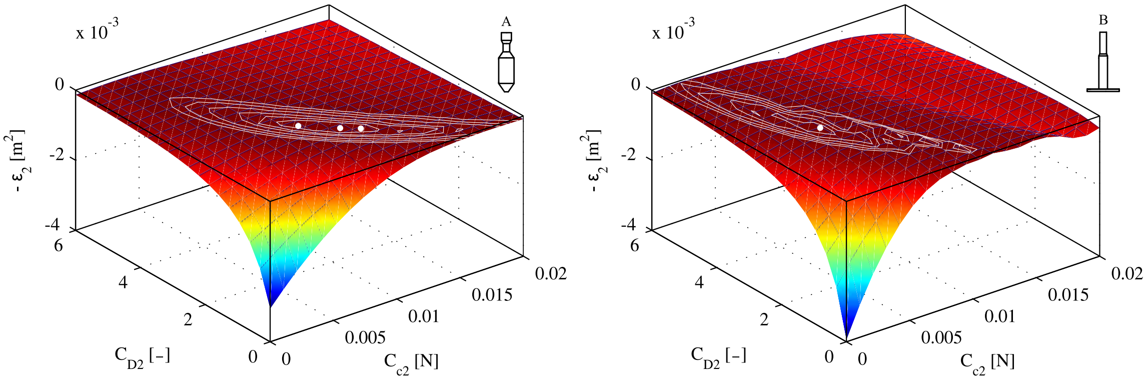

(a) Reacting Body A, $-\epsilon$.

(b) Reacting Body B, $-\epsilon$

Figure 3.4: Surfaces of mean squared error, $-\epsilon$ (shown here as a negative for easier viewing), between experimental displacement and numerical model displacement as a function of Morison drag and Coulomb friction coefficients. Contours of $-\epsilon$ are shown near the peak, and the converged optimal solutions are shown.

3.4.2 Validation of Time Domain Model

Response Amplitude Operators

Experimental and numerical RAOs of reacting bodies A and B with $F_{pto} = 0$ are plotted in Figures 3.5a and 3.5b. As a strategy to avoid end-stop collisions during regular wave RAO tests, the wave amplitude was varied between tests. For RAO tests of reacting body A, 0.7cm $\leq \eta \leq$ 3.9cm and for reacting body B, 1.5cm $\leq \eta \leq$ 6cm. The three numerically generated RAO curves are shown for each of reacting bodies A and B: each corresponds to a different wave amplitude.

As shown in Figures 3.5a and 3.5b, the natural frequency of reacting body A is approximately 2.0rad/s whereas the natural frequency of reacting body B is approximately 0.75rad/s. Reacting body A behaves as a 'wave follower' at frequencies below 1.5rad/s. At 1.5rad/s, the resonance condition is approached and heave displacement amplitudes on the order of 5η are observed. Reacting body B, due to high damping from the plate, exhibits much lower heave displacement amplitudes below 1.5rad/s and approximately zero amplitude response above 1.5rad/s.

Excellent agreement is seen between the experimental and time domain model heave RAOs. The RAO results show that the time domain model, when supplied with BEM derived radiation and diffraction kernels along with experimentally derived C_D and C_c, is valid in regular wave conditions with $c_{pto} = 0$. In the following sections, the time domain model data is tested against experimental data gathered during PTO

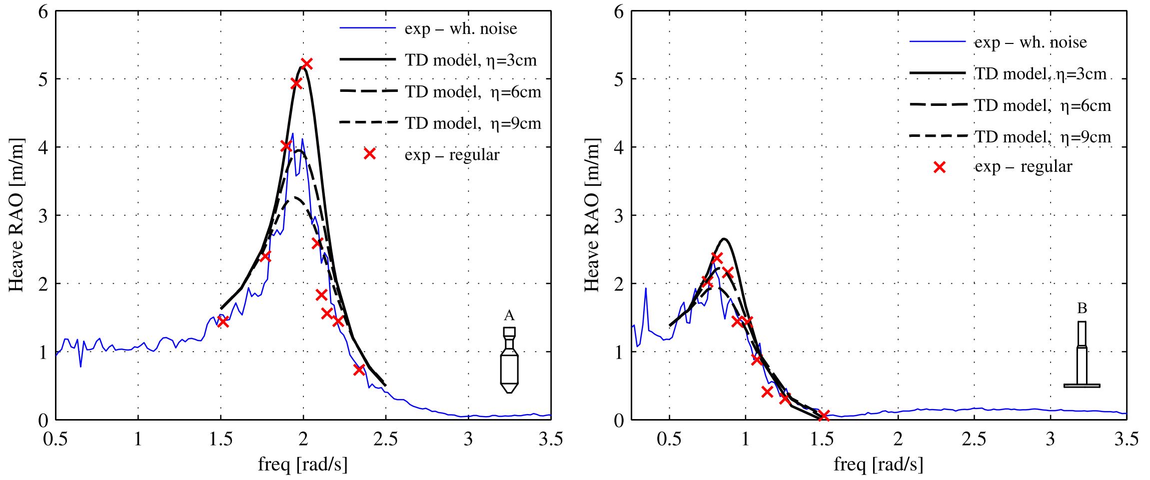

(a) Reacting body A. **(b)** Reacting body B.

Figure 3.5: Heave RAO's for reacting bodies A and B. (a), (b) Response amplitudes from two experimental methods compared to numerical model results for reacting body A, B respectively.

operation where $c_{pto} > 0$.

Power Capture

Data from example WEC power production tests along with time domain model results are given in Figures 3.6 and 3.7. The wave condition is a PM spectrum with H_s =0.073m, T_p =2.26sec denoted wave condition 3. Table 3.1 gives wave conditions and corresponding c_{pto} levels. The data plotted are water surface elevation, relative float-reacting body displacement, and mechanical power capture as a function of time. Figure 3.6 shows the time-series for the full test duration and Figure 3.7 shows the time-series for an 80sec portion. The wave probe signals in Figures 3.6a, 3.6b indicate maximum wave heights of ≈15cm. The zoomed wave probe plots in Figures 3.7a and 3.7b show that wave probes A and D produced very close but not identical water surface elevation signals with small differences more pronounced at peaks and troughs. The differences in the wave probe signals, though small, are likely due to a combination of tank wall effects and the inclusion of radiated waves from the WEC since the wave probe measurements were made *in situ*.

From the relative displacement time-series shown in Figures 3.6c, 3.6d, the time domain model output shows strong correlation to the experimental model results. Peaks and troughs in the experimental and modelled relative displacements align reasonably well temporally though indicate some time delay. Upon closer inspection via Figures 3.7c, 3.7d, it is evident some peaks and troughs are over/under predicted by the time domain model. The RMSE between the time domain model and experimental results over the test duration for both WECs is $\sim$ 5mm which amounts to $\sim$ 10% of the maximum relative displacements in the tests.

Figures 3.6e and 3.6f show the complete mechanical power time-series and Figures 3.7e and 3.7f show 80 second extracts. In these power time-series, the time domain model output is strongly correlated to the experimental model results. As wave groups arrive at the WEC, the time domain model clearly predicts the general power output behavior well, however, many of the power production peaks from the time domain model results are under/over predicted and/or delayed. The experimental mean power in wave condition 3 for WECs A and B is 0.73W, and 0.51W respectively. The time domain modelled mean power for WECs A and B is 1.1W, and 0.61W respectively.

To summarize the results from all sea-states tested, mean mechanical power from experimental tests and from the time domain model output for both WECs A and B are shown in Figure 3.8. The time domain model is shown to predict the mean mechanical power output very well for both WECs. The time domain model appears to have similar accuracy for predicting power production of WEC B in comparison to WEC A.

Summary plots of the RMS error between experimental and numerical relative heave displacement for both WECs A and B in all sea states tested are shown in Figure 3.9. The RMS error of relative displacement is generally higher for WEC B than for WEC A. Since viscous drag comprises a large proportion of the forces on reacting body B, the discrepancy in relative displacement is likely due to inaccuracy in the WEC B reacting body drag coefficient. Specifically, the inaccuracy in the drag coefficient can be attributed to three sources: (1) the drag coefficient was obtained from a single decay test rather then for an average of over three as done for WEC A; (2) due to the high drag of the damper plate, the decaying oscillations within that test were damped out much faster than for WEC B, thus reducing the data for which the fitting scheme was applied hence weakening the fit; (3) drag coefficients for oscillating flow are known to vary with frequency and amplitude of oscillation and the drag coefficient for reacting body B was extracted at the natural frequency of reacting body B— a low frequency compared to the wave frequencies applied during the power production tests.

The heave motion constrained time domain model is validated by Figure 3.8 for calculation of average power conversion of both of the WEC designs in irregular waves. However, the choice of sea conditions within the experimental test/validation exercises have not illuminated significant power conversion performance differences between the WEC designs. In the following section, the validated time domain model, is used to assess and compare the WEC A and B power production characteristics in a wider range of sea states.

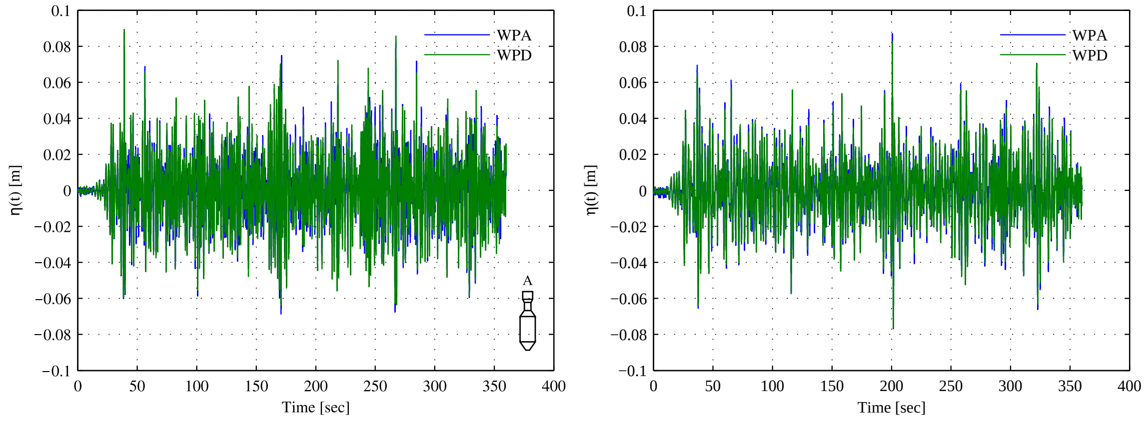

(a) WEC A (b) WEC B

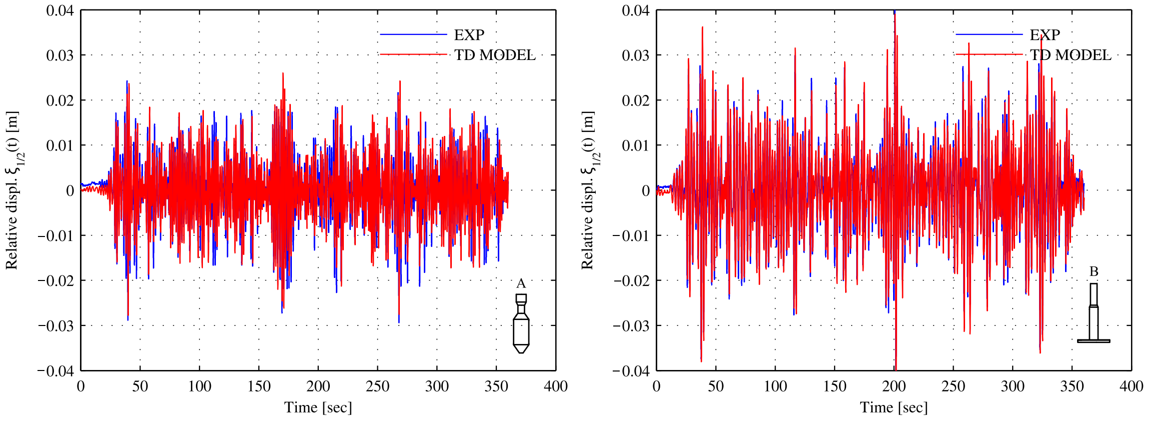

(c) WEC A (d) WEC B

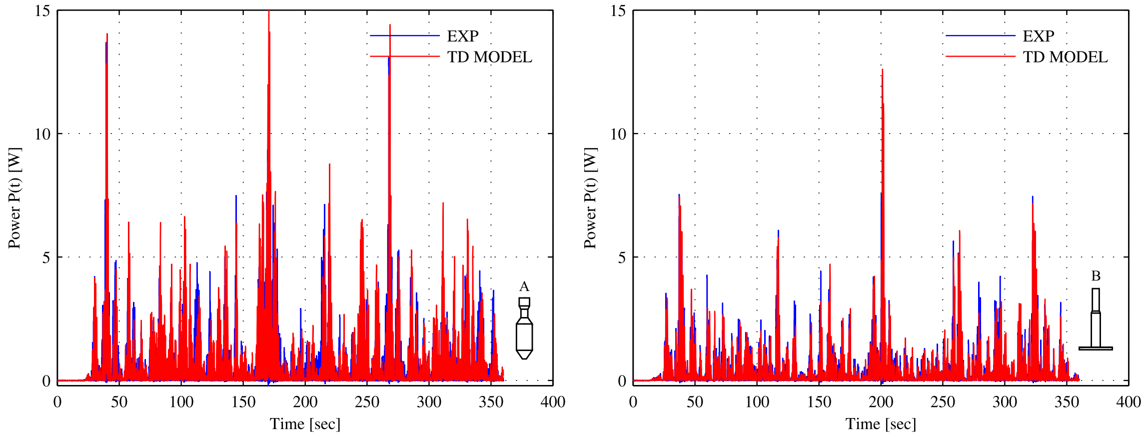

(e) WEC A (f) WEC B

Figure 3.6: Experimental surface elevation signals; Experimental vs. numerical relative displacement and mechanical power for both WECs A and B in sea state 3. Refer to Figure 2.3 for locations of wave probes A and D.

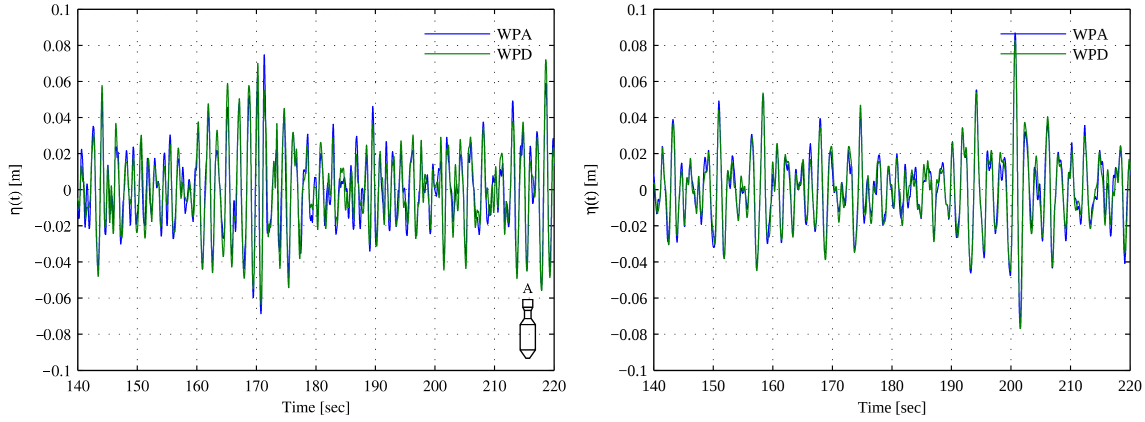

(a) WEC A

(b) WEC B

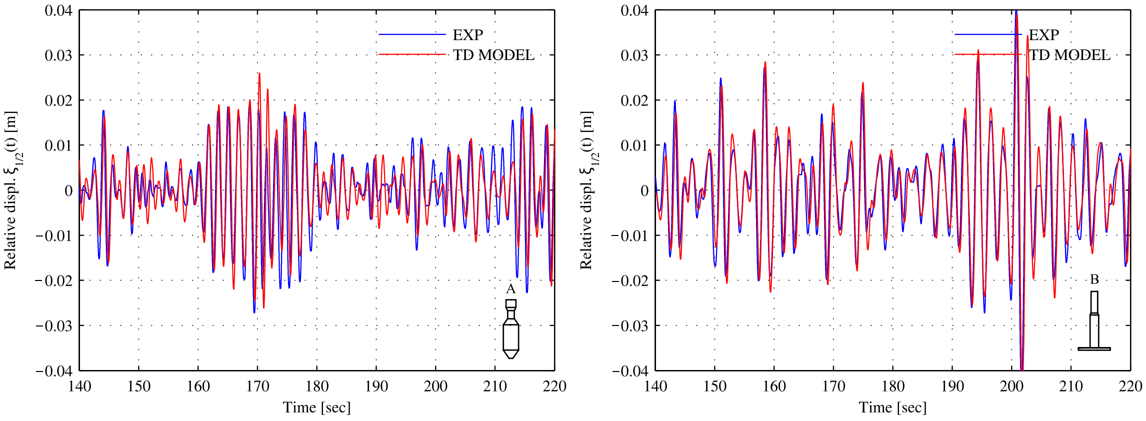

(c) WEC A

(d) WEC B

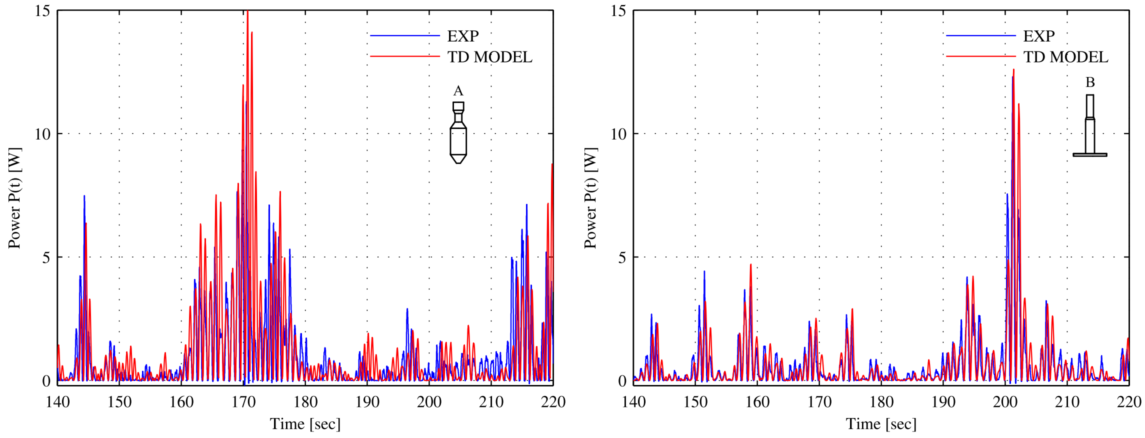

(e) WEC A

(f) WEC B

Figure 3.7: Experimental surface elevation signals; Experimental vs. numerical relative displacement and mechanical power for both WECs A and B in sea state 3. All signals zoomed to a relevant 80 second portion.

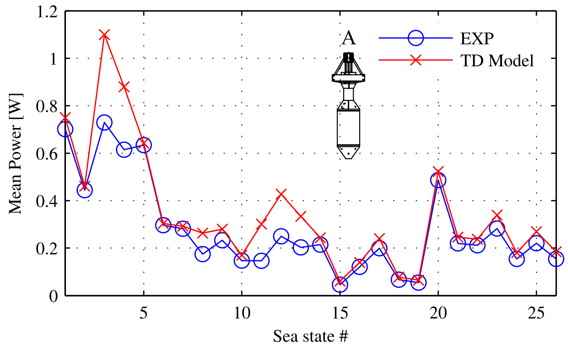

(a) WEC A

(b) WEC B

Figure 3.8: Experimental and numerical average mechanical power for both WECs A and B in all panchromatic sea states tested.

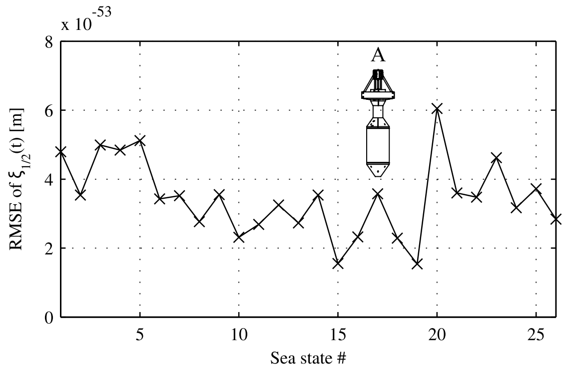

(a) WEC A

(b) WEC B

Figure 3.9: RMS error between experimental and numerical relative heave motion for the entire test duration in all sea states tested.

3.4.3 General Performance of WECs

To undertake a comparison of WEC A and B's power production levels in a wider range of wave conditions, the time domain model was run for each WEC over a grid of 144 total sea-states covering full scale H_s = 0.5-8.75m and T_p = 4-25sec. For each sea state, the optimum passive PTO damping was chosen using the methods discussed in Section 4.3.2. For each simulation, the water surface elevation was synthesized from a Pierson-Moscowitz spectrum using the uniformly distributed random phase model.

Contour plots of mean power production for each WEC as a function of H_s and T_p are shown in Figure 3.10. Contour plots of capture width are shown in Figure 3.11. Observing the power contours and capture width contours of Figures 3.10 and 3.11, WEC A's production reaches a higher peak value but WEC B shows a greater bandwidth of power production in comparison to WEC A. WEC B's power production and capture width are less sensitive to variation in the peak wave period, therefore WEC B is expected to capture more power from wider range of conditions. This confirms observations made about WEC B's bandwidth in comparison to WEC A's made in Chapter 2.

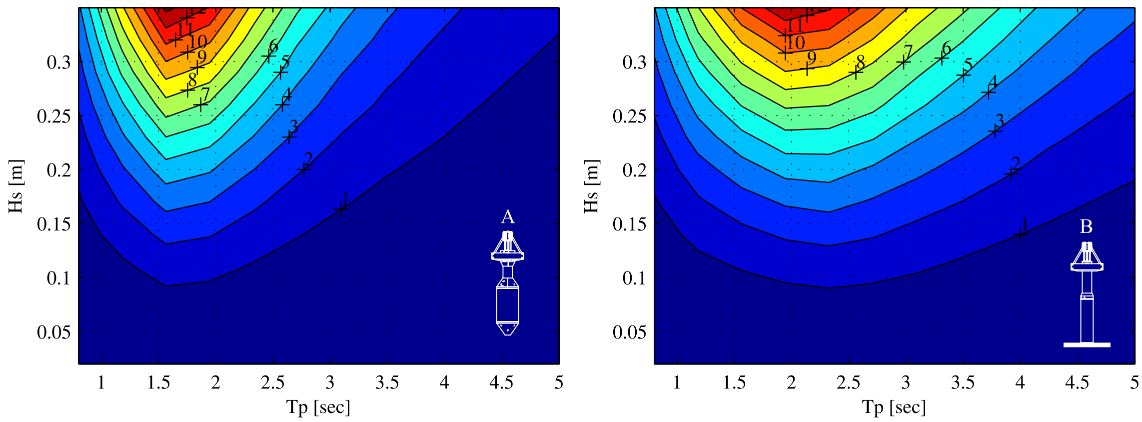

(a) WEC A power capture contours.

(b) WEC B power capture contours.

Figure 3.10: Mechanical power capture contours for both WECs. Contour labels units are Watts. Contours were taken from a 12x12 grid of power calculations (ie. a power matrix) for each WEC generated by the time domain model. The water surface elevations, duration $\sim$ 250sec (20 minutes full scale), were synthesized from Pierson-Moscowitz spectra.

For a representative location near Hesquiaht Sound off the West coast of BC, Canada, ten years of hourly parametric wave data [27] is used to assess the energy conversion performance of WEC A and WEC B. The mean wave power transport at the site is $\bar{J}$ = 29.5kW/m. The capture width contours given by Figure 3.11 for

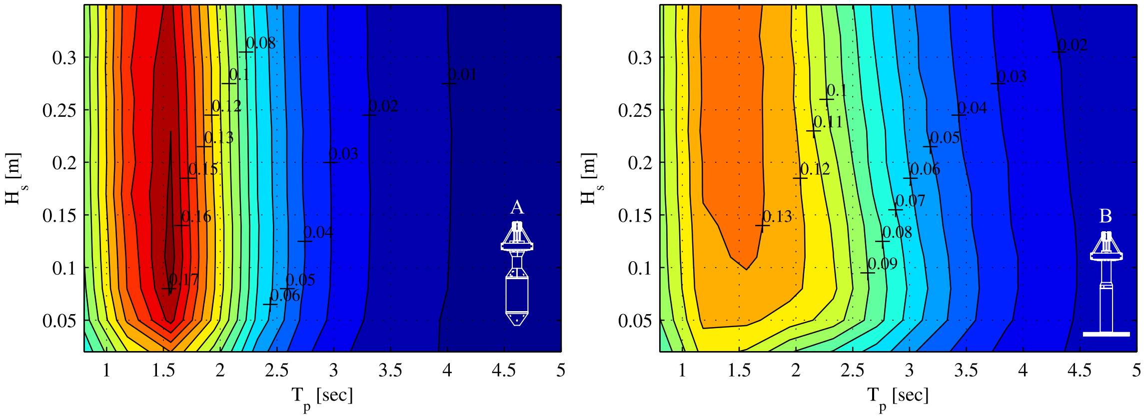

(a) WEC A capture width contours.

(b) WEC B capture width contours.

Figure 3.11: Capture width contours for both WECs. Contour labels units are meters. The CW surfaces were computed by Eq. (3.13) from a 12×12 grid of time domain model power calculations and the wave power transport in each sea state.

WEC A and B are Froude scaled by $\alpha = 25$ the interpolated and multiplied by the wave power transport for each hour in the wave data. The results are shown in Figure 3.12. Observing Figure 3.12, the power production of WEC B is often greater

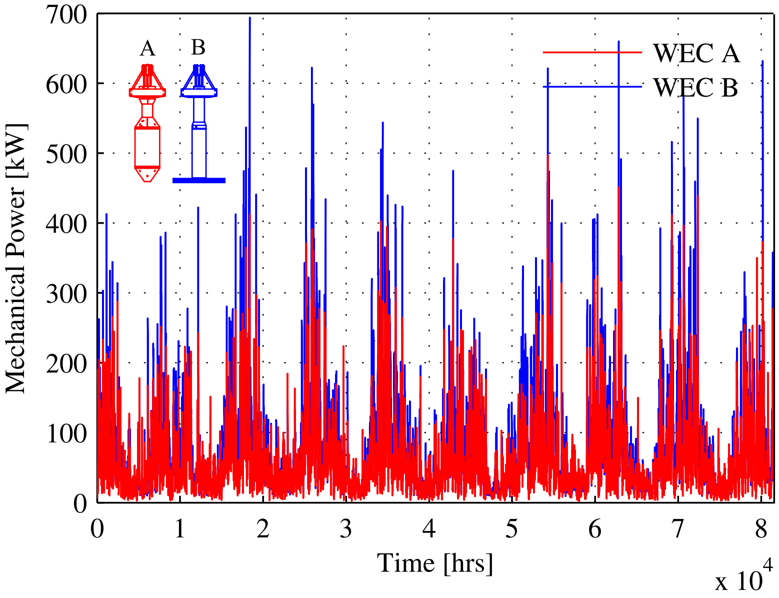

Figure 3.12: Average mechanical power converted over 9.3 years at 3 hour increments for a representative location off the West Coast, BC, Canada. The mean wave power transport at the site is $\bar{J} = 29.5$ kW/m.

than for WEC A in the West Coast Canada sea conditions. The data shows that

WEC B produces greater power output than WEC A for 62% of the data records. The average power output at the West Coast BC location for WEC A is 54.7kW, and for WEC B 78.5kW. The mean annual energy production (MAEP) for WEC A is 479 MWh, and for WEC B is 688 MWh. It can be concluded that the greater performance bandwidth of WEC B is driving its increased annual production compared to WEC A, and that WEC B, has a distinct economic advantage at the location studied.

3.4.4 Sensitivity of WEC Performance to Drag coefficients

Analysis of heave decay tests on the reacting bodies, discussed in Section 4.5.1, yielded a range of drag coefficients for WEC A reacting body and only a single test was available to determine the drag coefficient for the WEC B reacting body. Further, the float drag coefficient, is a value informed by the literature. A sensitivity study was done to gain insight into the uncertainty in the WEC performance associated with the drag coefficient assumptions. The power performance analysis at the West Coast BC location was re-executed for both WECS and for drag coefficient values of 50% and 150% of the experimentally calculated coefficient values. Results are summarized in Table 3.2. The sensitivity results in Table 3.2 show, for both WECs, that *increases* in each of the float and reacting body drag coefficients (while holding the other body's drag coefficient constant) by 50% causes reductions of approximately 10% in MAEP

Table 3.2: Sensitivity of WEC performance to viscous drag coefficients.

WEC A				
C_{D1} -	C_{D2} -	P [kW]	MAEP [MWh/yr]	%MAEP change
1.00	1.89	54.7	480	base
1.00	2.83	49.3	432	-10%
1.00	0.94	52.2	458	-5%
1.50	1.89	48.8	428	-11%
0.50	1.89	52.6	461	-4%
WEC B				
C_{D1} -	C_{D2} -	P kW	MAEP [MWh/yr]	%MAEP change
1.00	2.82	78.5	688	base
1.00	4.23	70.4	617	-10%
1.00	1.41	81.3	712	4%
1.50	2.82	73.1	641	-7%
0.50	2.82	76.3	669	-3%

over the 10 year data set. For WEC A, *reductions* of the float and reacting body drag coefficients by 50% also causes reductions in MEAP. These reductions may be explained by the lack of accounting for the perturbed viscous drag coefficients in the PTO damping optimization calculations discussed in Section 4.3.2; thus, leading to non-optimal c_{pto} levels for the perturbed cases within the sensitivity study. Similarly for WEC B, a 50% reduced float drag coefficient leads to a small reduction of MEAP. However, a 50% reduced reacting body drag coefficient leads to a small increase of MEAP. It is likely that the effects of non-optimality of c_{pto} as well as a reduction of energy dissipation into viscous drag are affecting the results. In summary, the sensitivity to drag results indicate the range of % change in MAEP is -11% to +4% for associated with changes in drag coefficients of ±50%

3.4.5 Alternative Performance Measures

There are other ways to summarize the efficiency of wave energy conversion devices. Capture width ratio, defined by Eq. (3.14), can be used. The mean capture widths for WEC A and B at the West Coast, BC location, are formulated into capture width ratios with the characteristic dimension, L, taken in three ways: as float diameter, square root of the wetted surface area, and cubed root of the submerged volume. The individual capture width ratios are denoted, CWR_D, CWR_A, and CWR_V respectively. Results are given in Table 3.3.

Table 3.3: Alternative WEC performance measures off West Coast, BC, Canada.

Parameter	WEC A	WEC B	Units
$\bar{P}$	54.7	78.5	kW
CW	1.86	2.66	m
CWR_D	0.126	0.180	-
CWR_A	0.0556	0.0692	-
CWR_V	0.149	0.240	-

The results in Table 3.3 indicate that WEC B has a greater efficiency of conversion from wave power to mechanical power on average at the West coast BC location regardless of the chosen capture width measure. However, because WEC A has a lower surface area than WEC B, WEC A is more competitive with WEC B in terms of CWR_A. Lastly, because WEC B has a much lower submerged volume than WEC A, WEC B's performance advantage based on CWR_V is amplified in comparison to WEC A's performance.

3.5 Conclusions

The following conclusions can be drawn:

1. Decay tests for drag coefficient selection can be used to extract Morison drag and Coulomb friction coefficients on floating bodies. A least squared error minimization scheme using a time domain simulation (that includes radiation forces) in the objective function is a reasonable solution to extract the coefficients for under-damped floating bodies.

2. The time domain model, as presented, is reasonably accurate in predicting the power capture of 1:25 scale experimental WECs with passively damped PTO, constrained to heave motion, in irregular waves. Although the experimental irregular wave conditions chosen did not provide for experimental comparisons of WEC A and WEC B power production, the time domain model provided for comparisons in a wider range of conditions.

3. Average power and capture width comparisons from the time domain model over an expanded range of wave conditions indicate WEC A has a greater peak production capability but WEC B has a wider banded production capability.

4. Comparisons of hourly power production over a year indicate that WEC A produces 54.7kW on average and WEC B 78.5kW at a representative location off the West Coast, BC, Canada.

Chapter 4

Experimental and numerical simulations of moored self-reacting point absorber wave energy converters

This chapter is based on the contents of the paper:
Beatty, S., Roy, A., Bubbar, K., Ortiz, J., Buckham, B., Wild, P., Stienke, D., Nicoll, R.,"Experimental and Numerical Simulations of Moored Self-Reacting Point Absorber Wave Energy Converters" *International Society for Offshore and Polar Engineering Conference*, Kona, USA, July 2015

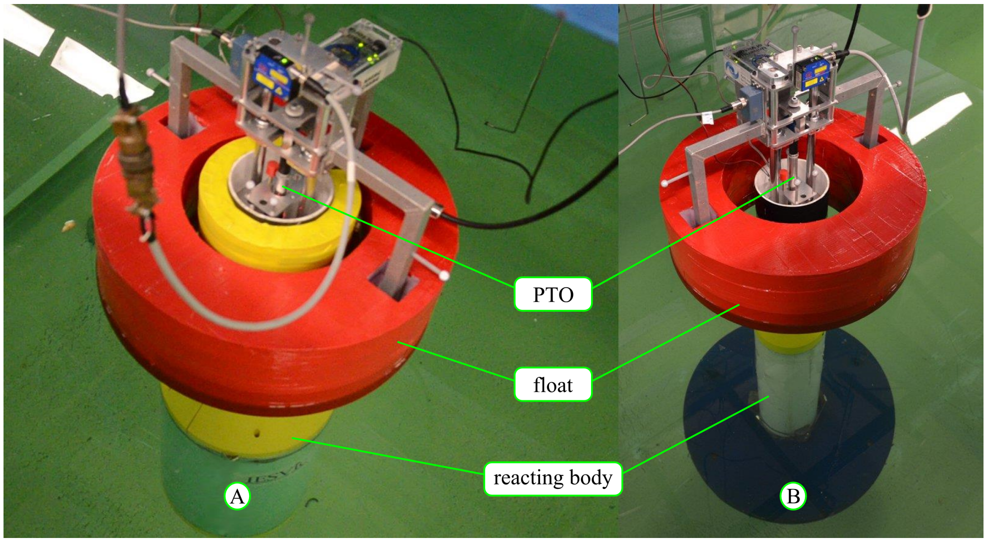

Figure 4.1: Images of the two WEC model configurations — WEC A (left) features a bulbous tank and WEC B (right) features a large heave plate. Both WECs have identical float shapes, drafts, PTOs, and instrumentation systems

4.1 Introduction

The objective of this chapter is to systematically compare the power production of WEC A and WEC B, given moorings and independently optimized PTOs. In this chapter, the WECs, shown in Figure 4.1, are moored with "soft" three legged horizontal moorings to highlight the natural behaviour and power capture performance of each WEC in the presence of dynamic motions in non-power producing degrees of freedom.

4.2 Literature Review

An assessment mooring arrangements, PTO settings, and end stops on the power production of a Wavebob style SRPA was done using 7 degree of freedom time domain simulations by Muliawan et al. [39]. That study however, does not have experimental validation, neglects viscous drag, and presents little on motions in non-power producing degrees of freedom. Tarrant and Meskell [59] also apply a 7 degree of freedom time simulation to study dynamics of the Wavebob WEC. However, their study focuses on the assessment of parametrically excited pitch and/or roll motions. The parametric excitation arises from the time variation of the pitch restoring coefficient [42]. Tarrant and Meskell [59] show the onset of resonant pitch and roll oscillations with an associated reduction of power production when the wave excitation frequency is twice the pitch/roll natural frequency of the WEC. The work of Villegas [62] is in agreement with Tarrant and Meskell [59], and further develops a notch filter in the PTO control system in an attempt to reduce the negative impact of the parametric oscillations.

Experimental tests and numerical simulations of the two SRPAs, moored, will be undertaken to facilitate a systematic comparison of the WECs power production and dynamic motions with independently optimized PTOs in regular waves. Experimental hydrodynamic and dynamic characterization of the WECs will be done in separate degrees of freedom; the resulting data will be used to select the coefficients required by the numerical simulation. A combination of the experimental and numerical results will be used to assess the effect of pitch and roll motion on power production. Lastly, the simulations will be used to assess an alternative strategy to the method proposed by Villegas [62] for reducing the negative impacts of resonant pitch oscillations.

4.3 Numerical Methods

4.3.1 Linear Hydrodynamics

The Boundary Element Method (BEM) code WAMIT [63] was used to obtain the inviscid hydrodynamic coefficients, namely added mass, radiation damping, and excitation force. The panel meshes used in the analyses of WEC A and B are shown in Figure 3.1. Details on the linear hydrodynamics including the calculation of the kernel functions used in the time domain simulations are given in Chapter 3, Section 3.3.1.

4.3.2 Dynamics in the time domain

The ocean engineering general dynamics solver ProteusDS [43, 56, 55] is employed to model and simulate the systems in the time domain. The float and reacting bodies are modelled using the articulated body algorithm (ABA) [20]. The first body is modelled as a floating 6DOF rigid body and the second body is constrained, via prismatic joint, to relative heave motion along the vertical axis of the first body. The PTO is modelled using a linear viscous damping, c_{pto}, applied in opposition to the relative heave velocity between the float and reacting body about the prismatic joint.

The BEM results are imported by ProteusDS to model the radiation and diffraction forces. The kernel functions given by Eq. (3.1), are used in the Cummins equation [10] to model the frequency dependent radiation forces in the time domain. Non-linear buoyancy and incident wave excitation forces are employed in the simulation. The Froude-Krylov force is calculated by integrating the undisturbed fluid pressure field over the surface of each body. This numerical integration is completed by discretizing the surfaces of each body into a polygonal mesh so that the force contributions from each polygon can be summed. This provides the ability to handle non-linear effects caused by large displacements or changes in submergence [44]. Viscous drag forces acting on the rigid bodies are computed using the same computational polygon mesh as the Froude-Krylov force model. The simulation uses the relative velocity formulation of Morison drag with constant independent drag coefficients in the surge, sway and heave directions.

Each arm of the three legged mooring system has three components: (1) a simply supported, single finite element cable attaches to the fair lead on the WEC reacting body; (2) an intermediate rigid body attached to the outboard end of the cable. The intermediate rigid body slides, via prismatic joint, about (3) an anchor rigid body that is held fixed in space. A spring stiffness, equal to the stiffness of the springs used in the experiments, is applied across each of the three anchor prismatic joints in the simulation.

4.3.3 Selection of PTO damping

The selection of the PTO damping coefficient, c_{pto}, that maximizes power capture in regular (monochromatic) waves can be obtained by mechanical impedance matching strategies for a two-body WEC [16]. The impedance matched c_{pto} for each WEC as a function of ω is chosen in this work using the heave motion constrained frequency domain numerical model of WECs A and B implemented and validated in Chapter 2. Table 4.1 shows the selected c_{pto} coefficients.

4.4 Experimental Methods

4.4.1 Experimental Setup

The test facility (dimensions 58m x 4.57m x 2m depth) was Memorial University's Ocean Engineering Research Center located in St. John's Newfoundland, Canada. Figure 4.2 shows the locations of the wave probes relative to the WECs and the

Table 4.1: Selected c_{pto} values for each test wave frequency. Wave heights were 4cm and 6cm for each frequency.

Name	ω [rad/s]	c_{pto} A [Ns/m]	c_{pto} B [Ns/m]
REG1	4.02	1555	470
REG2	3.71	1565	595
REG3	3.46	871	750
REG4	3.14	442	1091
REG5	2.89	295	1685
REG6	2.64	188	3087
REG7	2.32	89	2328
REG8	2.07	27	1206
REG9	1.76	64	638
REG10	1.51	134	397

mooring apparatus. Detail on the rationale for tank and model sizing and PTO simulator design are given in Chapter 2. Summary specifications of the moored physical models are given in Table 4.2. A Qualisys motion tracking system in a three camera configuration with passive markers was used to measure the WEC bodies position and rotation relative to a fixed global and local coordinate frames.

Table 4.2: Summary specifications of moored WEC models

Parameter	WEC A	WEC B	Units
Draft	1.4	1.4	m
Displacement	127	87.5	kg
Float outer diameter	0.59	0.59	m
Float hydrostatic stiffness	2000	2000	N/m
Reacting body hydrostatic stiffness	510	223	N/m
Mooring spring stiffness	42	42	N/m
Depth of mooring attachment point	0.56	0.76	m

The mooring system was designed to be soft; preventing drift while minimally affecting each WECs' free dynamic response to waves. The mooring lines are 2mm steel lines running 2m horizontally from the attachment point at the WEC reacting body to a self-aligning pulley. As shown in Figure 4.2, from the pulley, each of the three lines run vertically to a spring of 42 N/m stiffness which is connected to the fixed reference through a 10N capacity load cell. The mooring attachment points were located as near as possible to each WEC's centre of free pitch/roll rotation to provide minimal pitch/roll moments on the WEC in waves. The centres of free pitch/roll

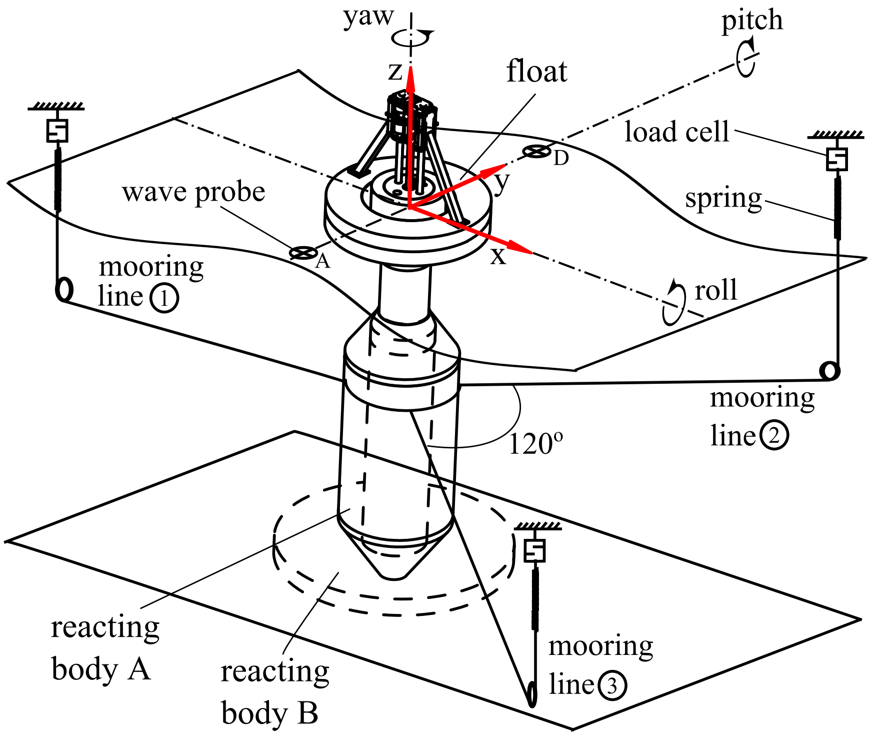

Figure 4.2: Experiment setup illustrating the moored WEC configurations. Waves travel in the $+x$ direction. Wave probes A and D are located at y =-1 m and y =1 m from the WEC center line. Tank width, depth, wave length, height are not to scale. Surge, sway, and heave motions are defined as displacements along $+x, +y, +z$ axes respectively.

rotation were located by analyzing motion capture data from free pitch decay tests.

In advance of work with WECs in the water, regular wave conditions spanning the selected frequency and amplitude ranges were characterized experimentally using three wave probes. The first wave probe was located at centre of the tank where the WEC is later mounted ($x = 0, y = 0$), the second located at $x = 0, y$ =-1 m, and the third located at $x = 0, y$ =1 m. The second and third wave probes are denoted A and D respectively in Figure 2.3. Data from the characterization is provided in Appendix F.

4.4.2 Decay Tests

Records of the motion capture signals from the free oscillations of initially displaced bodies with and without moorings attached were used to verify the dynamic and hydrodynamic coefficients with results from time simulations. To verify translational

Morison drag, C_{Dj} and mooring stiffness, decay tests on the moored WEC models were done in heave, surge, and sway directions. To obtain the pitch natural frequencies of each WEC, decay tests on un-moored WECs were done in the pitch direction.

4.4.3 Response Amplitude Operators

Response amplitude operator (RAO) tests without influence of the PTO were undertaken to separately assess the validity of the numerical simulation for each floating body in waves. The RAO is defined here as the amplitude of the body's displacement, $|\hat{\xi}_j|$, normalized by the wave amplitude, η, as a function of frequency. The simulated RAOs are compared to experimental RAO's. The experimental RAOs were obtained from regular wave tests over a range of frequencies where $|\hat{\xi}_j(\omega)|/\eta$ was obtained from amplitudes of the monochromatic signals.

4.4.4 Power Conversion

Tests of power capture for WECs A and B were done in 20 regular wave conditions. The mean mechanical power converted for each test was calculated by Eq. (3.12).

4.5 Parameter Identification Results

4.5.1 Decay Tests

Decay tests in pitch were used to calculate the pitch natural frequencies of each WEC without moorings using the average time between peaks of the pitch displacement decay data. The pitch and roll natural frequencies are ω_p =2.00rad/s for WEC A, and ω_p =1.44rad/s for WEC B.

The experimental and simulated results for the decaying oscillations in heave for WEC A and B, with the PTO connection "locked", are shown in Figures 4.3a and 4.3b respectively. The simulated locked heave decay data shown in Figures 4.3a and 4.3b correspond to heave drag coefficients of $C_{Dz1} = 2.5$ for the float, $C_{Dz2} = 2.0$ for reacting body A, and $C_{Dz2} = 3.5$ for reacting body B.

Three observations can be made of Figures 4.3a and 4.3b. First, the heave oscillations indicate locked heave natural frequencies for WEC A and WEC B as $\omega_{n33} = 3.8$rad/s and $\omega_{n33} = 2.6$rad/s respectively. Second, at $t > 7$ seconds, the WEC

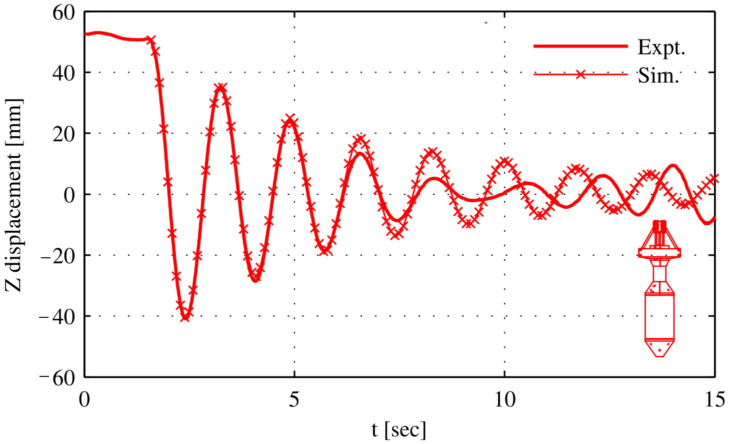

(a) WEC A.

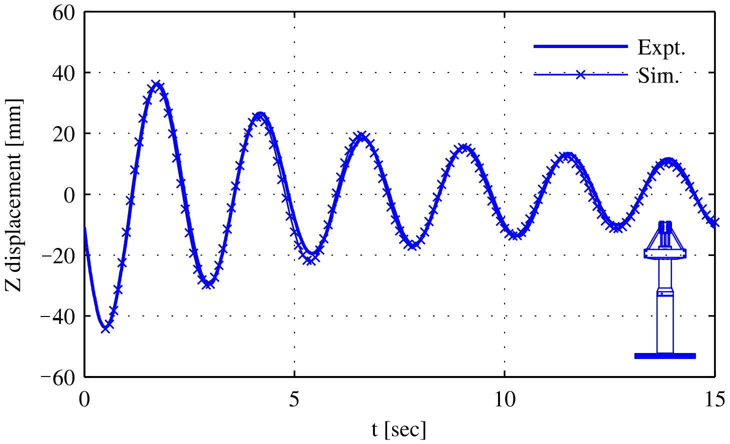

(b) WEC B.

Figure 4.3: Experimental vs. simulated heave decay results.

A experimental heave displacement is observed to change phase and increase in magnitude; thus diverging from the simulated displacement. Third, in Figure 4.3b, the simulation begins at the first displacement peak of the experimental data.

Despite WEC A having a greater total structural mass in comparison to WEC B, WEC B's locked heave natural frequency is much lower than WEC A's due a combination of lower total buoyancy stiffness and higher added mass than WEC A. The increasing response in the WEC A experimental and heave decay for $t > 7$ is due to the excitation of a standing wave mode across the width of the tank. Refer to Appendix F for a discussion of transverse standing wave resonant frequencies. Lastly, it is accepted here that the choice to set initial conditions of the simulation at the first displacement peak of the experimental data, shown in Figure 4.3b, introduces

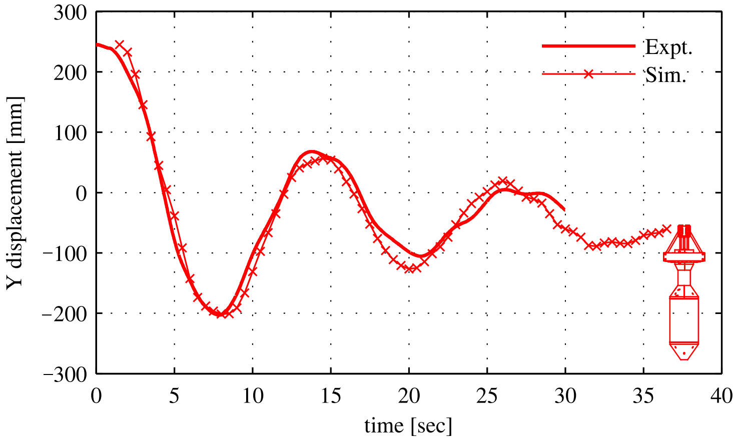

(a) WEC A.

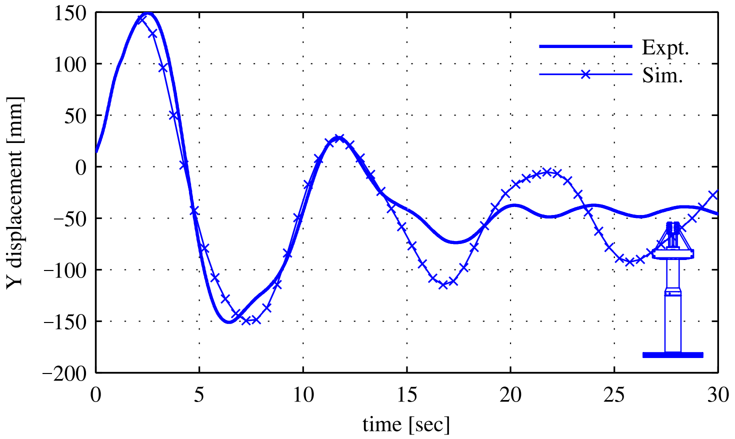

(b) WEC B.

Figure 4.4: Experimental and simulated sway decay results.

small error in the hydrodynamic force calculations due to the lack of accounting for the fluid memory effects of the WEC's previous motions.

Decaying oscillations in the sway direction for WEC A and B, with the PTO connection locked, are shown in Figures 4.4a and 4.4b respectively. The simulated sway decay data shown in Figures 4.4a and 4.4b correspond to surge and sway drag coefficients of $C_{Dx} = C_{Dy} = 1.0$ for the float, reacting body A, and for reacting body B. Since the moorings provide the sway stiffness, the sway decay oscillations provide key data in characterizing the moorings.

Observed from, Figures 4.4a and 4.4b, the sway natural frequencies of WEC A and WEC B are respectively $\omega_{n2} = 0.49$rad/s and $\omega_{n2} = 0.63$rad/s. The simulated decay oscillations show agreement with the experimental results except for the WEC

B displacements at $t > 15$ sec in Figure 4.4b. Figure 4.4b shows again that the simulation begins at the first displacement peak of the experimental data.

Since the mooring systems for both WEC A and WEC B have the same stiffness, the lower sway natural frequency of WEC A in comparison to WEC B is a result of WEC A's higher total mass. WEC A's structural mass is higher than WEC B's and, due to greater projected area in that degree of freedom, the sway added mass of WEC A is greater than that of WEC B. Lastly, the disagreement between the experimental and simulated WEC B displacements at $t > 15$ sec in Figure 4.4b are suspected to be due to the sensitivity of the WEC B damper plate drag characteristics to pitch and roll angle. A small change in pitch/roll angle will cause relatively large changes in the x/y direction projected area, and may exhibit vortex shedding phenomena that is not captured by the panelized Morison drag approximation in the simulation hydrodynamics. It is again accepted here that the choice to set initial conditions of the simulation at the first displacement peak of the experimental data, shown in Figure 4.4b, introduces small error in the hydrodynamic force calculations due to the lack of accounting for the fluid memory effects of the WEC's previous motions.

4.5.2 Response Amplitude Operators

Experimental and numerical RAOs of reacting bodies A and B constrained to heave motion with $F_{pto} = 0$ are plotted in Figure 4.5. As a strategy to avoid end-stop collisions during regular wave RAO tests, the wave amplitude was varied between tests. For RAO tests of reacting body A, $0.7\text{cm} \leq \eta \leq 3.9\text{cm}$ and for reacting body B, $1.5\text{cm} \leq \eta \leq 6\text{cm}$. A single curve, corresponding to $\eta = 3\text{cm}$ and $C_{Dz2} = 2.5$, is shown for the simulations of reacting body A. Two curves, corresponding to $\eta = 3\text{cm}$ and 6cm with $C_{Dz2} = 3.5$, are shown for the simulations of reacting body B.

The experimental RAO data from regular waves seen in Figure 4.5 come from tests of a variety of wave amplitudes. Motion constraints on the linear guide system limited the allowable wave amplitudes near the reacting body resonant frequencies. Away from the reacting body resonant frequencies, greater wave amplitudes were tested. At the very lowest wave frequencies $\omega \approx 0.5\text{rad/s}$, longitudinal tank reflections limited the ability to achieve steady state oscillations. The simulated heave RAO's show general agreement with all of the experimental data—building confidence in the simulation's capability to model the reacting body heave dynamics with reacting body A and B heave drag coefficients of $C_{Dz2} = 2.5$ and $C_{Dz2} = 3.5$.

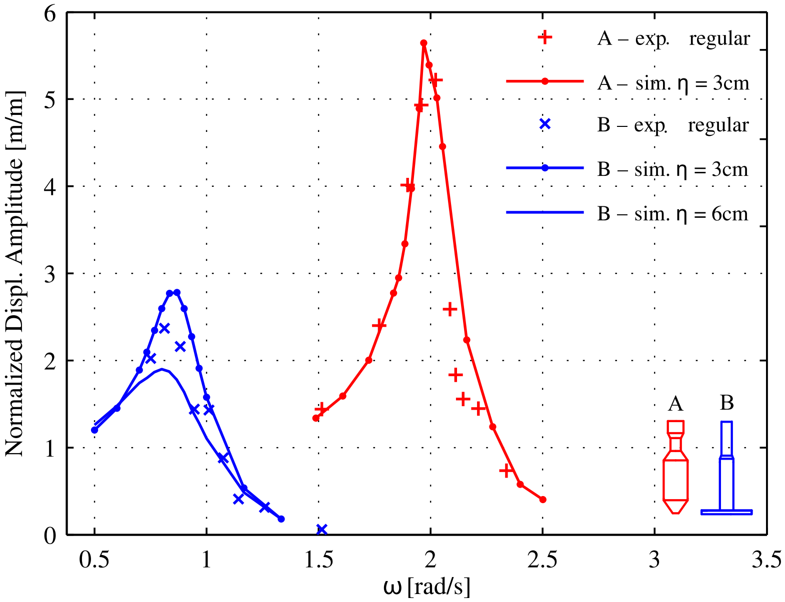

Figure 4.5: Heave displacement amplitude, normalized by wave amplitude, as a function of wave frequency for WEC A and WEC B reacting bodies.

4.6 Power Conversion Results

This section discusses results from tests of moored WECs A and B converting wave power to mechanical power in 20 regular wave conditions, representing typical operating conditions, from 1-4rad/s and 4-6cm heights as well as results from simulations that correspond to each of the experimental tests. Each WEC is given an individually adjusted PTO damping force. Comparisons between the experimental and simulated results are done for pitching motions, mooring loads, PTO force and displacements, as well as both absolute and normalized mechanical power.

4.6.1 Pitch and Roll Oscillations

During power capture tests, the pitch and roll oscillations of each WEC were observed to be highly transient in nature. Consequently, standard deviations,σ_p and σ_r, were respectively chosen as metrics for quantifying the magnitudes of pitch and roll for each test. In addition, the combined pitch and roll standard deviation is defined by Eq. (4.1)

$$\sigma_{pr} = \sqrt{\sigma_p^2 + \sigma_r^2} \tag{4.1}$$

The combined standard deviation of pitch and roll for WEC A and WEC B are shown in Figures 4.6 and 4.7. Results are given for both experimental and simulated data. Markers on the horizontal axis indicate the pitch natural frequencies as well as twice the pitch natural frequencies for WECs A and B.

Two main observations can be made from Figures 4.6 and 4.7. First, Figure 4.6 shows the simulated results are in agreement with the trends in the experimental results. Large pitching motions are seen both in experiments and simulations around the identified pitch natural frequencies. Second, the upper plot of Figure 4.7 shows the simulations over predict pitching motions for WEC A at $\omega = 3.75$-4rad/s and WEC B at $\omega = 3.8$rad/s. However, the lower plot of Figure 4.7 shows the simulations under predict roll motions.

An investigation of the time series, not shown here, indicates the pitch/roll oscillations observed for WEC A and B, for wave frequencies $\omega < 2.5$rad/s, have a frequencies equal to the wave frequency. These pitch/roll oscillations occur because $\omega \sim \omega_p$. However, the large pitch oscillations observed for WEC A, for wave frequencies $\omega > 3.5$rad/s, have a frequency $\omega/2$. Similarly, the large pitch oscillations observed for WEC B, in the wave frequency range 2.5rad/s $< \omega <$ 3.0rad/s, have a

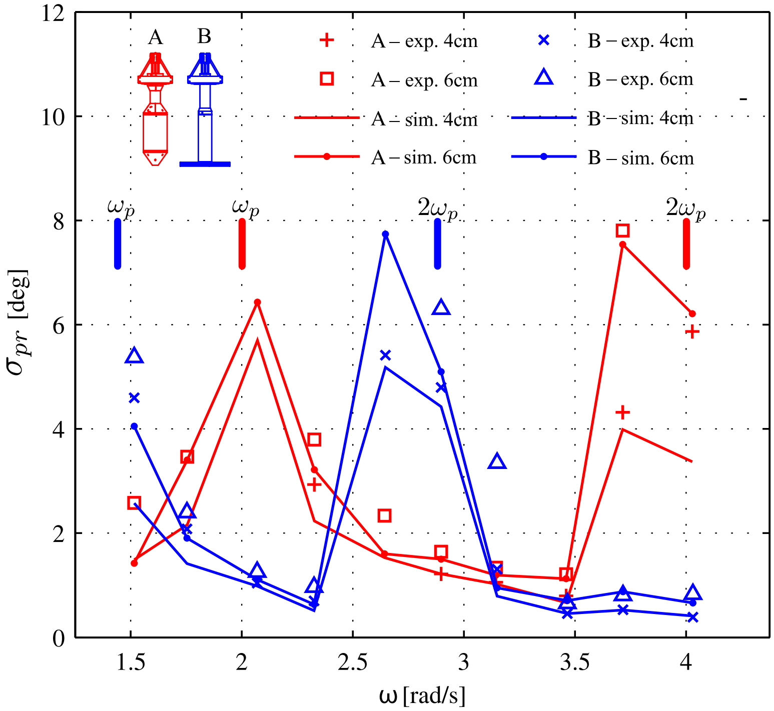

Figure 4.6: Combined standard deviation of pitch and roll, σ_{pr}, as a function of wave frequency for WEC A and WEC B during power conversion tests. Solid line markers indicate the single (ω_p) and double ($2\omega_p$)pitch natural frequencies for each WEC. Missing experimental data points are due to motion tracking system limitations.

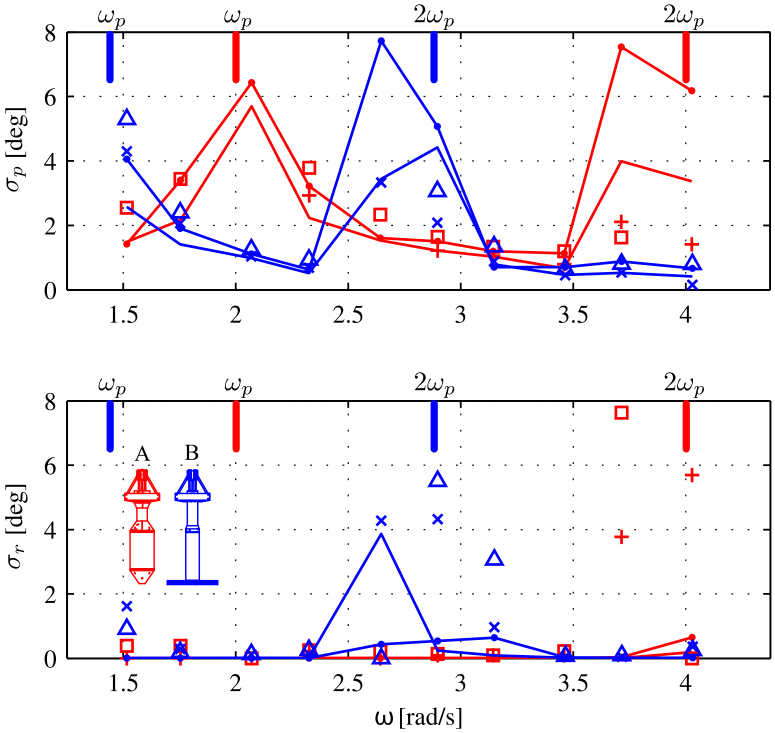

Figure 4.7: Standard deviation of pitch and standard deviation of roll as a function of wave frequency for WEC A and WEC B during power conversion tests. Solid line markers indicate the single (ω_p) and double ($2\omega_p$) pitch natural frequencies for each WEC.

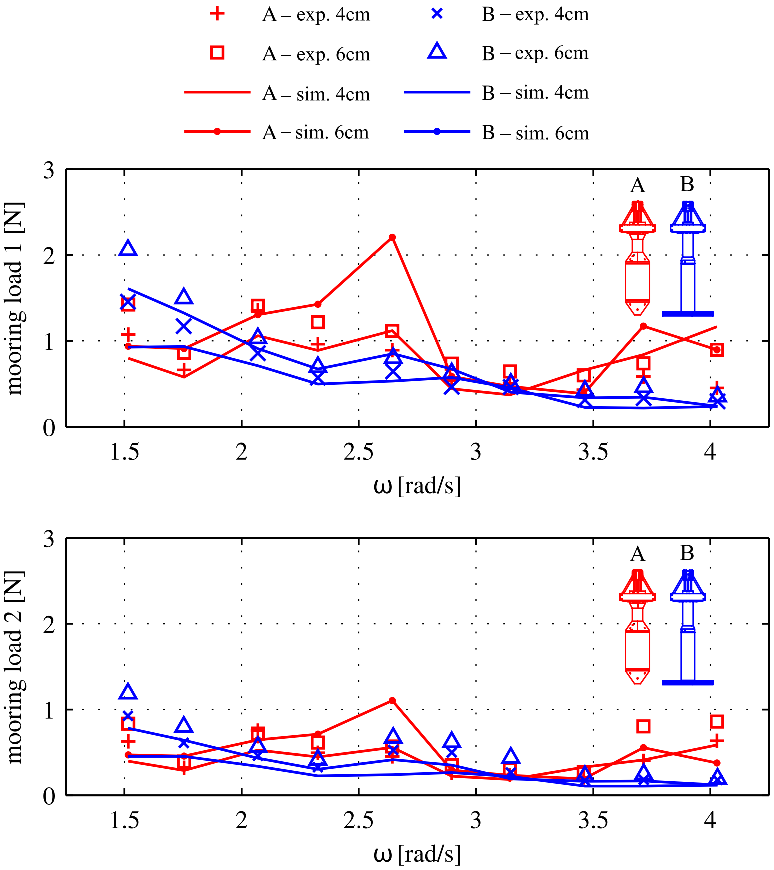

Figure 4.8: Standard deviation of tension in mooring lines 1 and 2 as a function of wave frequency for WEC A and WEC B during power conversion tests. Refer to Figure 4.2 to identify mooring lines.

frequency $\omega/2$. These pitch oscillations occur because $\omega \sim 2\omega_p$. In other words, the excitation from every second wave is combined to excite the pitch resonance.

4.6.2 Mooring forces and PTO dynamics

The standard deviations of experimental and simulated mooring forces are shown in Figure 4.8. The mooring force fluctuations from simulation agree reasonably well with experimental mooring tension data. In general, less agreement between simulated and experimental mooring forces is observed near pitch resonance frequencies.

The standard deviation of PTO force and relative float-reacting body displacement are shown in Figure 4.9. There is strong agreement between simulated and experimental PTO force apart from a couple of outliers which propagate into the power conversion results to be observed later. General agreement is also observed in

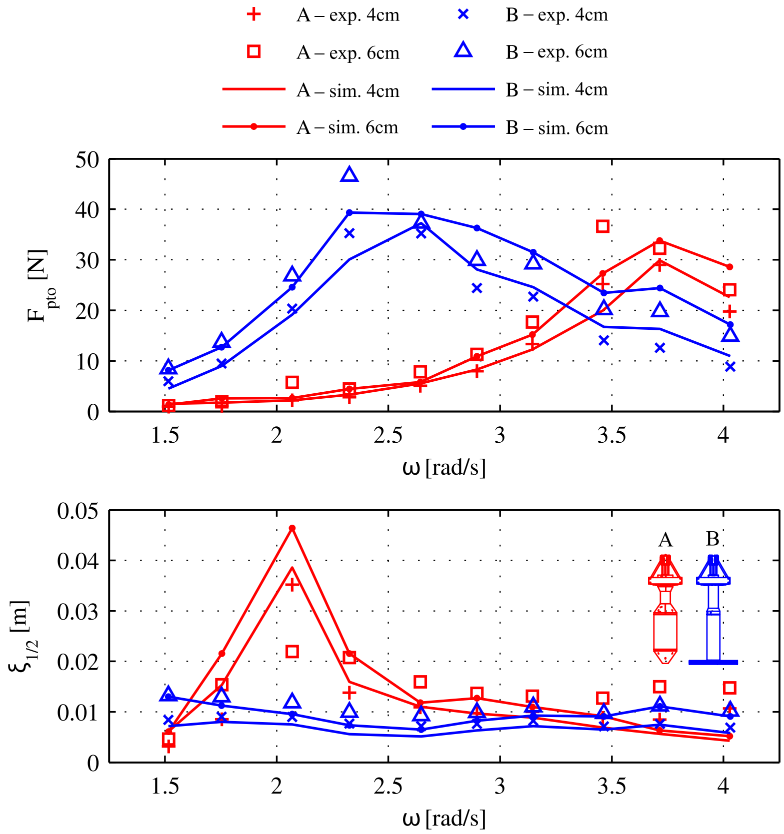

Figure 4.9: Standard deviation of PTO force and relative float-reacting body displacement as a function of wave frequency for WEC A and WEC B during power conversion tests.

the simulated and experimental relative float-reacting body displacements apart from a few outliers. The peak at $\omega = 2.07\text{rad/s}$ in the WEC A relative float-reacting body displacement is notable in its magnitude as well since it contributes very little to the overall power conversion performance of WEC A.

4.6.3 Power Conversion

The experimental and simulated average mechanical power, for both WECs in $2\eta \sim$ 4cm waves, are plotted in Figure 4.10. The simulated results show agreement with the general trends seen in the experimental mechanical power. The simulated power for WEC A agrees with the experimental output quite well apart from $\omega = 3.48\text{rad/s}$. The simulated power for WEC B shows less agreement with the experimental power. The two simulated power curves for each WEC correspond to the use of a) a single frequency component and b) multiple wave components to represent the wave

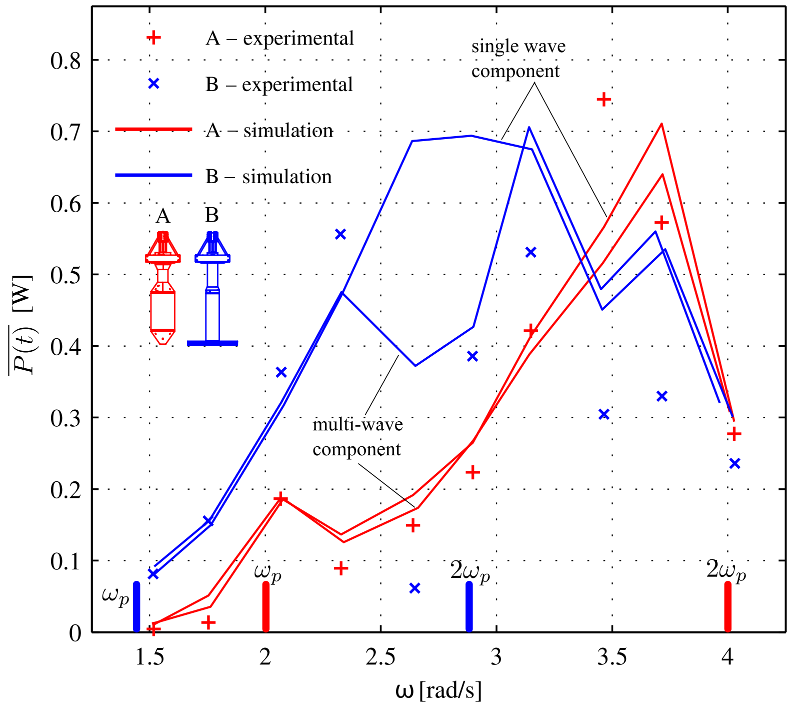

Figure 4.10: Average power output of WEC A and WEC B in regular waves of 4cm nominal height as a function of wave frequency. Solid line markers indicate the single (ω_p) and double ($2\omega_p$) pitch natural frequencies for each WEC.

conditions in simulation.

Figure 4.11 shows the experimental and simulated average mechanical power normalized by wave amplitude squared. Data is shown for both $2\eta \sim 4$cm and $2\eta \sim 6$cm. Two main observations of Figure 4.11 can be made. First, for both WECs, the experimental and simulated normalized power generally collapses together for all frequencies except in the frequency ranges where $\omega \sim 2\omega_p$. The only exception to this is for WEC A's simulated power curve at $\omega = 2.64$rad/s. Second, in the frequency ranges where $\omega \sim 2\omega_p$ for both WECs, the simulated and experimental normalized power for 6cm wave height falls far below the simulated normalized power for 4cm wave heights. The tendency for the normalized power at larger wave heights to diverge around the $\omega \sim 2\omega_p$ pitch resonance frequency, serves as evidence that pitch and/or roll resonant oscillations at the frequencies $\omega \sim 2\omega_p$ have a parasitic effect on power conversion.

Two main sources of error in the power conversion results are identified: (1) The transient nature of the moored WEC dynamics, especially in the pitch/roll degrees of freedom, causes error due to the choice of time window over which to sample

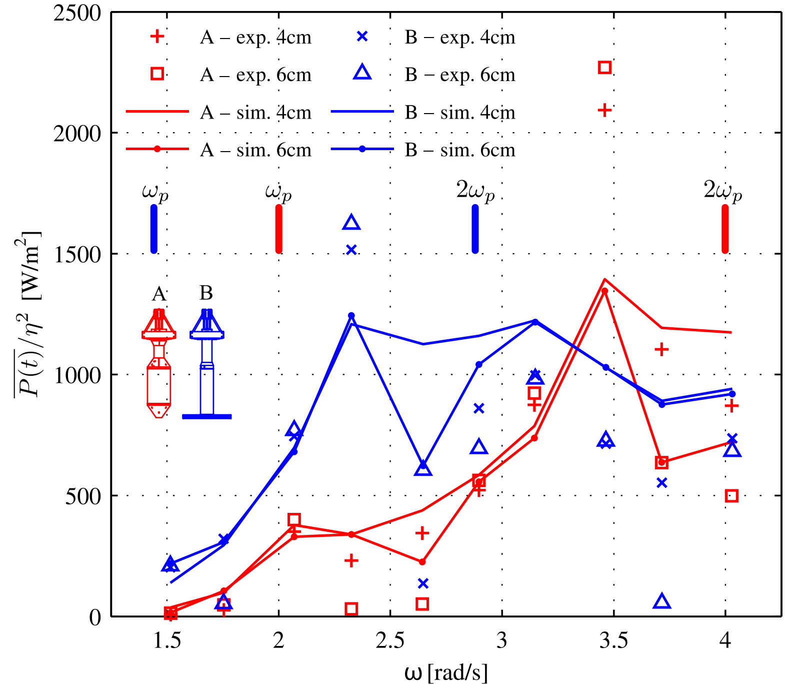

Figure 4.11: Normalized average power output of WEC A and WEC B in regular waves of 4cm, 6cm nominal height as a function of wave frequency. Solid line markers indicate the single (ω_p) and double ($2\omega_p$) pitch natural frequencies for each WEC.

average power and standard deviations of dynamic signals; (2) An assessment of standing wave resonant frequencies and wave probe measurements of surface elevations with transverse wave fluctuations, given in Appendix F, indicates that the large disagreements between experimental and simulated WEC power conversion in the range ω = 2.25-2.75rad/s and ω = 2.25-2.75rad/s is likely attributable to tank wall/standing wave effects.

4.7 Assessment of Strakes for Pitch Mitigation

Evidence given above indicates is likely that power production is limited by the excessive pitch and roll motions at the resonances for $\omega \sim 2\omega_p$. It is likely possible to reduce the excessive pitch/roll motions using a physical change to each WEC's design. A concept proposed here, to attach *strakes* that act vertical stabilizers for the heave degree of freedom while acting as damper plates for the pitch/roll degrees of freedom, will be assessed.

Using the numerical simulation, comparisons of the power conversion and motion dynamics of each WEC with and without strakes are made in regular waves. Three wave frequencies where pitch/roll resonances observed in Figures 4.6 and 4.7 are chosen for the simulations with strakes and the corresponding c_{pto} levels from Table 4.1 are taken.

4.7.1 Strake Design

Four strakes, modelled by 30cm x 30cm x 1cm thick plates, were attached to the lower outside reacting body of each WEC as shown in Figure 4.12. The strakes are aligned with the xz and yz planes. The strake physical dimensions and the strake position relative to each WEC's centre of rotation are held constant across WEC A and WEC B.

The drag coefficients of the strakes are estimated as $C_{Dx} = C_{Dy} = 3.0$, a value consistent with parameter identification results from the WEC B heave damper plate, which is also thin and sharp edged. To single out the effect of strake drag on the WEC dynamics, the added mass of the strakes is set to zero.

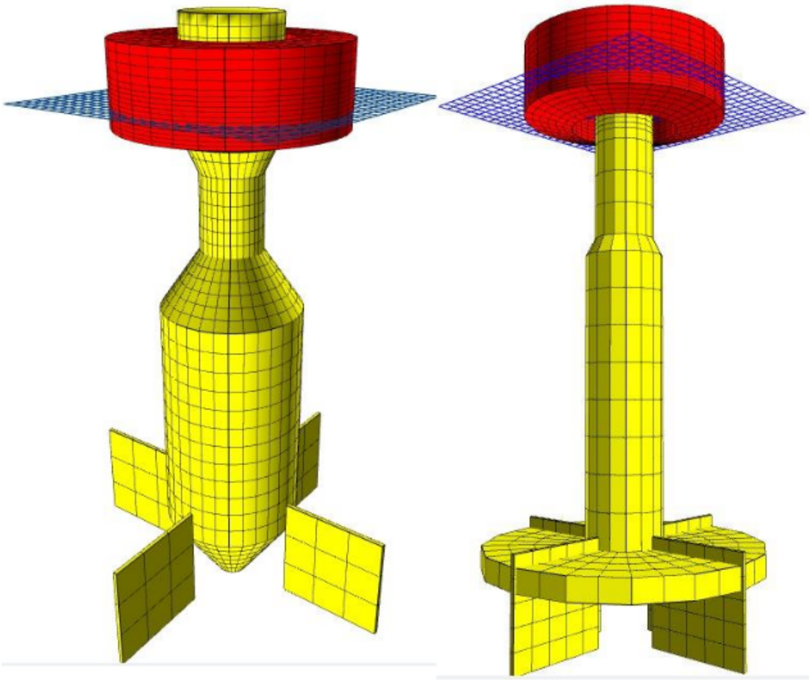

Figure 4.12: Simulation panel meshes of the two WECs fitted with strakes to minimize pitch/roll. WEC A (left), WEC B (right). Vertical distance between each WEC's centre of rotation and the strakes are held constant at a value 0.69m.

4.7.2 Simulation Results

Each simulation specified monochromatic Airy waves, run times of 240 seconds, and a ramp up time of 20 seconds. Results from last 40 seconds of simulations of WEC A and WEC B with and without strakes are given in Figures 4.13 and 4.14. Time series of pitch, roll, relative float-reacting body velocity $U_r(t)$, PTO force F_{pto}, and mechanical power conversion $P(t)$ are shown.

Figure 4.13 shows results from simulations of WEC A with and without strakes in waves of frequency $\omega = 4.02$rad/s and height $2\eta = 0.06$m. The simulation results with strakes attached to WEC A are observed to reduce pitch and roll amplitudes compared to the results without strakes. In addition, the simulations with strakes show higher amplitudes of relative velocity and PTO force. Finally, the simulation results with strakes show a much greater mechanical power conversion over the simulation results without strakes. For WEC A, in monochromatic waves at $\omega = 4.02$rad/s, the strakes succeeded in their envisioned purpose.

Observations of results from simulations of WEC B with and without strakes, $\omega = 2.89$rad/s, $2\eta = 0.06$m, seen in Figure 4.14 shows results similar results from WEC A. Simulation results with strakes attached to WEC B are shown to significantly reduce pitching motions compared to results without strakes. However, simulation results with strakes are shown to increase roll motions over simulation results without strakes. Despite the increase in roll motion, the simulation results with strakes indicate an increased relative velocity and PTO force, leading to a significant increase in the mechanical power conversion in comparison to simulation results without strakes. For WEC B, in monochromatic waves at $\omega = 2.89$rad/s, the strakes also succeeded in their envisioned purpose.

The result, that pitch amplitudes are reduced by the strakes for WEC B while roll amplitudes are increased, illustrates an interesting behaviour of axi-symmetric SRPAs also observed in the experiments: because the pitch and roll natural frequencies are equivalent, a small bias or perturbation to the WEC system can lead to transitions in the motion dynamics from pitch dominated oscillations to roll dominated oscillations or a combination thereof.

The strakes to no-strakes simulation results comparisons are summarized for WEC A and WEC B in Tables 4.3 and 4.4 respectively. The bold faced rows highlight the summaries of the results shown in Figures 4.13 and 4.14.

Table 4.3 quantifies strakes' affect on the WEC A average power conversion: for

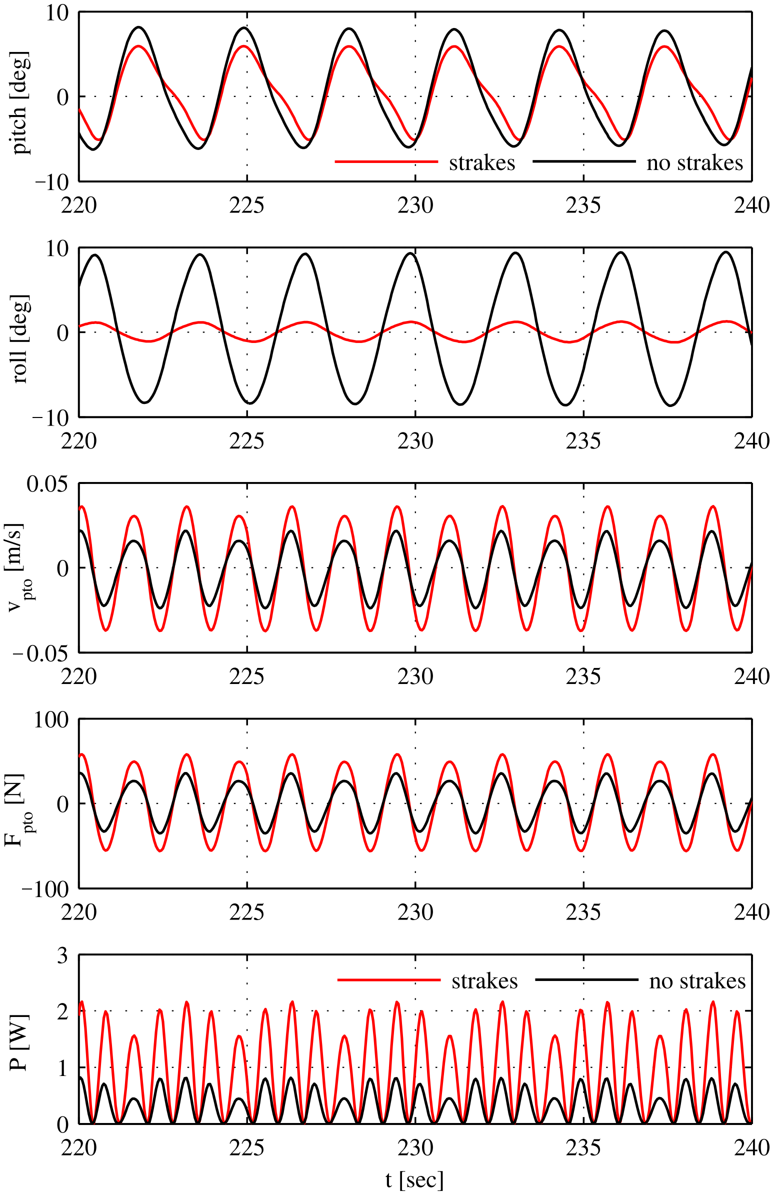

Figure 4.13: Simulation results for moored WEC A with and without strakes in monochromatic waves ω =4.02rad/s, $2\eta = 0.06$m.

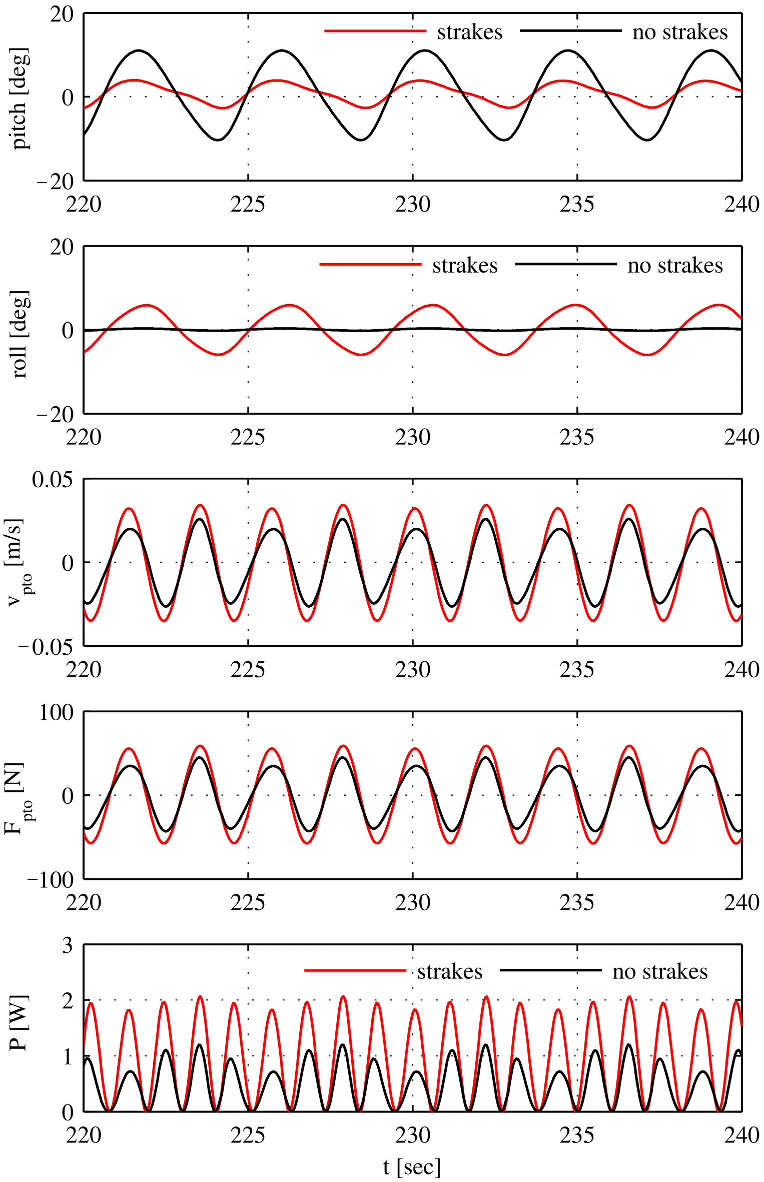

Figure 4.14: Simulation results for WEC B with and without strakes in monochromatic waves ω =2.89rad/s, $2\eta = 0.06$m.

$\omega = 4.02$rad/s, $\bar{P}$ is increased by 136-187%; for $\omega = 3.71$rad/s, $\bar{P}$ is increased by 19-77%; and for $\omega = 2.07$rad/s, $\bar{P}$ is decreased by 7-9%. Table 4.4 quantifies strakes' affect on the WEC B average power conversion: for $\omega = 2.89$rad/s, $\bar{P}$ is increased by 82-100%; for $\omega = 2.64$rad/s, $\bar{P}$ is increased by 46-65%; and for $\omega = 1.51$rad/s, $\bar{P}$ is decreased by 4-6%;

For both WECs, the strakes afford drastic improvements to power conversion near the pitch resonant frequencies where $\omega \sim 2\omega_p$. The strakes cause slight reductions, however, in power conversion near the $\omega \sim \omega_p$ resonances. But, because the $\omega \sim 2\omega_p$ resonances fall nearer to the peak output of each WEC's power producing frequency band than the $\omega \sim \omega_p$ resonances, parasitic pitch/roll motions from $\omega \sim 2\omega_p$ resonances will have greater effect on each WEC's annual energy production than the $\omega \sim \omega_p$ resonances. Consequently, the reductions of parasitic pitch/roll motion and the associated power conversion improvements made by the strakes appears significant. An expanded analysis of the WECs fitted with strakes should include the added mass contributions of the strakes, as well an assessment of the power conversion in panchromatic waves.

Table 4.3: Summary of results for WEC A with and without strakes.

		With Strakes			Without Strakes		
ω	2η	$\bar{P}$	σ_p	σ_r	$\bar{P}$	σ_p	σ_r
[rad/s]	[m]	[W]	[deg]	[deg]	[W]	[deg]	[deg]
4.02	0.04	0.56	2.12	0.001	0.24	5.83	0.001
3.71	0.04	0.73	0.68	0.001	0.61	4.61	0.000
2.07	0.04	0.15	3.37	0.001	0.16	5.37	0.002
4.02	**0.06**	**0.98**	**3.61**	**0.777**	**0.34**	**5.05**	**6.099**
3.71	0.06	1.18	3.72	0.001	0.67	5.19	5.503
2.07	0.06	0.27	4.11	0.001	0.29	6.55	0.004

Table 4.4: Summary of results for WEC B with and without strakes.

		With Strakes			Without Strakes		
ω	2η	$\bar{P}$	σ_p	σ_r	$\bar{P}$	σ_p	σ_r
[rad/s]	[m]	[W]	[deg]	[deg]	[W]	[deg]	[deg]
2.89	0.04	0.52	3.33	0.272	0.29	5.70	0.066
2.64	0.04	0.53	3.87	0.021	0.36	5.97	0.010
1.51	0.04	0.07	2.67	0.002	0.08	3.49	0.001
2.89	**0.06**	**0.98**	**2.22**	**4.119**	**0.49**	**7.45**	**0.189**
2.64	0.06	0.73	5.98	0.013	0.44	8.20	0.003
1.51	0.06	0.16	3.22	0.002	0.17	4.27	0.005

4.8 Conclusions

The following conclusions can be drawn:

1. Congruent with conclusions of chapter 2, the power performance of WEC B is wider banded in the frequency range studied and WEC A's power production peak ($\omega = 3.75$) occurs at a higher frequency than WEC B's ($\omega =$ 2.5-3.25rad/s).
2. The damper plate design approach is effective for the design of SRPA reacting bodies. It is shown to provide a high added mass which improves power performance by driving the reacting body natural frequency low without the need for structural mass. Because the damper plate reduces the structural mass while increasing the power production, damper plates are improves the cost efficiency of power production from SRPA WECs.
3. For the SRPA WECs studied, the peak power conversion occurs at a frequency equal to the heave natural frequency of the effective single body when the float is locked to the reacting body.
4. For slack moored SRPAs, resonant oscillations in pitch and roll that occur when the wave frequency is equal to twice the pitch natural frequency severely degrade the power conversion performance.
5. Vertical stabilizing strake plates, fitted below the centres of gravity and rotation of the SRPA WEC, are effective at mitigating the parasitic pitch and roll oscillations that occur when the wave frequency is equal to twice the pitch natural frequency. For the WEC's studied, the average power production with strakes is improved by 20-190% compared the the WEC's without strakes in the same conditions.

Chapter 5

Conclusions

To characterize and quantify the key dynamic and hydrodynamic factors that contribute to the power conversion performance of SRPA WECs, two, archetypal, SRPAs were selected for experimental and numerical investigation. A 1:25 scale, reconfigurable self-reacting WEC fitted with an adjustable PTO system has been developed and a comprehensive series of tests has been conducted. The tests were aimed at quantification of hydrodynamic parameters as well as power conversion. To provide for equitable power conversion comparisons, each WEC was given a uniquely optimized power take off damping level. Using the experimental platform as a backbone, and applying three phases of numerical modelling, I have shown:

1. Budal's theoretical upper bound on power conversion for single body WECs can be extended to two body WECs. The bound is established from the maximum utilization of the wave excitation forces on a two body WEC.

2. Using an experimentally validated, heave constrained, frequency domain numerical dynamics model of WECs A and B in monochromatic waves,

    - that, given optimal passive damping PTOs, WEC A's peak power conversion occurs at much higher frequency than WEC B's peak, due to the very high added mass contribution of the damper plate on WEC B's reacting body.
    - that reactive control PTOs significantly increase power conversion for both WECs, though the increase is more practical to implement for WEC B than for WEC A because WEC B's relative displacement under reactive control is much lower than WEC A's.

3. A least squared error minimization scheme can be used to extract Morison drag and Coulomb friction coefficients from decay tests for under-damped floating bodies. The scheme uses a time domain model of the floating body inside the objective function.

4. Using power conversion and capture width matrices calculated by an experimentally validated, heave constrained, time domain numerical dynamics model of WECs A and B in panchromatic waves,

   - WEC A has a greater peak power conversion but WEC B has a wider banded power conversion.
   - Comparisons of hourly power production over a year indicate, at full scale, that WEC A produces 54.7kW on average and WEC B 78.5kW at a representative location off the West Coast, BC, Canada.

5. Using an experimentally validated time domain simulation of WECs A and B with three legged moorings in panchromatic waves,

   - Vertical stabilizing strake plates, fitted below the centres of gravity and rotation of the WECs, are effective at mitigating the power conversion degradation from parasitic pitch and roll oscillations that occur when the wave frequency is equal to twice the pitch natural frequency.
   - For the WECs studied, the average power production with strakes is improved by 20-190% compared the the WEC's without strakes in the same conditions.

6. The damper plate design approach is effective for the design of SRPA reacting bodies. It is shown to provide a high added mass which improves power performance by driving the reacting body natural frequency low without the need for structural mass. Because the damper plate reduces the need for structural mass while increasing the power production, heave damper plates will improve the cost efficiency of power conversion from SRPA WECs.

Appendix A

Representative sea condition distributions

Three relevant distributions were extracted from a 10 year series of records taken at 3hour intervals for a grid point located near Hesquiaht Sound, on the Pacific coast of Canada. These distributions are plotted in Figure 2.17b.

1. The first distribution is from a histogram analysis of data set where the fraction of occurrence (or probability density function) of energy period, PDF[T_e], was extracted.

2. The second distribution derives from a joint (H_s, T_e) probability of occurrence analysis. Of all records, the most frequently occurring pair from the data set is $(H_s, T_e) = (1.5m, 8.0sec)$. Next, all records where $1.35m \leq H_s \leq 1.65m$ and $7.2sec \leq T_e \leq 8.8sec$ were identified amounting to ∼1800 records. Finally, a mean "most-frequent" variance density spectrum, $S_{MF}(T)$, was formed by taking the mean of the set of 1800 identified variance density spectra.

3. The third distribution derives from a joint (H_s, T_e) probability of occurrence analysis that is weighted by the wave power transport. Of all records, the sea state most contributing to mean annual wave power is $(H_s, T_e) = (3.0m, 10sec)$. Next, all records where $2.7m \leq H_s \leq 3.3m$ and $9sec \leq T_e \leq 11sec$ were identified amounting to ∼1500 records. Finally, a mean "power weighted most frequent" variance density spectrum, $S_{PW}(T)$,was formed by taking the mean of the set of 1500 identified variance density spectra.

Appendix B

WEC Model specifications

Summary specifications of the WEC models and identified parameters are given in Table B.1. Radial profiles showing the submerged geometries of the WECs are shown in Figure B.1.

Table B.1: Detailed specifications of experimental WEC models

Parameter	WEC A Value	WEC B Value	Units
Float			
Outer diameter	0.595	0.595	[m]
Inner diameter	0.317	0.317	[m]
Hydrostatic stiffness	2000	2000	[N/m]
Physical mass	12	12	[kg]
Surface Area	0.3699	0.3699	[m^2]
Submerged Volume	0.01218	0.01218	[m^3]
Reacting Body			
Hydrostatic stiffness	509.5	222.9	[N/m]
Physical Mass	115	75.5	[kg]
Surface Area	1.409	1.996	[m^2]
Submerged Volume	0.1104	0.07546	[m^3]

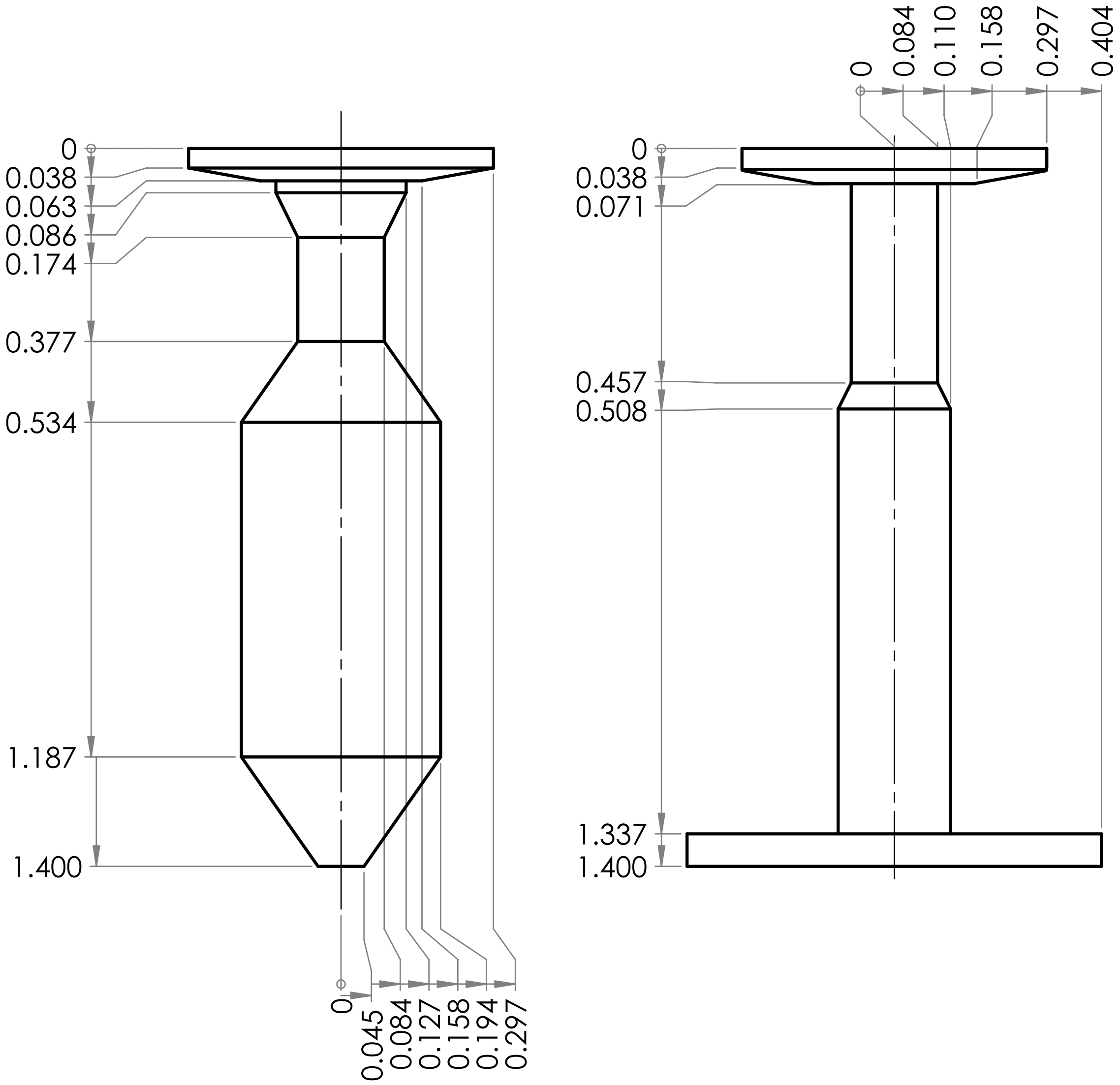

Figure B.1: External dimensions of experimental WEC models. Units in meters.

Appendix C

Irregular Wave Conditions & Analysis

Twenty six sea states were tested for each WEC representing tests between both the most frequent and power weighted most frequent operating conditions as discussed in Section 3.3.2. Nine spectra taken from the wave probe signals are shown in Figure C.1. The significant wave height is taken from the variance of the timeseries by $H_s = 4\sqrt{\sigma^2_{\eta(t)}}$. The peak period was taken from the frequency at which the maximum of the smoothed variance density spectrum occurs. The smoothed variance density spectrum is obtained by low pass filtering the variance density spectrum.

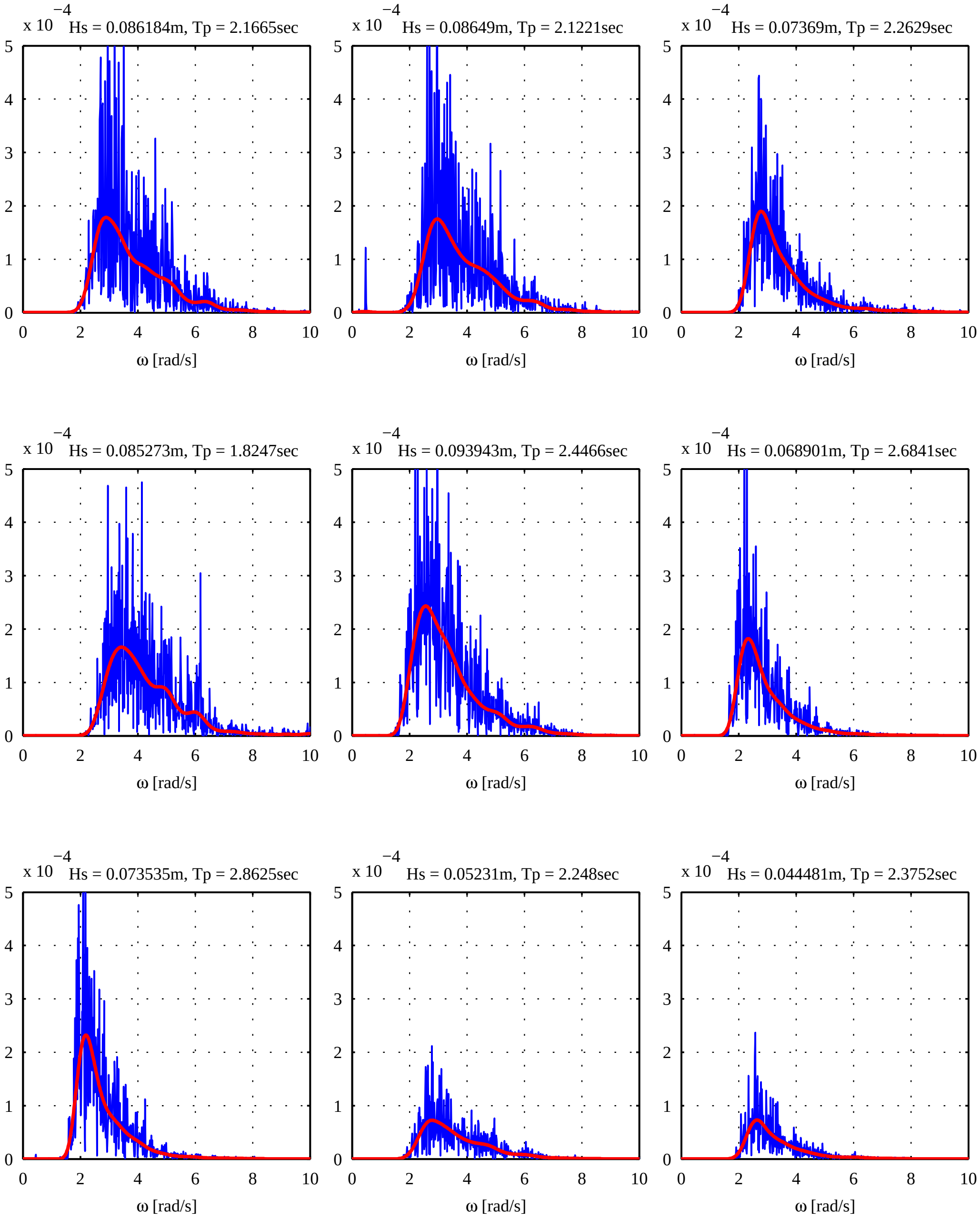

Figure C.1: Nine example variance density spectra taken from the wave probe surface elevation signals.

Appendix D

Inviscid Hydrodynamic Coefficients

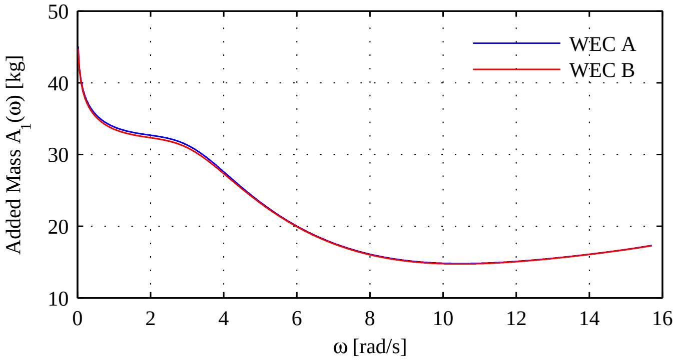

(a) Float added mass

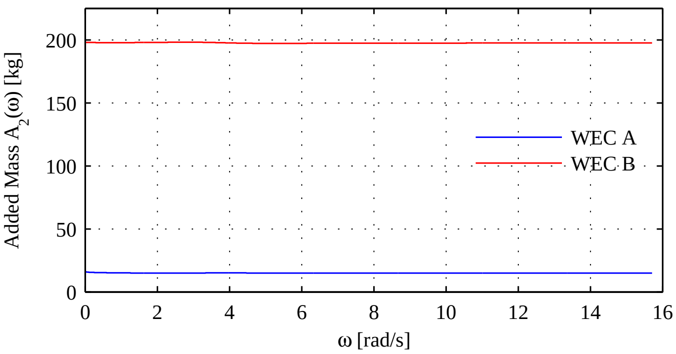

(b) Reacting body added mass

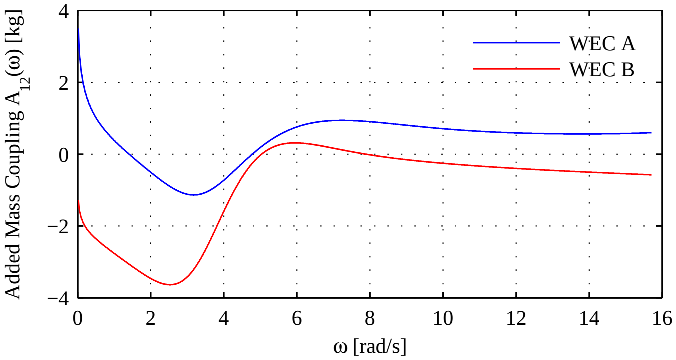

(c) Float-reacting body added mass coupling

Figure D.1: Added mass coefficients from BEM analysis for both WECs.

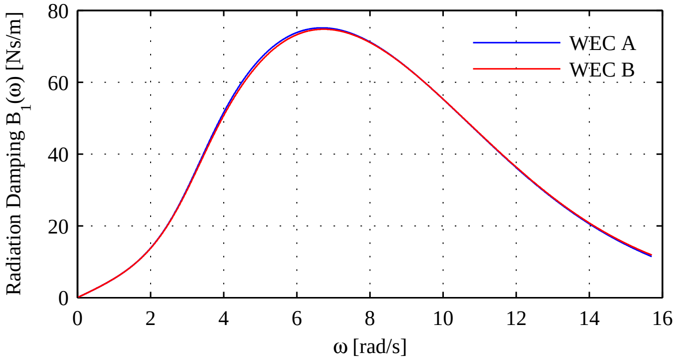

(a) Float radiation damping

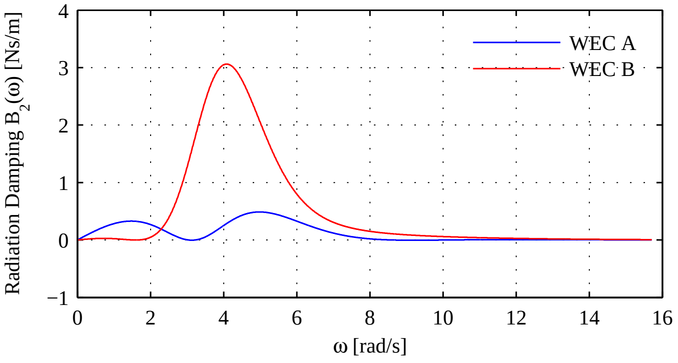

(b) Reacting body radiation damping

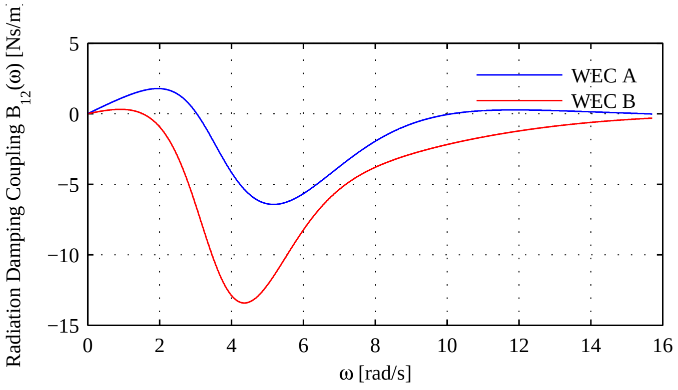

(c) Float-reacting body radiation damping coupling

Figure D.2: Radiation damping coefficients from BEM analysis for both WECs.

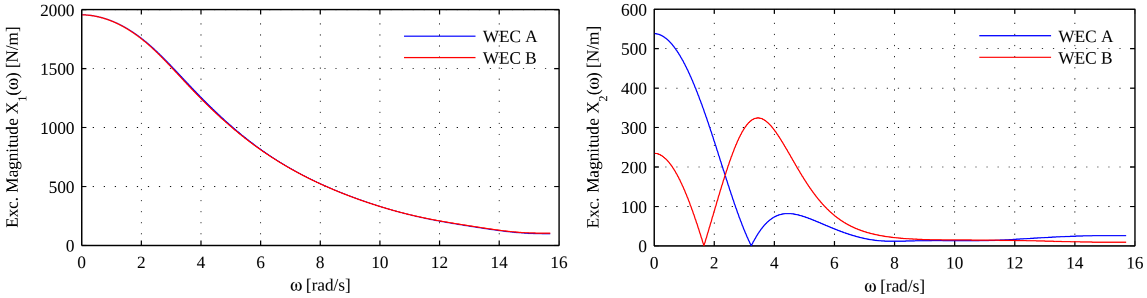

(a) Float excitation magnitude **(b)** Reacting body excitation magnitude

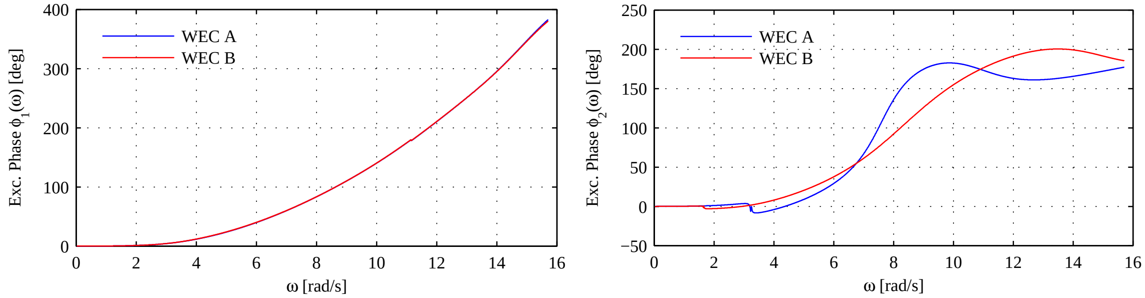

(c) Float excitation phase **(d)** Reacting body excitation phase

Figure D.3: Excitation force coefficients from BEM analysis.

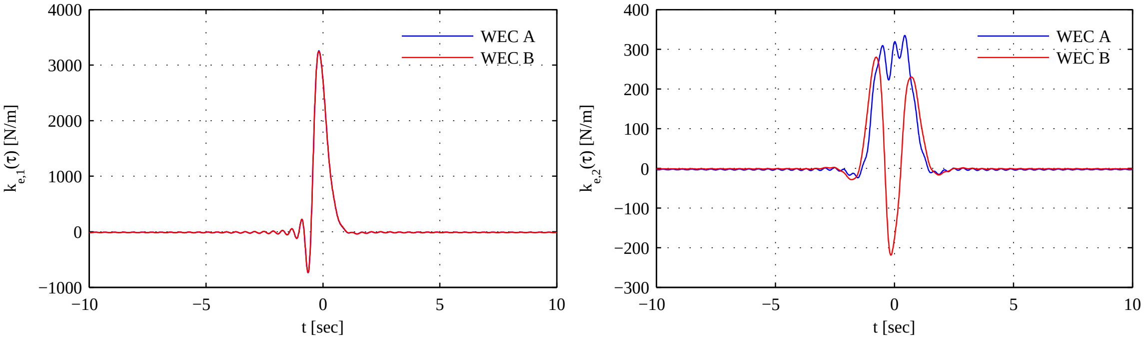

(a) Float excitation kernel **(b)** Reacting body excitation kernel

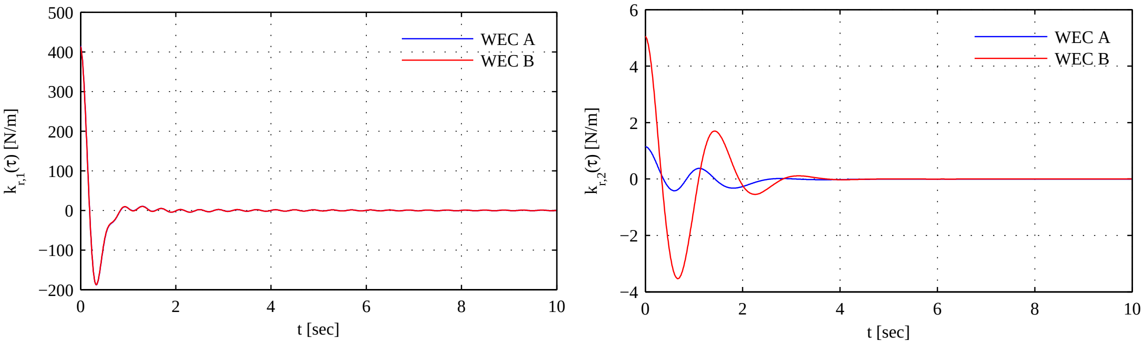

(c) Float radiation kernel **(d)** Reacting body radiation kernel

Figure D.4: Kernel functions for both WECs calculated from the inviscid hydrodynamic coefficients.

Appendix E

The Effect of Radiation Coupling

To illustrate the effect of radiation coupling impedance Z_c on the power production of WEC A and WEC B, the frequency domain model defined by Eqs. (2.2) and (2.5) was used for each of WEC A and WEC B for $Z_c = 0$ and for Z_c as calculated from BEM analysis. Figure E.1 shows the normalized power capture from Eq. (2.7) as a function of frequency. Figure E.1 shows that $Z_c \neq 0$ only slightly increases the

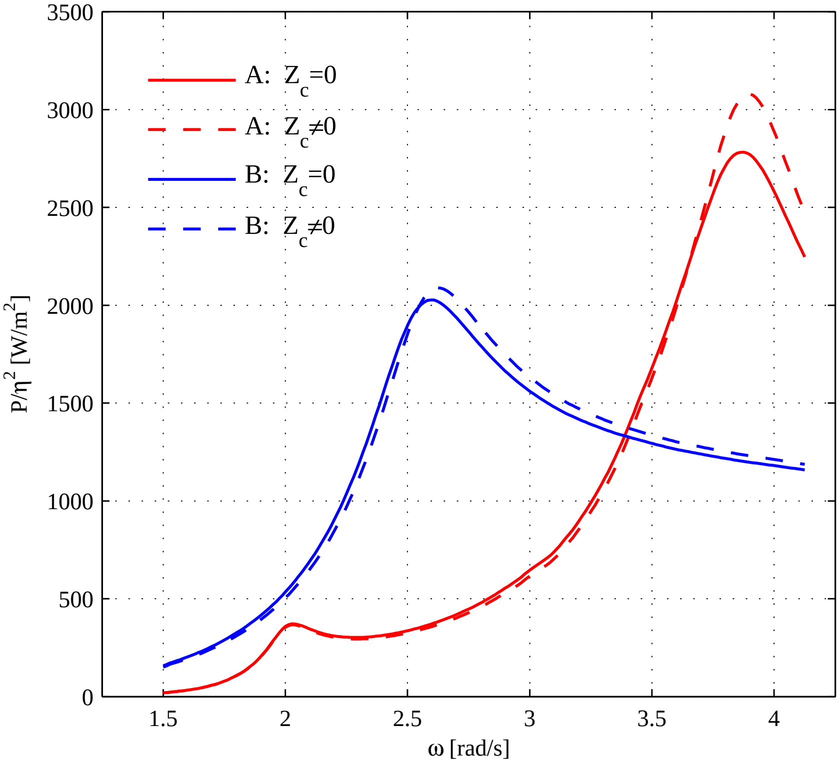

Figure E.1: The effect of radiation coupling impedance Z_c on WEC power conversion.

frequency domain power peaks. The increase is more pronounced for WEC A than for WEC B; The observed shifts in the power curves are due to a) the small off-diagonal contributions of Z_c to the impedance matrix Eq. (2.2) and b) the small contributions of Z_c in the PTO impedance calculated by way of the optimum amplitude condition Eq. (2.5).

Appendix F

Tank Wall Effects

An estimation of standing wave natural frequencies within the tank width $W = 4.57$m, using the linear dispersion relation given by Eq. (F.1), with resonant wavelengths $\lambda_0 = 2W$ and $\lambda_1 = W$, yields zeroth and first mode natural frequencies of $\omega_0 = 2.43$rad/s, and $\omega_1 = 3.66$rad/s.

$$\omega_i = \sqrt{\frac{2\pi g}{\lambda_i}\tanh\frac{2\pi h}{\lambda_i}} \tag{F.1}$$

Analyses of wave maker driven standing waves may utilize the work of Garret [23]. However, an analysis of wave data without installed WECs to find the wave frequencies most affected by standing waves was done. Measurements were recorded from two wave probes, one located at the origin, (x, y) = (0,0), and one located offset from the tank centreline, (x, y) = (0,-1m), for each of the monochromatic wave frequencies in Table 4.1 and for multiple wave heights. A linear regression of the two wave probe signals was executed for each of the regular wave conditions. Using Matlab's "robustfit.m" function, the best fit linear relationship between the offset wave probe signal and the origin wave probe signal was established in the form $\eta_{y=-1} = b_2\eta_{y=0} + b_1$. The slope, b_2, of the regression analysis for each regular wave condition is shown in Figure F.1. The regression results, given by Figure F.1, indicate repeatable differences between the centreline and offset wave probe signals at 2.6rad/s, 2.9rad/s, 3.2rad/s, 3.72rad/s, and 4rad/s. These repeatable differences are likely a result of excitation of transverse standing waves between the walls of the tank.

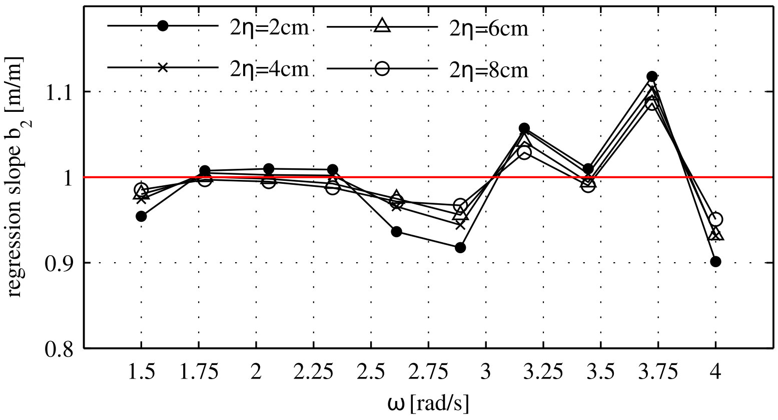

Figure F.1: Regular wave characterization: slope of the linear regressions between signals from the offset wave probe located at $(x, y) = (0, -1m)$ and the centreline wave probe at $(x, y) = (0, 0)$.

Bibliography

[1] Juan Pablo Julca Avila and Julio Cezar Adamowski. Experimental evaluation of the hydrodynamic coefficients of a ROV through Morison's equation. *Ocean Engineering*, 38(17–18):2162–2170, December 2011.

[2] A. Babarit, J. Hals, M.J. Muliawan, A. Kurniawan, T. Moan, and J. Krokstad. Numerical benchmarking study of a selection of wave energy converters. *Renewable Energy*, 41:44–63, May 2012.

[3] Aurelien Babarit, Jørgen Hals, Adi Kurniawan, Made Muliawan, Torgeir Moan, and Jorgen Krokstad. Numerical estimation of energy delivery from a selection of wave energy converters—final report. Technical report, Ecole Centrale de Nantes, NTNU Trondheim, Statkraft, 2011.

[4] H. Bailey and I.G. Bryden. The influence of a mono-directional PTO on a self-contained inertial WEC. *Proceedings of the 8th European Wave and Tidal Energy Conference EWTEC*, 2009.

[5] S. J. Beatty, C. Hiles, R. S. Nicoll, J. E. Adamson, and B. J. Buckham. Design synthesis of a wave energy converter. *Proceedings of the International Conference on Offshore Mechanics and Arctic Engineering*, Honolulu, Hawaii, 2009.

[6] Jose J. Candido and Paulo A.P.S. Justino. Modelling, control and Pontryagin maximum principle for a two-body wave energy device. *Renewable Energy*, 36(5):1545–1557, May 2011.

[7] Subrata K. Chakrabarti. *Developments in Offshore Engineering, wave phenomena and offshore topics*, chapter Modeling Laws in Ocean Engineering, pages 295–335. Gulf Professional Publishing, 1999.

[8] Ronan Costello, Josh Davidson, Davide Padeletti, and John V. Ringwood. Comparison of numerical simulations with experimental measurements for the response of a modified submerged horizontal cylinder moored in waves. In *ASME 2014 33rd International Conference on Ocean, Offshore and Arctic Engineering*, volume Volume 9B: Ocean Renewable Energy, page 8, San Francisco, California, USA, June 2014. OMAE2014-24270.

[9] Joao Cruz. *Ocean Wave Energy*. Number 1865-3529 in Green Energy and Technology(Virtual Series). Springer Berlin Heidelberg, 2008.

[10] W.E. Cummins. The impulse response function and ship motions. *Schiffstechnik*, 47:101–109, 1962. Reprinted as David Taylor Model Basin Report 1661.

[11] A.D. de Andres, R. Guanche, J.A. Armesto, F. del Jesus, C. Vidal, and I.J. Losada. Time domain model for a two-body heave converter: Model and applications. *Ocean Engineering*, 72(0):116–123, November 2013.

[12] DNV. Recommended practice DNV-RP-C205 Environmental conditions and environmental loads, 2010.

[13] David Elwood, Solomon C. Yim, Joe Prudell, Chad Stillinger, Annette von Jouanne, Ted Brekken, Adam Brown, and Robert Paasch. Design, construction, and ocean testing of a taut-moored dual-body wave energy converter with a linear generator power take-off. *Renewable Energy*, 35(2):348–354, February 2010.

[14] D.V. Evans. A theory for wave-power absorption by oscillating bodies. *Journal of Fluid Mechanics*, 77:1–25, 1976.

[15] D.V. Evans. Maximum wave-power absorption under motion constraints. *Applied Ocean Research*, 3(4):200–203, October 1981.

[16] J. Falnes. Wave-energy conversion through relative motion between two single-mode oscillating bodies. *Journal of Offshore Mechanics and Arctic Engineering*, 121(1):32–38, 1999.

[17] Johannes Falnes. Radiation impedance matrix and optimum power absorption for interacting oscillators in surface waves. *Applied Ocean Research*, 2(2):75–80, April 1980.

[18] Johannes Falnes. *Ocean Waves and Oscillating Systems: Linear Interactions including Wave Energy Extraction.* Cambridge University Press, 2002.

[19] Johannes Falnes. A review of wave-energy extraction. *Marine Structures*, 20(4):185–201, October 2007.

[20] R. Featherstone. *Rigid body dynamics algorithms.* Springer, 2008.

[21] F. Flocard and T.D. Finnigan. Experimental investigation of power capture from pitching point absorbers. *Proceedings of the 8th European Wave and Tidal Energy Conference EWTEC, Uppsala, Sweden*, 2009.

[22] M.J. French. Heaving point absorbers reaction against an internal mass. In *Hydrodynamics of ocean wave-energy utilization: IUTAM symposium*, pages 247–255, Lisbon, Portugal, 1985. Hydrodynamics of Ocean Wave-Energy Utilization.

[23] C. J. R. Garrett. On cross-waves. *Journal of Fluid Mechanics*, 41(04):837–849, 1970.

[24] Jorgen Hals, Torkel Bjarte-Larsson, and Johannes Falnes. Optimum reactive control and control by latching of a wave-absorbing semisubmerged heaving sphere. In *Proceedings of the International Conference on Offshore Mechanics and Arctic Engineering - OMAE*, volume 4, pages 415–423, Department of Physics, Norwegian Univ. of Sci. and Technol., NTNU, Trondheim, Norway, 2002. American Society of Mechanical Engineers.

[25] Jorgen Hals, Reza Taghipour, and Torgeir Moan. Dynamics of a force-compensated two-body wave energy converter in heave with hydraulic power take-off subject to phase control. In *Proceedings of the 7th European Wave and Tidal Energy Conference*, Porto, Portugal, Sept. 2007.

[26] J.C.C. Henriques, M.F.P. Lopes, R.P.F. Gomes, L.M.C. Gato, and A.F.O. Falcao. On the annual wave energy absorption by two-body heaving WECs with latching control. *Renewable Energy*, 45(0):31–40, September 2012.

[27] Clayton E. Hiles, Bradley J. Buckham, Peter Wild, and Bryson Robertson. Wave energy resources near Hot Springs Cove, Canada. *Renewable Energy*, 71(0):598–608, November 2014.

[28] E.R. Jefferys. Simulation of wave power devices. *Applied Ocean Research*, 6(1):31–39, 1984.

[29] L. Johanning, P.W. Bearman, and J.M.R. Graham. Hydrodynamic damping of a large scale surface piercing circular cylinder in planar oscillatory motion. *Journal of Fluids and Structures*, 15(7):891–908, October 2001.

[30] J.M.J. Journe and W.W. Massie. *Offshore Hydromechanics*. Delft University of Technology, 2001.

[31] U. A. Korde. On providing a reaction for efficient wave energy absorption by floating devices. *Applied Ocean Research*, 21(5):235–248, 1999.

[32] Umesh A. Korde. Systems of reactively loaded coupled oscillating bodies in wave energy conversion. *Applied Ocean Research*, 25(2):79–91, 2003.

[33] J.C. Lagarias, J. A. Reeds, M. H. Wright, and P. E. Wright. Convergence properties of the Nelder-Mead simplex method in low dimensions. *SIAM Journal of Optimization*, 9:112–147, 1998.

[34] Ye Li, Y.H. Yu, Epler J., and Previsic M. Experimental investigation of the power generation performance of floating-point absorber wave energy systems. In *27th International workshop on water waves and floating bodies*, Copenhagen, Denmark, 2012.

[35] M. F. P. Lopes, J. C. C. Henriques, Miguel C. Lopes, L. M. C. Gato, and Antnio Dente. Design of a non-linear power take-off simulator for model testing of rotating wave energy devices. In *Proceedings of The 8th European Wave and Tidal Energy Conference*, September 2009.

[36] Edward B.L. Mackay, Joao Cruz, Chris Retzler, Peter Arnold, Elva Bannon, and Remy Pascal. Validation of a new wave energy converter design tool with large scale single machine experiments. In *First Asian Wave and Tidal Energy Conference Series*, Jeju Island, Korea, November 2012. Asian Wave and Tidal Energy Conference AWTEC.

[37] A.P. McCabe, A. Bradshaw, J.A.C. Meadowcroft, and G. Aggidis. Developments in the design of the PS Frog mk 5 wave energy converter. *Renewable Energy*, 31(2):141–151, February 2006.

[38] Niels I. Meyer, Michael McDonald Arnskov, Carl Erik Vad Bennetzen, Hans F. Burcharth, J. Bnger, Vagner Jacobsen, Preben Maegaard, Stig Vindelv, Kim Nielsen, and Jens Nrkr Sorensen. Wave energy program completion report. Technical report, RAMBLL, Teknikerbyen 31, 2830 Virum, Denmark, 2002.

[39] Muliawan, Gao, Moan, and Babarit. Analysis of a two-body floating wave energy converter with particular focus on the effects of power take-off and mooring. *Journal of Offshore Mechanics and Arctic Engineering*, 135/3:12, 2013.

[40] Vincent S. Neary, Mirko Previsic, Richard A. Jepsen, Michael J. Lawson, Yi-Hsiang Yu, Andrea E. Copping, Arnold A. Fontaine, Kathleen C. Hallett, and Dianne K. Murray. Methodology for design and economic analysis of marine energy conversion (mec) technologies. Technical Report SAND2014-9040, Sandia National Laboratories, March 2014.

[41] P Nebel. Maximizing the efficiency of wave-energy plant using complex-conjugate control. *Proceedings of the Institution of Mechanical Engineers, Part I: Journal of Systems and Control Engineering*, 206(4):225–236, November 1992.

[42] Marcelo A.S. Neves and Claudio A. Rodriguez. On unstable ship motions resulting from strong non-linear coupling. *Ocean Engineering*, 33(14–15):1853–1883, October 2006.

[43] R. S. Nicoll, D. M. Steinke, J. Attia, A. Roy, and B. J. Buckham. Simulation of a high-energy finfish aquaculture site using a finite element net model. In *Proceedings of the ASME 2011 30th international conference on ocean, offshore and arctic engineering OMAE 2011*, 2011.

[44] R. S. Nicoll, C. F. Wood, and A. R. Roy. Comparison of physical model tests with a time domain simulation model of a wave energy converter. In *Proceedings of the ASME 2012 31th international conference on offshore mechanics and arctic engineering OMAE 2012*. OMAE, July 1-6 2012.

[45] S. Olaya, J.-M. Bourgeot, and M. Benbouzid. Hydrodynamic coefficients and wave loads for a WEC device in heaving mode. In *OCEANS - Bergen, 2013 MTS/IEEE*, pages 1–8, 2013.

[46] S. Olaya, J.-M. Bourgeot, and M. Benbouzid. Modelling and preliminary studies for a self-reacting point absorber WEC. In *First International Conference on Green Energy ICGE*, 2014.

[47] Gregory S. Payne, Jamie R.M. Taylor, and David Ingram. Best practice guidelines for tank testing of wave energy converters. *Journal of Ocean Technology*, 4(4):39–69, December 2009.

[48] A. Pecher, J.P. Kofoed, J. Espedal, and S. Hagberg. Results of an experimental study of the Langlee wave energy converter. In *Proceedings of the International Offshore and Polar Engineering Conference*, volume 1, pages 877–885, Beijing, China, 2010. International Society of Offshore and Polar Engineers.

[49] M. Previsic, Shoele Kourosh, and Jeff Epler. Validation of theoretical performance results using wave tank testing of a heaving point absorber wave energy conversion device working against a subsea reaction plate. Technical report, Re Vision Consulting, 2014.

[50] Mirko Previsic, Roger Bedard, and George Hagerman. E2I EPRI assessment offshore wave energy conversion devices. Technical Report E2I EPRI WP-004-US-Rev 1, Electricity Innovation Institute, June 2004.

[51] A.A.E. Price, C.J. Dent, and A.R. Wallace. Frequency domain techniques for numerical and experimental modelling of wave energy converters. In *Proceedings of the 8th European Wave and Tidal Energy Conference EWTEC*, 2009.

[52] P. Roux de Reilhac, F. Bonnefoy, J.M. Rousset, and P. Ferrant. Improved transient water wave technique for the experimental estimation of ship responses. *Journal of Fluids and Structures*, 27(3):456–466, April 2011.

[53] M. Ruellan, H. BenAhmed, B. Multon, C. Josset, A. Babarit, and A. Clement. Design methodology for a searev wave energy converter. *Energy Conversion, IEEE Transactions on*, 25(3):760–767, 2010.

[54] Thomas Sauder and Torgeir Moan. Experimental investigation of the hydrodynamic characteristics of a novel column design for semi-submersible platforms. In *Proceedings of the Sixteenth (2007) International Offshore and Polar Engineering Conference*, Lisbon, Portugal, July 2007.

[55] D. M. Steinke, R. S. Nicoll, and A. R. Roy. Real-time finite element analysis of a remotely operated pipeline repair system. In *Proceedings of the ASME 2013 32th International Conference on Offshore Mechanics and Arctic Engineering OMAE 2013*. OMAE, June 2013.

[56] D. M. Steinke, R. S. Nicoll, T. Thompson, and B. Paterson. Design methodology and numerical analysis of a cable ferry. *SNAME transactions*, 2013.

[57] Reza Taghipour, Tristan Perez, and Torgeir Moan. Hybrid frequency-time domain models for dynamic response analysis of marine structures. *Ocean Engineering*, 35(7):685–705, May 2008.

[58] Longbin Tao and Shunqing Cai. Heave motion suppression of a spar with a heave plate. *Ocean Engineering*, 31(5-6):669–692, 2004.

[59] Kevin Tarrant and Craig Meskell. Investigation on parametrically excited motions of point absorbers in regular waves. In *Proceedings of the ASME 2014 Pressure Vessels & Piping Conference PVP2014*, number PVP2014-28387 in , Anaheim, California, USA, July 2014.

[60] Taylor and Mackay. The design of an eddy current dynamometer for a free-floating sloped ips buoy. In *Proceedings of Marine Renewable Energy Conference*, pages 67–74, March 2001. ISBN 1-902536-43-6.

[61] Jørgen Hals Todalshaug. Practical limits to the power that can be captured from ocean waves by oscillating bodies. *International Journal of Marine Energy*, 2013.

[62] Carlos Villegas and Haite van der Schaaf. Implementation of a pitch stability control for a wave energy converter. *Ninth European Wave and Tidal Conference*, Southampton, UK, September 2011.

[63] WAMIT Inc., November 2012. Version 7.0.

[64] A. Weinstein, G. Fredrikson, L. Claeson, J. Forsberg, M.J. Parks, K. Nielsen, M.S. Jenses, K. Zandiyeh, P. Frigaard, M. Kramer, and T.L. Andersen. Aquabuoy-the offshore wave energy converter numerical modeling and optimization. In *OCEANS 2003. Proceedings*, volume 4, pages 1988–1995 Vol.4, 2003.

[65] Wello. The penguin wave energy converter, http://www.wello.eu/en/penguin, 2015.

[66] Bijun Wu, Xing Wang, Xianghong Diao, Wen Peng, and Yunqiu Zhang. Response and conversion efficiency of two degrees of freedom wave energy device. *Ocean Engineering*, 76:10–20, 2014.

[67] Yi-Hsiang Yu and Ye Li. Reynolds-averaged Navier Stokes simulation of the heave performance of a two-body floating-point absorber wave energy system. *Computers & Fluids*, 73(0):104–114, March 2013.

[68] Z. Yu and J. Falnes. State-space modelling of a vertical cylinder in heave. *Applied Ocean Research*, 17(5):265–275, 1995.

[69] A.S. Zurkinden, F. Ferri, S. Beatty, J.P. Kofoed, and M.M. Kramer. Non-linear numerical modeling and experimental testing of a point absorber wave energy converter. *Ocean Engineering*, 78(0):11–21, March 2014.